CBP 835

LBNL- ????
September 1, 2009

Accelerator Design Study for a Soft X-Ray Free Electron Laser at the Lawrence Berkeley National Laboratory

E. Kur, G. Penn, J. Qiang, M. Venturini, R. Wells, and A. Zholents

Lawrence Berkeley National Laboratory, Berkeley CA 94720

Abstract

A concept for a high brightness, high repetition rate, free electron laser light source operating in the soft x-ray spectrum is under development at LBNL. The present Report summarizes recent design studies for the accelerator part of the machine. We highlight aspects of charged particle dynamics that have the potential to affect the beam quality, discuss the main components of the beam delivery system, and present the baseline design for the accelerator utilizing superconducting technology. Particular attention is devoted to the study of the microbunching instability, which is modeled using state of the art multi-billion macroparticle simulations, assessment of multibunch instabilities, and investigation of jitter errors including an approximate model of a feedback system. The proposed design is expected to be capable of delivering beams with the required characteristics to meet the performance goals for a new light source.

Disclaimer

This document was prepared as an account of work sponsored by the United States Government. While this document is believed to contain correct information, neither the United States Government nor any agency thereof, nor The Regents of the University of California, nor any of their employees, makes any warranty, express or implied, or assumes any legal responsibility for the accuracy, completeness, or usefulness of any information, apparatus, product, or process disclosed, or represents that its use would not infringe privately owned rights. Reference herein to any specific commercial product, process, or service by its trade name, trademark, manufacturer, or otherwise, does not necessarily constitute or imply its endorsement, recommendation, or favoring by the United States Government or any agency thereof, or The Regents of the University of California. The views and opinions of authors expressed herein do not necessarily state or reflect those of the United States Government or any agency thereof, or The Regents of the University of California. Ernest Orlando Lawrence Berkeley National Laboratory is an equal opportunity employer.

Content

1. Introduction
    1.1 Machine overview and design goals
    1.2 Main issues of beam dynamics
2. Longitudinal beam dynamics
    2.1 Longitudinal dynamics without collective effects.
    2.2 Longitudinal dynamics with collective effects.
        2.2.1 Longitudinal wake potentials
        2.2.2 Coherent synchrotron radiation
        2.2.4 Longitudinal space charge effects
        2.2.5 Microbunching instability
3. Transverse beam dynamics
4. Accelerator design
    4.1 Laser heater
    4.2 Bunch compressor
    4.3 Electron beam switch yard
        4.3.1 Design description
        4.3.2 Beam dynamics studies
    4.4 An active `management' system for bunch tails
5. Long range wake fields and beam break-up instability
    5.1 High-order modes
        5.1.1 Wake field of a single bunch
    5.2 Results of beam break-up studies
        5.2.1 Two linac sections model
        5.2.2 Five linac sections model
6 Start-to-end macroparticle tracking studies
7. Jitter studies
    7.1 Simulation technique
    7.2 Global jitter studies
    7.3 Time-dependent model
8. Conclusion
9. Acknowledgments
Appendix A: 6D parallel tracking code IMPACT
Appendix B: Vlasov solver
References

1 Introduction

1.1 Machine overview and design goals

This Report describes the design of the beam delivery system for a proposed soft x-ray free electron laser (FEL) or `Berkeley Free electron laser Array' (BFA) at the Lawrence Berkeley National Laboratory. The present work follows a long list of studies for FEL-based 4th generation light sources either proposed or already under construction or operation: *e.g.*, SLAC LCLS [Arthur *et al*.], DESY XFEL [Brinkman *et al*.], FERMI@elettra [Bocchetta *et al*.], MIT X-ray Laser Project [Moncton *et al*.], BESSY FEL [Kramer *et al*.], LBNL LUX [Corlett *et al*.], Daresbury 4GLS [Alexander *et al*.] and others. Designing this system we have borrowed many ideas proposed in the above publications and other related publications. While some of these ideas are reviewed here for completeness the focus of the Report is primarily on various concepts and issues that are specific to the envisioned BFA.

Given that BFA must operate as a user facility with high reliability, the underlining motive of our work was to produce a design with careful balance of technical difficulties of individual components that does not overly stress the state of the art of similar systems demonstrated elsewhere.

The basic functions of the beam delivery system described in this document are to accelerate electron bunches from 40 MeV to 2.4 GeV and manipulate the beam to achieve 1 kA peak current while preserving a low slice energy spread $\sigma_E \leq 100$ keV and low normalized slice emittance $\varepsilon_\perp \leq 1$ μm. An additional important demand on the accelerator is the delivery of beams with charge density and slice average energy that are as uniform as possible along the bunch core. Although the beam delivery system serves more purposes than just acceleration of electrons, in the following we will often refer to it more simply as the `accelerator' or `linac' for brevity.

The accelerator, schematically shown in Fig. 1.1, occupies the region between the injector and FEL undulators. The latter, not shown in the picture, are located at the exit of the spreader lines.

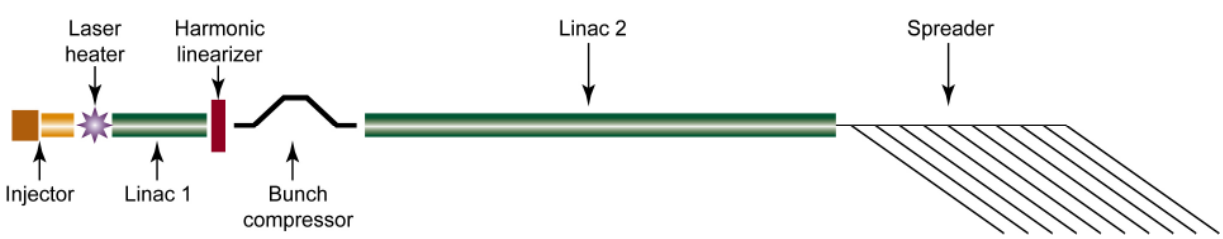

Figure 1.1: Schematic of the BFA accelerator. Elements of the accelerator include the laser heater (LH), first linac (L1), harmonic linearizer (HL), bunch compressor (BC), second linac (L2), spreader, and possibly a module for collimation of the bunch tails (not shown).

The laser heater (LH) is the first major subsystem along the accelerator. Located at the end of the injector and receiving ~40 MeV electron bunches with 60-70 A peak current it is used to adjust the beam uncorrelated energy spread. The LH is followed by the first linac (L1), a superconducting linac with 13.5 MeV/m accelerating gradient. Presently TESLA-style cryomodules hosting 1.3 GHz rf structures are proposed for L1. However, it is worth pointing out that cryomodules with 1.5 GHz rf structures under development for the CEBAF upgrade represent an equally viable alternative. The electron beam energy at the end of the L1 is ~ 260 MeV. L1 is followed by the harmonic linearizer (HL), a 5 MeV/m accelerating gradient, 3.9 GHz rf structure. The HL decelerates slightly the electrons and in combination with L1 imparts a linear energy chirp to the electron bunches before they enter the bunch compressor (BC). The BC, consisting of a magnetic chicane, compresses the electron bunches thus increasing the electron peak current up to 1 kA. The BC is followed by the second linac (L2) that accelerates electrons to approximately 2.4 GeV. The switch yard at the end of L2, the `spreader', distributes the electron bunches into ten independent FEL undulator lines. In addition to the above subsystems a module to provide controlled collimation of the bunch tails may be necessary. While the exact location of such a system is yet to be finalized, most naturally it would fit at the beginning of the accelerator to minimize the power deposition on collimators by stray electrons. The maximum bunch repetition rate in the machine is 1 MHz corresponding to a bunch repetition rate of 100 kHz for each of the 10 FEL lines operating simulataneously. A bunch repetition rate of 1 MHz in each FEL operating alone is also an option.

Three modes of operations are currently envisaged, which target the following scenarios: *i)* high-charge long electron bunches with bunch length between 100 and 600 fs; *ii)* medium-charge electron bunches with bunch length between 10 and 100 fs; and *iii)* low-charge short electron bunches with bunch length below 10 fs.

The electron beam delivery system is designed with sufficient flexibility to accommodate all the above options and produce the desired 1 kA peak current regardless of the bunch charge. The long-pulse mode of operation, which carries the highest bunch charge and, thus, expected to have the largest beam emittance produced in the electron gun, is in our opinion the most challenging for the beam delivery system. It will be the primary focus of this Report.

1.2 Main issues of beam dynamics

Intense electron bunches propagating along the accelerator are exposed to various collective effects. Sources of these collective effects include wake fields, space charge, and coherent synchrotron radiation (CSR).

Space charge manifests itself in both the transverse and longitudinal planes. Transverse space charge may affect the beam emittance at low energy. Longitudinal space-charge (LSC) effects are also stronger at lower energy but continue to have an impact on beam dynamics through much higher energies, particularly on a shorter length scale, and can be responsible for the appearance of microstructures within the electron bunches.

Longitudinal wake fields can chirp the electron bunch energy and produce nonlinear variation of the slice energy along the bunch. Transverse wake fields can affect the transverse emittance.

Also relevant for beam stability is the emission of coherent synchrotron radiation (CSR) in the bending magnets of the bunch compressors and spreader. In the absence of microstructures in the beam density, CSR produces effects very similar to those of longitudinal wake fields and contributes to the development of an energy chirp along the beam with possible consequences on the horizontal emittance. In addition, CSR can aggravate the presence of small fluctuations in the charge density and contribute to the development of the so-called microbunching instability together with the LSC. This has the effect of enhancing fluctuations in the beam density, generating energy modulations on a short length scale that can evolve into a large energy spread and/or fragmentation of the beam distribution in phase space.

The nonlinear curvature of the rf waveform and nonlinear terms in the transfer matrix through the bunch compressor relating a particle time-of-flight and energy are often responsible for the appearance of large spikes in the peak current at the head and tail of the electron bunches. A spike at the head of the bunch can induce resistive wall wake fields that can cause a nonlinear energy chirp along the electron bunch during its motion through the spreader and FEL undulator. The spike at the tail of the bunch can also induce a nonlinear energy chirp along the bunch due to the CSR in the spreader.

The machine design discussed in this Report accounts for all these effects as well as limitations arising from various engineering considerations. The choice of beam parameters for the three modes of operation mentioned at the end of the previous section reflects a careful balance between technological constrains and mitigation of adverse effects.

2 Longitudinal beam dynamics

The intensity of the bunch current at the exit of the injector is typically about an order of magnitude smaller than needed for lasing in FEL. A suitable manipulation of the beam longitudinal phase space along the beam delivery system is then necessary to meet the required current specifications. This can be achieved by using a series of rf accelerating sections and magnetic chicanes (henceforth called the “bunch compression system”) [Dohlus]. Ideally, this process should preserve the linearity of the longitudinal-energy correlation in order to avoid `bifurcations’ of the beam density in the longitudinal phase space which lead to high peak current spikes at the edges of the electron bunch (and reduce the number of electrons that can be effectively uililized in FEL). A uniform charge density profile is also desirable for the most efficient utilization of electrons in the FEL for a given bunch length. Finding an optimum set of design parameters is a rather complicated process and requires several iterations. Fortunately, an element of simplification is offered by the fact that for the most part the longitudinal and transverse dynamics are effectively decoupled and can be treated separately.

2.1 Longitudinal dynamics without collective effects.

As a first step toward a more complete analysis we start by considering the longitudinal dynamics in the absence of collective effects. In this approximation the longitudinal motion of an electron is determined by the energy variations relative to the reference particle as determined by the rf structures and the presence of dispersion. Because in the accelerator the motion is relativistic (E>40MeV) slippage of the electrons with respect to each other will be generally negligible in regions of vanishing dispersion. Fig. 2.1 shows the basic idea of a chicane-based bunch compressor.

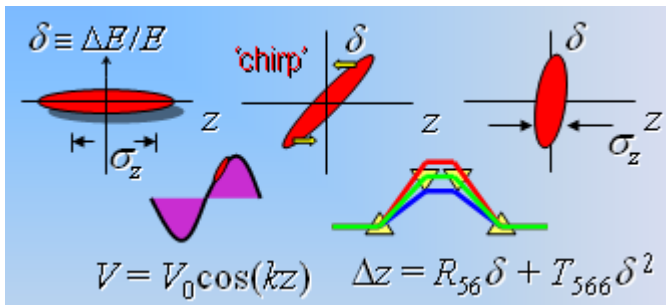

Figure 2.1: Schematic of compression of a chirped bunch through a magnetic chicane. The head of the bunch is at z<0.

The rf system accelerates the electron beam off-crest and generates a correlated energy variation (chirp) along the electron bunch. The momentum compaction, the R_{56} and T_{566} terms in the transport matrix, relates the electron energy and the trajectory path length in the chicane in such a way that higher energy electrons follow shorter paths and lower energy electrons follow longer paths. This correlation between energy and path length compresses the length of an electron bunch accelerated off-crest by the rf wave, as shown in Fig. 2.1 with the bunch head at $z < 0$. A more effective compression can be achieved [Dowell *et al.*] by correcting the second-order term in the rf waveform using a 3rd harmonic rf 'linearizing' cavity (in our case a 3.9 GHz structure).

The acceleration seen by the electrons upstream of BC as a function of the distance z of the electrons from the center of the bunch can be written as:

$$U(z) = U_0 \cos(kz) + U_1 \cos(kz + \phi_1) + U_3 \cos(3kz + \phi_3), \qquad (2.1)$$

where $k = 2\pi / \lambda_{rf}$ is the rf wave number and λ_{rf} is the rf wavelength for the basic 1.3 GHz linac. U_0 is the acceleration amplitude of the injector linac preceding the laser heater (see, Fig. 1.1) where acceleration is on-crest. U_1 is the acceleration amplitude of Linac L1 placed between the laser heater and the BC, with off-crest acceleration at phase ϕ_1 (defined with respect to the crest of the rf wave). U_3 and ϕ_3 are the amplitude and phase of the 3rd harmonic linearizer linac. The first, second, and third derivatives of $U(z)$ taken at the bunch center $z = 0$ can be written as:

$$U'(z=0) = -kU_1 \sin\phi_1 - 3kU_3 \sin\phi_3, \tag{2.2a}$$
$$U''(z=0) = -k^2U_0 - k^2U_1 \cos\phi_1 - 9k^2U_3 \cos\phi_3, \tag{2.2b}$$
$$U'''(z=0) = k^3U_1 \sin\phi_1 + 27k^3U_3 \sin\phi_3. \tag{2.2c}$$

The second derivative is zero if

$$U_3 = -\frac{U_0 + U_1 \cos\phi_1}{9\cos\phi_3} \tag{2.3}$$

This condition eliminates the quadratic energy chirp. At the same time the first derivative becomes

$$U'(z=0) = -kU_1 \sin\phi_1 + \frac{1}{3}k\left(U_0 + U_1 \cos\phi_1\right)\tan\phi_3. \tag{2.4}$$

A comparison of (2.2a) and (2.2c) shows that $U'''(z=0)$ can also be written as:

$$U'''(z=0) = -k^2U'(z=0) - \frac{8}{3}k^3\left(U_0 + U_1 \cos\phi_1\right)\tan\phi_3. \tag{2.5}$$

Having denoted with z_0 the longitudinal position of a particle within the bunch at the entrance of the accelerator we, combine Eq.'s (2.1) - (2.4) to obtain the following expression for the particle relative energy through Linac L1 and linearizer (the energy deviation is with respect to the nominal beam energy $E(0)$):

$$\delta \equiv \frac{E(z) - E(0)}{E(0)} = \left[-U_1 \sin\phi_1 + \frac{1}{3}\left(U_0 + U_1 \cos\phi_1\right)\tan\phi_3\right]\frac{kz_0}{U(0)} + \delta_0 = -hz_0 + \delta_0. \tag{2.6}$$

where δ_0 represents the uncorrelated energy spread and the third equality in the expression above defines the quantity h, the energy chirp along the electron bunch. Because the motion is ultrarelativistic the longitudinal coordinate of the electron remains unchanged $z = z_0$. At the exit of the BC, characterized by the momentum compaction R_{56} (we neglect the generally small nonlinear correction T_{566}) we have, using (2.6),

$$z_1 = z + R_{56}\delta = (1 - hR_{56})z_0 + R_{56}\delta_0. \tag{2.7}$$

We can then calculate the rms bunch length after the BC:

$$\sigma_z = \left\langle \left(z_1 - \langle z_1 \rangle\right)^2 \right\rangle = \sqrt{\left(1 - hR_{56}\right)^2 \sigma_{z0}^2 + \left(R_{56}\sigma_{\delta 0}\right)^2} \approx \left|1 - hR_{56}\right|\sigma_{z0}, \tag{2.8}$$

where σ_{z0} and $\sigma_{\delta 0}$ are the rms bunch length and uncorrelated energy spread before the BC. The compression factor is

$$C = \frac{\sigma_z}{\sigma_{z0}} \approx \frac{1}{|1 - hR_{56}|}. \tag{2.9}$$

The uncorrelated energy spread after compression is $C\sigma_{\delta 0}$. The compression is large when the denominator in (2.9) is small and for a given R_{56} it is highly sensitive to small variations of the rf phases and amplitudes. Fig. 2.2 illustrates the sharp dependence of C on ϕ_1 and ϕ_3.

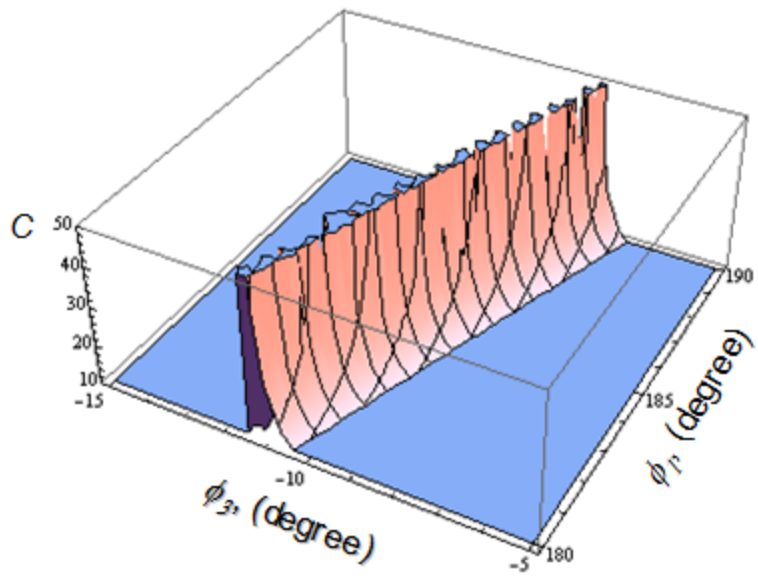

Figure 2.2: The plot shows the steep dependence of the compression factor C on the adjustable phases ϕ_1 (Linac L1) and ϕ_3 (harmonic linearizer) for fixed R_{56}.

2.2 Longitudinal dynamics with collective effects.

2.2.1 Longitudinal wake fields

A charged particle traveling through accelerating structures with velocity close to that of light *c* excites electromagnetic fields, called wake fields, that may affect the dynamics of a test electron trailing behind at distance $\hat{z}$. The longitudinal wake function $w(\hat{z})$ is defined as the voltage gain experienced by the test particle, typically given in units of voltage per unit length per unit charge [V/C/m] or in units of [V/C] to represent the voltage gain integrated over the length of a given device (*e.g.*, in our case a single accelerating module). Causality requires that the wake be zero if the test particle is in front of the source ($\hat{z} < 0$). For a given longitudinal charge distribution λ_z, the voltage gain experienced by a test electron located at *z* along the bunch due to the wake fields generated by all the leading electrons is given by the wake potential [Bane 2006]:

$$W(z) = \int_z^{\infty} w(z - z')\lambda_z(z')dz' . \tag{2.10}$$

An exact calculation of the wake function for an accelerating structure requires extensive numerical modeling. However, there exists a simple and convenient analytical formula that fits a numerical determination of the wakes on a short length scale quite accurately, which can be effectively used over longer distances and a wide range of parameters. [Novokhatski *et al*., 1996, 1999, Bane *et al.* 1998a, 1998b, 2003, 2006]:

$$w(\hat{z}) = -A\frac{Z_0 c}{\pi a^2}\left((1+\beta_0)\exp\left(-\sqrt{\hat{z}/z_0}\right) - \beta_0\right) \tag{2.11a}$$

where Z_0=377Ω is the vacuum impedance, and A, β_0 and z_0 are fitting coefficients. Typically $A \approx 1$ and z_0 is close to the value given by the following expression [Novokhatski *et al*., 1996]:

$$z_0 = 0.41 \frac{a^{1.8} g^{1.6}}{L^{2.4}}, \tag{2.11b}$$

where a, g, L are the geometric parameters defined in Fig. 2.3.

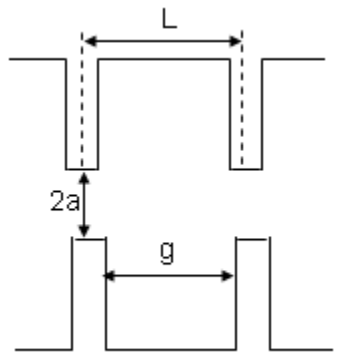

Figure 2.3: A schematic of one period of the accelerating structure.

Strictly speaking Eq. (2.11) only applies to a steady state situation. In general, it will take approximately the distance $a^2/2\sigma_z$ from the entrance of the accelerating section before the wake establishes itself as the steady state. It is easy to see that this distance is only about 0.5 m for a 1 mm long bunch and 3 cm iris radius, which is small compared to the rf structures, thus justifying our use of the steady state wake.

Specialized to 1.3 GHz acclerating structures the expression (2.11) for the wake function reads:

$$w(\hat{z})\left[\frac{V}{pC\,m}\right] = -38.1 \times \left(1.165 \times \exp\left(-\sqrt{\hat{z}/3.65[mm]}\right) - 0.165\right), \tag{2.12}$$

while for the 3.9 GHz accelerating structure we have:

$$w(\hat{z})\left[\frac{V}{pC\,m}\right] = -130 \times \left(1.02 \times \exp\left(-\sqrt{\hat{z}/3.65[mm]}\right) - 0.02\right). \tag{2.13}$$

Figures 2.4 and 2.5 show the good agreement between fitting formulas and numerical calculations in the two cases.

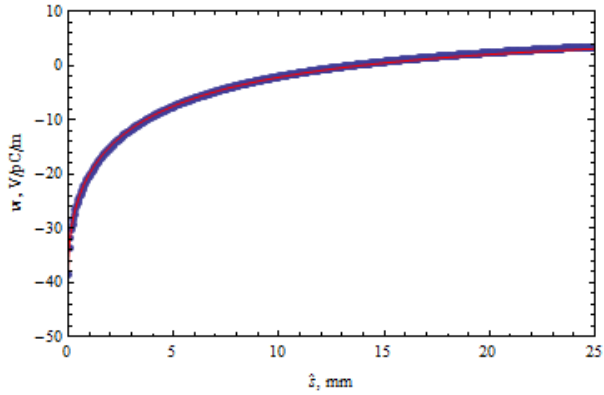

Figure 2.4: Longitudinal wake function for the 1.3 GHz accelerating structure as a function of the distance between source and test particles. The blue line is the result of numerical simulations, the red line represents the fit based on the analytical formula (2.12).

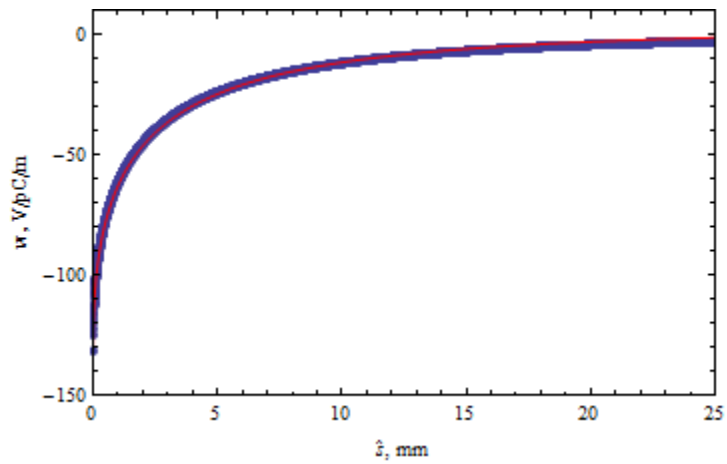

Figure 2.5: Longitudinal wake function for the 3.9 GHz accelerating structure as a function of the distance between source and test particles. The blue line is the result of numerical simulations, the red line represents the fit based on the analytical formula (2.13).

Next, we make use of the analytical expressions for the wake functions to calculate the energy loss experienced by an electron as a 1pC bunch travels through both the 25 m long, 1.3 GHz Linac L1 and the 4.5 m long, 3.9 GHz linearizer linac. We assume a parabolic longitudinal bunch density profile with 6 mm bunch length (measured at the base). The energy variation is obtained by carrying out a convolution of the bunch density with the wake function. The result is shown in Fig. 2.6.

The curve in Fig. 2.6 is well approximated by the following cubic fit:

$$\frac{\Delta E_1(z)}{e} = (a_3 z^3 + a_2 z^2 + a_1 z + a_0) Q \tag{2.14}$$

where e is the electron charge, Q is the total bunch charge measured in pC and $a_0 \approx$ -418 V/pC, $a_1 \approx 163$ V/pC/mm, $a_2 \approx 17.6$ V/pC/mm^2, $a_3 \approx$ -8.0 V/pC/mm^3.

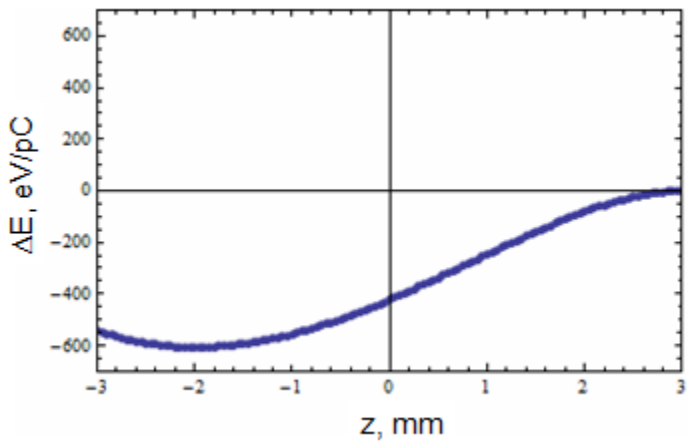

Figure 2.6: Rf wake-field induced energy loss by an electron with coordinate z along the bunch (z=0 is the bunch center). The energy loss is per unit of 1 pC bunch charge (see text for details) and is evaluated for a 6 mm long bunch with parabolic profile.

Now we can modify Eq. (2.3) to account for the effects of wake fields

$$U_3 = -\frac{U_0 + U_1 \cos\phi_1 - 2a_2 Q/k^2}{9\cos\phi_3} \tag{2.15}$$

and update the resulting expression for the linear energy chirp:

$$h = \left[U_1 \sin\phi_1 - \frac{1}{3}\left(U_0 + U_1 \cos\phi_1 - 2a_2 Q/k^2\right)\tan\phi_3 - a_1 Q/k \right] \frac{k}{U(0)}. \tag{2.16}$$

The cubic energy chirp defined by the third derivative in (2.2c) takes the following form:

$$U'''(z=0) = k^3 \left[U_1 \sin\phi_1 + 27 U_3 \sin\phi_3 + 6Qa_3/k^3 \right]. \tag{2.17}$$

As a numerical example consider the case $k = 2\pi/\lambda_{rf}$, $\lambda_{rf} \cong 230$ mm corresponding to 1.3 GHz rf frequency, $Q = 1$ nC and a typical accelerator set-up with ϕ_3=0 and energy chirp $ehU(0) = 0.5$ MeV/mm. From (2.16) we find $U_1 \sin\phi_1$=12.4 MV and compare it with $6Qa_3/k^3 \approx$ 2350 MV, which is the second non-zero term in (2.17). Cleary, we can conclude that the cubic nonlinearity in the energy chirp is largely dominated by the contribution from the longitudinal wake potentials. We should point out that the cubic nonlinearity in the energy chirp is often responsible for the appearance of bifurcations in the longitudinal phase space that become apparent after the beam passes the bunch compressor. These lead to the appearance of the characteristic spikes in the peak current at both edges of the electron bunch that are often observed in simulations. It is therefore desirable to minimize a_3. One way to achieve this is to use a longitudinal density distribution other than the parabolic density considered here (see, *i.e.* [England *et al.*, Cornacchia *et al.*]).

2.2.2 Coherent synchrotron radiation

In this section the effect of CSR is analyzed for the case of a smooth electron density distribution without microstructures. Radiation is coherent for frequencies $\omega \le c/\ell_b$, where c is the speed of light and ℓ_b is a characteristic length of the order of the bunch length [Derbenev *et al.* 1995]. In analogy with the effect of structure wake fields considered above, CSR causes a variation of the particle energy along the bunch.

Here we follow Ref. [Derbenev *et al.* 1995] to present a heuristic derivation of the CSR-induced force experienced by an electron along its direction of motion. The 1D beam is assumed to travel on a circular orbit of radius *R* at ultrarelativistic speed. See diagram in Fig. 2.7. The test particle at present time is located at *B* (the head of the bunch) while the whole bunch population is thought of as being concentrated at point *A* (the tail of the bunch) when the radiation now reaching *B* was emitted. Let θ be the angle between *A* and *B*. The condition that the tail radiation at a point *A* will overtake the head of the bunch at a point B at present time is:

$$z = arc(AB) - line(AB) = R\theta - 2R\sin(\theta/2) \approx \frac{1}{24}\theta^3 R\,, \qquad (2.18)$$

where z is the distance between the tail of the bunch and the test electron. Notice that in this section we adopt the convention that *z=0* at the bunch tail rather than at the bunch center. This condition determines two important geometrical parameters as functions of z:

$$\theta = 3^{1/3}\,2\left(\frac{z}{R}\right)^{1/3} \text{ and}$$

$$d = line(AB)\sin(\theta/2) = 2R\sin^2(\theta/2) = 3^{2/3}2\;z^{2/3}R^{1/3}$$

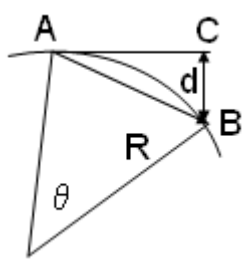

Figure 2.7: A geometrical diagram for an electron bunch motion in the bending magnet.

The magnitude of the transverse electric field which acts on the head particle can be estimated as the field of the charged line produced at the characteristic distance *d*:

$$E_\perp \cong \frac{2e\lambda_z}{d}\,, \qquad (2.19)$$

where λ_z is the electron density function normalized such as $\int_{-\infty}^{\infty}\lambda_z(z)dz = N$, where N is the number of electrons in the electron bunch. Because this field was radiated at a point *A*, its direction at a point *B* is perpendicular to the line (*AC*). Thus, the head particle experiences the acceleration force:

$$F_{\parallel}(\hat{z}) \cong e\,E_{\perp}\theta = \frac{2e^2\lambda_z}{d}\theta = \frac{2e^2\lambda_z}{3^{1/3}\hat{z}^{1/3}R^{2/3}}\,. \tag{2.20}$$

In the case of the long magnet with bending angle:

$$\varphi_M \;\geq \left(24\;\frac{\ell_b}{R}\right)^{1/3} \tag{2.21}$$

one can calculate an average rate of the energy loss per electron and per unit length of the trajectory:

$$\frac{dU}{ds} = -\frac{1}{N}\int_0^{\ell_b} dz\lambda_z(z)F_{\parallel}(z) = -3^{2/3}\,\frac{Ne^2}{R^{2/3}\ell_b^{4/3}}\,. \tag{2.22}$$

The integration was performed for a uniform flat-top density distribution $\lambda_z = N/\ell_b$. Remarkably this is the same result one obtains starting from the following more rigorous formula [Saldin *et al.* 1997]:

$$\frac{dU}{ds} = \frac{1}{N}\int_{-\infty}^{\infty} dz\lambda_z(z)\frac{dE(z)}{ds}\,. \tag{2.23}$$

The above equation is valid for an arbitrary longitudinal charge density λ_z where $dE(z)/ds$ is the energy variation per unit length experienced by an electron with coordinate z in the bunch, (also dependent on the profile of the longitudinal bunch density) , which reads

$$\frac{dE(z)}{ds} = -\frac{2Ne^2}{3^{1/3}R^{2/3}}\frac{1}{N}\int_{-\infty}^{\infty} dz'\frac{1}{(z-z')^{1/3}}\frac{\partial\lambda_z(z')}{\partial z'}\,. \tag{2.24}$$

We note that (2.22)-(2.24) are correct only if condition (2.21) is satisfied, *i.e.* the radiation of the tail particles overtakes the head particles before the electron bunch leaves the magnet. In reality, it was shown in Ref. [Saldin *et al.* 1997] that CSR continues to affect electrons in the drift past the bending magnet as CSR emitted by the electrons before the exit of the magnet catches up with the beam. However, the accuracy of the above equations tends to be acceptable when the condition (2.21) is not strongly violated.

Another potentially important limitation to the validity of the above formulas is given by the presence of the metallic boundaries from the vacuum chamber. The vacuum chamber acts as a waveguide for the radiation. Not all spectral components of CSR propagate in the waveguide and therefore the actual radiated energy is smaller than in free space. We use the recipe suggested in Ref. [Li R.] to estimate this reduction:

$$\Delta E_{\text{shielded}}/\Delta E_{\text{free space}} \cong 4.2(n_{th}/n_c)^{5/6}\exp(-2n_{th}/n_c), \qquad n_{th} > n_c\,. \tag{2.25}$$

Here $n_{th} = \sqrt{2/3}(\pi R/\Delta)^{3/2}$ is the threshold harmonic number for a propagating radiation, Δ is the total height of the vacuum pipe, and $n_c = R/\sigma_c$ is the characteristic harmonic number for a Gaussian longitudinal density distribution with σ_c rms length. For a uniform flat-top density distribution $\sigma_c \cong \ell_b/3.22$, with ℓ_b being the length of the flat

top part. The harmonic number n_c has the meaning of an approximate divider of the spectra of the electron bunch radiation into the part where radiation of all electrons in the electron bunch contribute coherently, *i.e.* the part with harmonic numbers less than n_c, and the part where electrons radiate incoherently, *i.e*. the part with harmonic numbers larger than n_c. Fig. 2.8 shows the calculated effect of the suppression of the CSR for the vacuum chamber with Δ=8 mm.

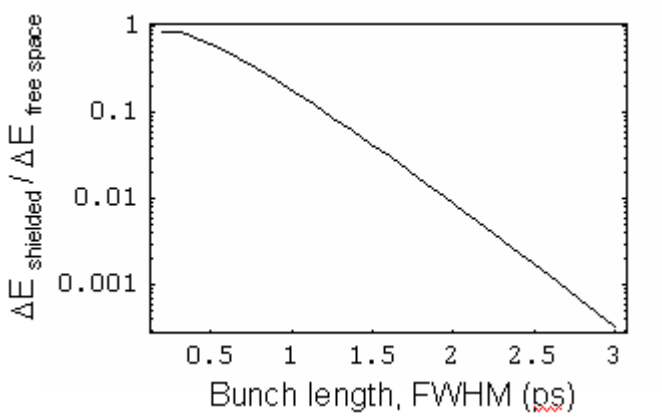

Figure 2.8: Suppression of CSR by the vacuum chamber shielding.

Let us first estimate the effect of CSR in the 4th magnet of the BC where the bunch length is shortest and is expected to be of the order of 0.5 ps (for a case of the high-charge long electron bunches). This magnet has a length L_M=0.25 m and a bending radius R=2 m. The calculation using a 1 nC bunch charge in (2.22) gives an average energy loss per electron in free space ~ 0.35 MeV. The arc angle of the magnet is just right to satisfy (2.21).

Now we want to estimate the energy variation along the electron bunch and compare the result with the similar variation caused by rf structure wakes. Using the electron density distribution shown in Fig. 2.9 (flat top with smooth transitions at the edges with characteristic width of ~ $2\sigma_0$ modelled by *erf* functions) we obtain:

$$\frac{dE(z)}{ds} = -\frac{2}{3^{1/3}} \frac{Ne^2}{R^{2/3}\ell_b} \int_{-\infty}^{z} \frac{1}{\sqrt{2\pi}\sigma_0} \left(e^{-\frac{z'^2}{2\sigma_0^2}} - e^{-\frac{(z'-\ell_b)^2}{2\sigma_0^2}} \right) \frac{ds'}{(z-z')^{1/3}}, \qquad (2.26)$$

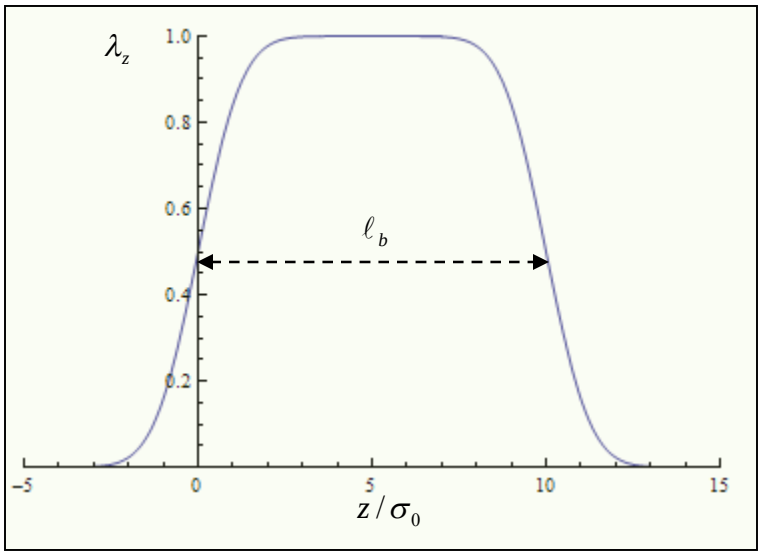

Figure 2.9: The longitudinal density of electrons (ℓ_b/σ_0 =10).

The integral (2.26) can be evaluated in a closed analytical form, but the expression is too long to report here. The plot of the energy modulation $L_M dE(z)/ds$ acquired by a 0.5 ps long electron bunch with 1 nC bunch charge through the same bending magnet as in previous example is shown in Fig. 2.10.

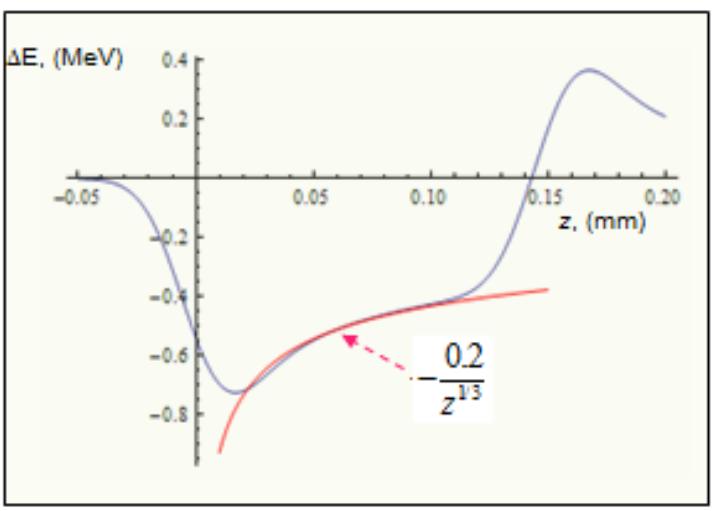

Figure 2.10: Energy loss/gain due to CSR as a function of the electron position within the electron bunch with the density distribution from Figure 2.9 (see text for a description of beam and bend magnet parameters). The red line shows the fitting function.

We note that $\Delta E(z) \sim \mu / z^{1/3}$ over the central part of the electron bunch ($\mu \approx 0.2$ MeV·mm$^{1/3}$). One can also see that the entire span of the energy variation in the central part is of the order of 0.2 MeV. A meaningful comparison with the energy variation induced by rf wakes can be done by considering the cubic component of the structure

wake field in Eq. (2.14), which is the dominant nonlinear term contributed by Linac L1 after the quadratic component is removed by the linearizer. Specifically, the 3rd-order term in Eq. (2.14), evaluated for a 1 nC bunch yields about a 0.4 MeV energy variation over the bunch length (this is for the 6 mm long bunch with parabolic profile to which Eq. (2.14) applies).

2.2.3 Longitudinal space charge effects

In addition to rf-structure wake fields and coherent synchrotron radiation a third important source of collective effects is represented by space charge. Its actual relevance is strongly dependent on the scale length of interest. On longer scales comparable to the bunch length, the effect of space charge is preponderant in the injector at low energy but it quickly weakens as the beam transitions into the accelerator starting at 40-50 MeV energy. Starting from this energy range its impact on the evolution of the beam tails in the longitudinal phase space becomes typically quite modest. The reason is the strong dependence ($\sim 1/\gamma^2$) of space-charge forces on energy at low frequencies. For example, based on the longitudinal space-charge impedance model (2.27) discussed below and the same flat-top beam profile with smooth ends considered in the previous section, one finds peak energy variations through the beam tails of the order of 6 keV/m when γ=80 and the transverse radius r_b =0.5 mm.

On the other hand space charge remains quite relevant through much higher beam energies when one is concerned with microbunching effects occurring on much shorter length scales (typically from about 100 μm down to 1 μm or less). In this range space-charge forces when integrated over the length of the machine are typically larger than those caused by either the rf-structure impedance or those induced by CSR. A detailed discussion of the microbunching instability is deferred to the next section. Here we discuss 1D models of longitudinal impedance that can be used with various degree of accuracy to assess the effect of space charge. Handy analytical expressions can be obtained if one considers beams with circular cross section of radius r_b and uniform transverse density. The impedance (per unit length) yielding the longitudinal electric field at radial position r for such beams in response to a longitudinal beam density modulation with wavelength k reads [Rosenzweig]

$$Z(k,r) = \frac{iZ_0}{\pi k r_b^2}\left[1 - \frac{kr_b}{\gamma} K_1\left(\frac{kr_b}{\gamma}\right) I_0\left(\frac{kr}{\gamma}\right)\right], \tag{2.27}$$

where K_1 and I_0 are the modified Bessel functions. The expression one obtain from (2.27) when specialized to on-axis fields (*i.e.* r=0, yielding $I_0(kr/\gamma)$=1) is often used and gives a good approximation of the longitudinal electric field over the entire transverse cross section provided that the ratio $kr_b/\gamma << 1$, *i.e.* the wavelength is large compared to the transverse radius reduced by the relativistic γ factor. In this limit

$$Z(k, r=0) \approx \frac{iZ_0 k}{4\pi\gamma^2}\left[1 - 2\log\left(\frac{kr_b}{\gamma}\right)\right], \tag{2.28}$$

displaying explicitly the dominant $\sim 1/\gamma^2$ energy dependence mentioned earlier. In the same limit the above expression can be used to represent the electric field generated by beams with different shape of transverse density, provided that one interprets r_b in a suitable way. For example, the on-axis electric field generated by a beam with Gaussian transverse density with rms widths σ_x and σ_y in the horizontal and vertical plane respectively can, to a good approximation [Venturini 2008], still be represented by (2.28) with $r_b = 1.747(\sigma_x + \sigma_y)/2$. At smaller wavelengths when the ratio kr_b/γ approaches or exceeds unity the longitudinal electric field across the transverse direction becomes less uniform, tapering off toward the beam edges. A better model is then obtained by averaging (2.27) over the transverse density of the beam. For beams with circular cross section and uniform transverse density this averaging yields

$$Z_{avg}(k) = \frac{iZ_0}{\pi k r_b^2}\left[1 - 2K_1\left(\frac{kr_b}{\gamma}\right)I_1\left(\frac{kr_b}{\gamma}\right)\right]. \tag{2.29}$$

Fig. 2.11 shows a numerical test where the two models of Eq. (2.27) and (2.29), with the impedance in the first equation evaluated on-axis $r=0$, are compared against the more accurate prediction one obtains by numerically solving the Poisson equation for a macroparticle distribution representing a transversally uniform beam with circular cross section. The quantity reported in the graph is the rms energy spread developed as a consequence of the LSC electric field as the beam travels with constant energy through a 3 m drift. Notice that indeed the model (2.27) yields a larger estimate at smaller wavelengths than (2.29). The latter is seen to track more closely the result of the calculation carried out with IMPACT (dots) [Qiang *et al*. 2000] (see also Appendix A).

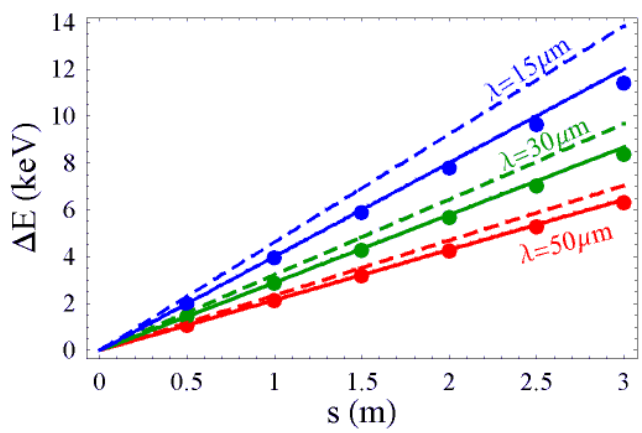

Figure 2.11: Amplitude of energy modulations as a function of distance induced by space charge starting from an initial 5% sinusoidal modulation of beam current with wavelengths λ=15 μm, 30 μm, and 5 μmm. Without modulation the beam has a longitudinal smooth flat-top profile with I=120 A peak-current and it drifts in free space at 120 MeV energy. The initial transverse density is uniform with circular cross-section of radius r_b=200 μm, and has vanishing transverse emittance and initial slice energy spread. The results from IMPACT simulations (dots) are compared to the longitudinal space-charge impedance models of Eq. (2.27) *with r=0, dashed lines, and the more appropriate Eq.* (2.29)*, solid lines.*

The numerical test shown in the picture is for a density perturbation that while is modulated longitudinally is uniform transversally. The case where one allows for density fluctuations across the transverse plane of the beam distribution is unfortunately not captured but these 1D models of space charge and accurate modeling require high-resolution computationally intensive macroparticle simulations. There is some evidence from early commissioning experience in LCLS that such fluctuations may be responsible for unexpectedly large coherent signals detected in the beam diagnostics [Ratner]. However the problem of the exact origin of these signals is still unresolved.

2.2.5 Microbunching instability

So far we have considered collective effects on a typical scale of the order of the electron bunch length. We showed that on this scale the CSR induces smooth energy variations along the electron bunch comparable to those induced by the wake fields from the rf-structures. We also showed that longitudinal space-charge effects (LSC) on a smooth beam density distribution in the linac proper are generally weak. The situation becomes quite different on a scale much smaller than the bunch length.

First of all, as far as CSR is concerned, shielding by the vacuum chamber will be largely ineffective on this scale and any microstructures present in the longitudinal beam density will essentially cause the same CSR effects as in a free space. One can then exclude the possibility of invoking a suitable design of the vacuum chamber to provide effective shielding. Secondly, the presence of microstructures in the bunch will cause the electric forces due to LSC also to become significant. The peak magnitude of these forces is generally smaller than those associated with CSR but their integrated effect over the length of the linac can actually be significantly larger. The longitudinal electric fields due to LSC and CSR will then contribute to the creation of energy modulations within the electron bunches. Their presence is responsible for the onset of what has become known as the `microbunching instability' [Saldin *et al*. 2002, 2003, Borland *et al.* 2002, Huang *et al*. 2004, Heifets *et al*.] The mechanism for this instability is very similar in its nature to the process of self-amplified spontaneous emission in FELs. Small density fluctuations present in the beam when it is first generated will start to seed energy modulations as a result of LSC. Once the beam traverses a bending magnet, for instance a dipole in a magnetic chicane used for bunch compression, further energy modulation is added by CSR and, more critically, a finite dispersion will turn the energy modulations into larger density fluctuations which in turn will result in even larger energy variations. Within one chicane or a sequence of chicanes this cycle can rapidly escalate and yield a significant amplification of the initial perturbation present in the beam. Thus the entire machine acts as a gigantic noise amplifier with possible serious consequences on the quality of the longitudinal phase space of the beam at exit. This is a rather fundamental instability in that density fluctuations when the beam is first generated are unavoidable. The most fundamental source of these fluctuations is the shot noise due to the discreteness of the electron charge. The random arrangement of electrons within a beam distribution creates charge density fluctuations that for typical bunch populations are fairly small but can nonetheless be amplified to unacceptable degree if the gain of the instability is particularly high. In addition to shot noise other sources of undesired

perturbations are irregularities on the surface of the cathode or uncontrolled fluctuations in the laser pulse in the photo-gun. Features of a beam affected by the microbunching instability at the exit of the linac are large charge-density fluctuations at the μm level, a large uncorrelated energy spread, energy modulations, and generally an irregular fragmentation of the longitudinal phase space. These features can compromise the performance of the FELs if not preventing lasing altogether. In particular, various seeding techniques that are meant to improve the temporal coherence of the radiation output pose stricter requirements on the longitudinal uniformity of the beam distribution and make the FEL performance more sensitive to any possible instability.

There are a few ways one can control the microbunching instability. At the level of lattice design one precaution is to limit the recurrence of dispersive regions. For example, using a single chicane is generally preferable to using two distinct chicanes (for an equal compression factor). Moreover, maximizing R_{56} in the relatively low-energy sections of the machine where the magnetic compressors are located can help suppress the higher frequency components of the instability. However, in the high-energy sections of the machine where the spreaders are located and the relative energy spread is small minimizing R_{56} may be helpful. Still, these lattice-design measures can be insufficient to control the magnitude of the instability or may not be feasible because of other considerations. In this case a further remedy one can adopt is to widen the uncorrelated energy spread right after the injection by use of the so-called 'laser-heater', as an increased energy spread at injection into the accelerator effectively reduces the instability gain. All the designs of x-ray FEL facilities either proposed or under construction have provisions for a laser heater located early on in the accelerator. The functioning of the laser heater and optimization of its tuning will be discussed in some detail in Sec. 4.1 and 4.2.

The very nature of the instability makes its modeling a quite delicate endeavor. One severe demand imposed upon particle-tracking simulations is the requirement of a large number of macro-particles to avoid spurious large random fluctuations that may seed the instability. To illustrate the problem consider a model of gain function $G(k)$ for the microbunching instability that vanishes everywhere outside a frequency band $\Delta k=k_{max}-k_{min}$ where it has the uniform value G_0. (Indeed, the features of this model are not too different from those of the gain curve of the actual physical system, *e.g.* see Fig. 6.7). Also, consider a model of flat-top bunch with L_b length. The shot noise due to the discreteness of the elementary charge presents a uniform power spectrum $\sim(N_b)^{-1/2}$ where N_b is the number of particles in the bunch. One can easily recognize that the components of the Fourier spectrum in the band Δk amplified by the instability will contribute to the development of a relative rms charge density fluctuation given by

$$b = \frac{\left\langle (\Delta\rho)^2 \right\rangle^{1/2}}{\rho} = G_0 \sqrt{\frac{2L_b}{N_b}\frac{\Delta k}{2\pi}} \approx G_0 \sqrt{\frac{2}{N_{\lambda\,\min}}} \qquad (2.30)$$

The last equality follows from the assumption that the bandwidth of the gain be sufficiently broadband $k_{max} >> k_{min}$, which is certainly true for the microbunching instability. In this case $\Delta k=k_{max}-k_{min} \sim 2\pi/\lambda_{min}$. The minimum wavelength $\lambda_{min} =2\pi/ k_{max}$ is determined by the presence of smoothing mechanisms due to a finite energy spread and transverse emittance, that tend to suppress small-scale density fluctuations. The quantity

$N_{\lambda min} = N_b(\lambda_{min} / L_b)$ has the physical meaning of number of electrons contained in a beam segment of length λ_{min}. For a bunch with peak current $I_b = 75\ A$ and assuming a maximum gain $G_0=50$ and wavelength cut-off $\lambda_{min} \sim 150\ \mu m$ (these values are read off the gain curve of the microbunching instability through the bunch compressor for the lattice considered in Sec. 6) the above formula gives a modest b =0.46%. The number of electrons in a *1.5* mm long beam with the above peak current is $N_b = 2.3 \times 10^9$. If we were to simulate the dynamics of such a beam using $N_{mp}=10^6$ macroparticles we would overestimate the amplitude of the initial shot noise and the relative density fluctuations by a factor $\sqrt{N_b / N_{mp}} \sim 50$, corresponding to a much larger b =23% bunching.

For certain purposes making simulations of the microbunching instability with a relatively small number of macroparticles may still be useful. For example, the tracking code ELEGANT [Borland 2000] has been successfully used to determine the gain curve for the instability using a number of macroparticles significantly smaller (up to N_{mp} = 60 M) than the bunch population. This was done by a judicious use of low-pass filters [Borland 2008]. Quiet-start techniques to reduce the unphysical component of shot noise, which have proved quite successful for studies of beam dynamics in FELs could also be applied in principle to the beam dynamics in accelerators. However, our preliminary attempts to experiment with these techniques have not yielded satisfactory results. A more straightforward and robust path toward increasing the accuracy of the simulations is to employ a larger number of macroparticles. This is the path we decided to pursue by continuing the development of the code IMPACT [Qiang *et al*. 2000] (see also Appendix A) By taking advantage of the multi-processor large-scale computing resources made available at the National Energy Scientific Computing Center (NERSC) through the INCITE project [NERSC] we have routinely been able to carry out simulations with one billion macroparticles (a number comparable to the population of the electron bunches of interest), with computer job runs typically taking a few hours.

The relevance of the microbunching instability and the importance of using a large population of macroparticles in the simulations is illustrated by the study summarized in Fig. 2.12. Here we show the electron distribution in the longitudinal phase space at the end of the linac designed for the x-ray FEL at FERMI@elettra [Bocchetta *et al*.]. The picture contains the superposition of the three simulations. In the first simulation (blue points) the electron bunch was tracked through the linac while the LSC and CSR effects were turned off. Here we see that the final electron distribution has a smooth shape and a fairly small energy spread. In the second and third simulations the LSC and CSR effects were turned on and the results were obtained using 10^7 (red points) and 10^9 (green points) macroparticles per bunch. Clearly, the LSC and CSR effects significantly degrade the beam quality and yield a much larger uncorrelated energy spread accompanied by beam fragmentation in the phase space. The simulation carried out with a large number of macroparticles clearly shows less degradation.

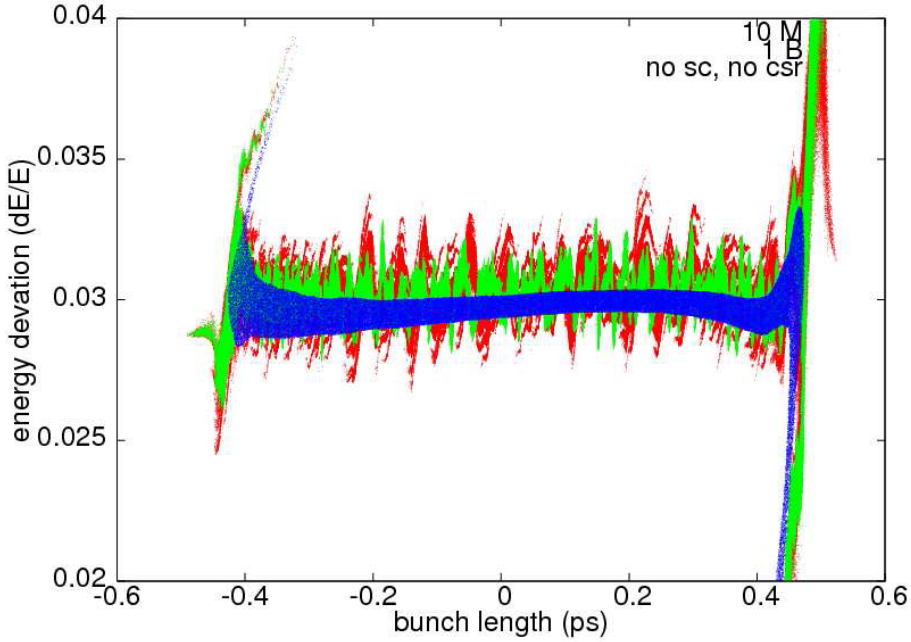

Figure 2.12: The electron distribution in the longitudinal phase space at the end of the linac for FERMI@elettra FEL obtained in simulations using 10 million (red data points) and one billion macroparticles (green data points). Blue data points show simulation without the LSC and CSR effects.

In addition to macroparticle simulations we have also pursued an alternative approach based on the use of grid-based direct methods to solve the Vlasov equation describing the beam dynamics [Venturini *et al.* 2007a, 2007b]. The beam density in phase space is represented on a grid and therefore is immune to sampling noise that occurs when the number macroparticles is significantly smaller than the bunch population. Advancement of the beam density is then done by repeated application of interpolations schemes. To keep errors under control and avoid undesirable deviations from physical behavior (*e.g.* the beam density going negative) one has to use sufficiently fine meshes. Still, the performance of direct Vlasov solvers compare favorably with macroparticle simulations, at least in a low-dimension phase space. The solver we have developed, which is described in more detail in Appendix B, is applicable to the longitudinal phase space and captures all the basics physics features of the microbunching instability. While the modeling of the physics is necessarily more approximate than the modeling that can be implemented in macroparticle/PIC codes (*e.g.* the effect of space charge is represented by an impedance rather than by solutions of a full 3D Poisson equation) the code execution time is much shorter (a few minutes on a desktop). This makes it particularly suitable for carrying out parameter or optimization studies and to assist with the understanding of the general features of the microbunching instability. A demonstration of the power of the Vlasov solvers, is shown in Fig. 2.13, highlighting the capability of the method for high resolution studies of the longitudinal phase space. These are density plots of the longitudinal phase space in the presence of a particularly strong instability (example taken from our studies of the FERMI@elettra project). By the exit of the second bunch compressor in one of the lattices we considered the beam is seen to have

developed noticeable microstructures in the form of density stripes almost collinear with the bunch (picture to the left). These stripes contribute to a large slice energy spread and also contribute to a charge density modulation that, by the end of the accelerator, is mapped by LSC into the additional energy modulation apparent on the 5-10μm length scale in the picture to the right.

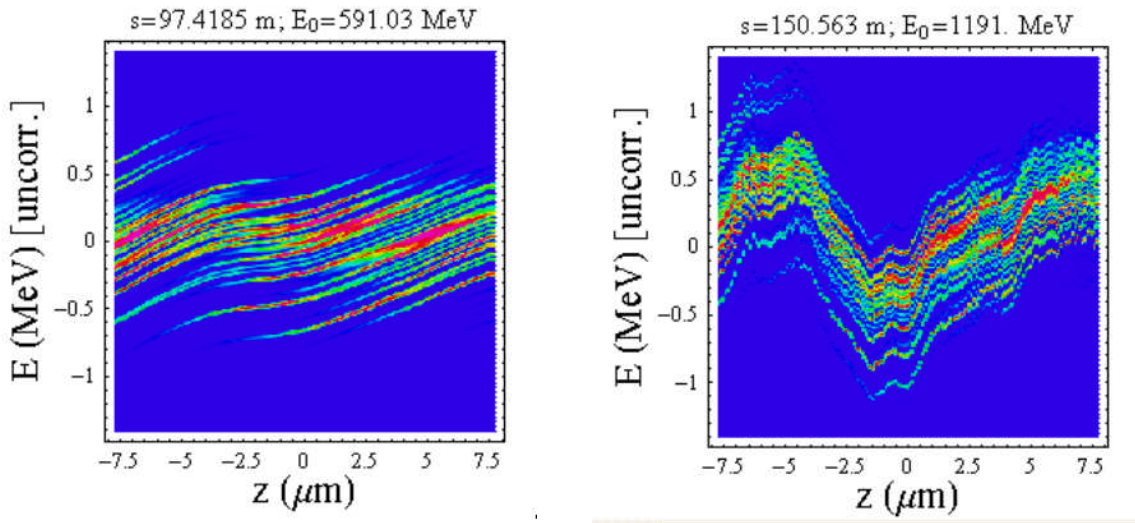

Figure 2.13: Two small sections of the electron distribution in the longitudinal phase space obtained using Vlasov's solver for analysis of the microbunching instability in the FERMI@elettra accelerator. Left plot is taken at the end of the second bunch compressor and right plot is taken at the end of the beam switch yard.

Finally, among the various tools at our disposal for characterizing the microbunching the instability we should mention the semi-analytical methods [Heifets *et al*.] for solving the linearized Vlasov equation. In fact it was on the basis of these methods that an appreciation of the relevance of the instability started to emerge, first at DESY [Saldin *et al*. 2002, 2003] and later at SLAC for the LCLS project [Huang *et al*. 2004]. In particular linear theory can be used to determine the gain curve of the instability which contains essential information for its characterization. Linear theory also offers useful bench-marks for validating the numerical methods used in the simulations.

During our studies we made several attempts to cross validate the various tools we used. We found good convergence between linear theory and numerical Vlasov methods in the small-amplitude regime where linear theory applies. We also found generally good agreement between the spectral content of the instability as predicted by high-statistics macroparticle simulations and the Valsov methods (both linear and nonlinear). However, the latter consistently seem to overestimate somewhat the magnitude of the instability compared to macroparticle simulations. The various approximations involved in the LCS impedance model used in the analytical models are the most likely cause of the discrepancy.

3. Transverse dynamics

Single-particle transverse dynamics through the linac is not expected to pose any unusual challenges, although care will have to be taken to estimate possible particle losses and position the collimators appropriately to protect the machine. A discussion of these issues however is beyond the scope of the present study. Transverse collective-force perturbations to the single-particle dynamics are also expected to be mild and certainly not as important as collective effects in the longitudinal phase space. Potential sources of collective perturbation to the transverse dynamics include transverse rf wake fields, CSR, and space charge. Because of the low frequency of the SC rf structures to be adopted in the BFA transverse wake fields are expected to have a relatively tame effect in comparison to those originating from normal conducting linacs. We did not include them in our present study but a closer look is in our plans for the future. Their effect on multi-bunch dynamics is investigated in some detail in Sec. 5.

As for CSR, the energy variation it induces along the bunches as the beam traverses a dipole (*e.g.* in the magnetic chicane) couples to the transverse dynamics through dispersion and generally results into a growth of the projected horizontal emittance. The projected emittance growth could be substantially suppressed by employing a double-chicane magnetic compressor with the two chicanes separated by a π phase advance in the horizontal betatron motion [Emma *et al.* 1998]. However, this may not be necessary (and may also be undesirable because of other considerations) as a careful design of a single-chicane bunch compressor can be successful at keeping the effect under control. We will touch again on this effect briefly in Sec. 4.2.

Space charge is critically important in the injector, where it largely determines the minimum achievable emittance, but it continues to play a role through the low-end energy of the linac in spite of the relatively high energy (>40MeV) because of the high particle density. One of the consequences of space charge is to modify the matching conditions for injection of the beam into the linac. An estimate of the effect can be made by comparing the space charge and the emittance terms in the equations governing the evolution of the rms envelope equations. Following Ref. [Sacherer], assume that the bunch density carries an elliptical symmetry (*i.e.* the density is a function of $x^2/a^2 + y^2/b^2 + z^2/c^2$) the equation of motion for the rms transverse envelope (say in the horizontal plane, σ_x) in the relativistic limit $\gamma_0 >> 1$ can then be written as

$$\sigma_x'' + k_x\sigma_x - \frac{\varepsilon_x^2}{\sigma_x^3} - \frac{N_b e^2}{4\pi\varepsilon_0 mc^2\gamma_0^3}\frac{3\lambda_3}{2\sigma_x\sigma_z} = 0\,, \tag{3.1}$$

where we also assumed, for simplicity, that the beam is axis-symmetric ($\sigma_x=\sigma_y$) and that the longitudinal length is much larger that the transverse sizes $\sigma_z>>\sigma_x$). The coefficient λ_3 depends on the form of the charge density. For a Gaussian density we have $\lambda_3 = 1/6\sqrt{\pi}$ and the space-charge term (last monomial on the LHS of Eq. (3.1)) can also be written in terms of the bunch peak current I as $I/2\sigma_x\gamma_0^3 I_A$, where I_A is the Alfvén current. The ratio of this quantity to the emittance term (third monomial in the LHS of Eq. (3.1)) gives a measure of the relative importance of space-charge forces. With the

following choice of parameters I=70 A, E=40 MeV, ε_x=1 μm and β_x = 10 m this ratio is 2.3 indicating that space charge is noticeable. Thus, avoiding emittance growth in the low-energy part of the linac requires careful matching of the electron beam transverse distribution with the lattice. Even if the beam is properly matched, emittance degradation can still occur because of the nonlinear nature of the space-charge forces. Macroparticle simulations are needed to assess this effect. An exhaustive investigation will require simulations in which the beam dynamics trough the injector is combined with that of the linac. At this stage of our study we limited ourselves to an investigation of rms emittance evolution through the first few meters of the linac starting from E=40MeV. Evidence of emittance growth is apparent from the macroparticle simulation results shown in Fig. 3.1. Here we compare two lattices encompassing the first portion of the linac, both including a chicane for the laser heater, which will be discussed in detail in Sec. 4. In both cases the beam is injected with 40 MeV energy. One lattice is longer by about 20 m as it includes an additional beamline at 40 MeV beam energy designed to host the longitudinal collimator discussed in Sec. 4.4.

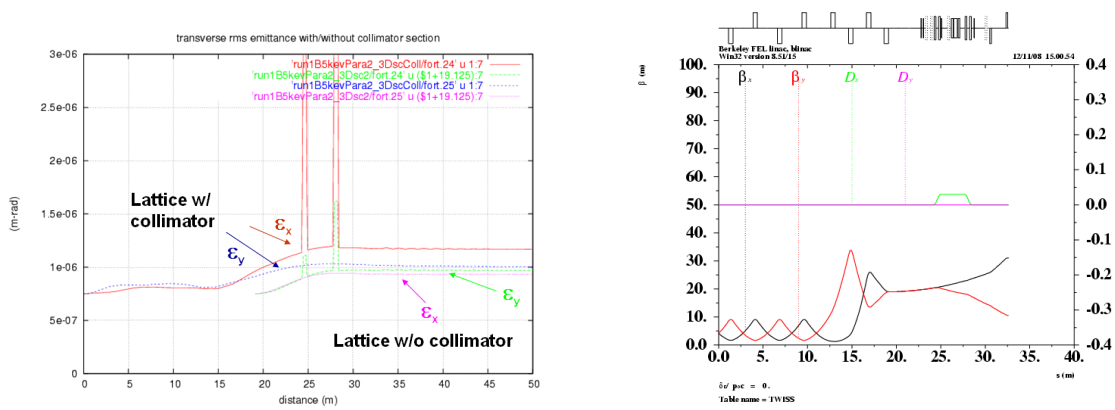

Figure 3.1: Picture to the left: evolution of the horizontal and vertical rms emittance. Two lattices are compared. The longer lattice includes an additional 20 m beamline at constant E=40MeV energy. The lattice functions for the first 32 m of the longer lattice are shown in the picture to the right.

In both cases the distributions of the injected beam have an initial normalized 0.75 μm rms emittance and are somewhat matched to the lattice. However, the matching is carried out using two different procedures. For the case of the longer lattice, which begins with two identical FODO cells, first a periodic solution to the rms envelope equation in the presence of space charge matched to the two FODO cells is found and these envelopes are used to define the beam distribution to be injected. In the case of the longer lattice we started with an initial beam distribution matched to the unperturbed lattice (no space charge) and then modified the setting of some selected quadrupoles to obtain the target beam envelopes at the end of the lattice.

The shorter beamline shows the emittance approaching 1 μm in both planes (the spikes observed in the figure between s=20 and 30 m are a spurious artifact and should be ignored). Not unexpectedly the emittance growth experienced by the beam through the

longer lattice is larger (particularly in the horizontal plane). Some portion of this emittance growth is likely to be due to the imperfect matching and can perhaps be avoided but it is clear that the growth observed in these simulations is not desirable.

An obvious remedy to the space charge induced emittance growth is to decrease the transit time of the beam at lower energy. This could be achieved by moving the laser heater along the linac to higher energy while at the same time accelerating the beam in the section of the beamline that provides the matching between the module for longitudinal collimation and the rest of the linac. Fig 3.2 shows that lattices (see Fig. 3.3) providing this acceleration can indeed reduce the emittance degradation due to space charge.

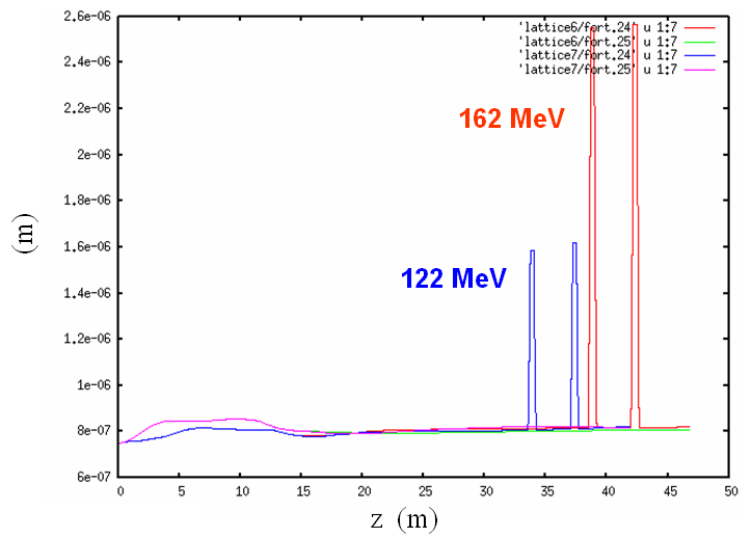

Figure 3.2: Evolution of the horizontal and vertical rms emittance for the two lattices reported in Fig. 3.3. A more rapid acceleration is shown to reduce emittance growth due to transverse space charge (compared to Fig. 3.1).

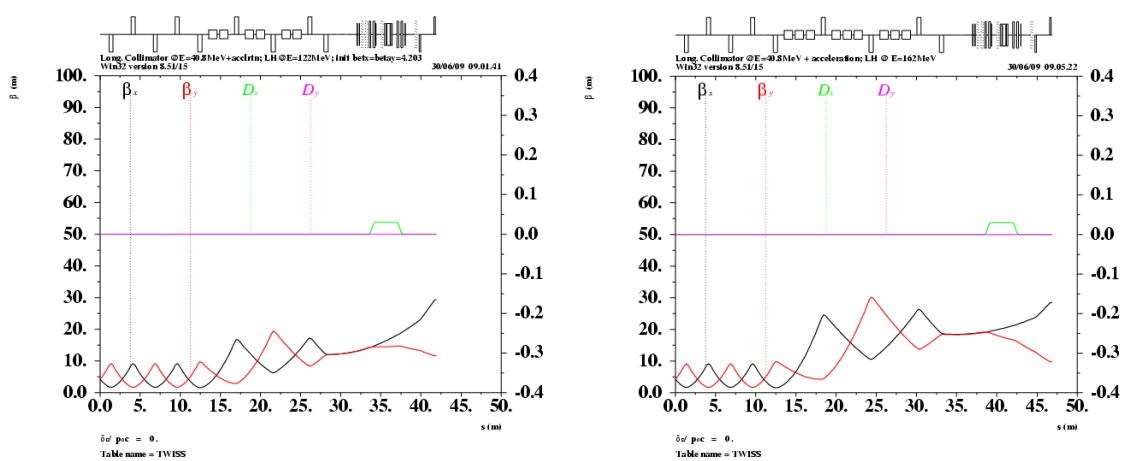

Figure 3.3: Variants of lattices for the low-energy end of the linac used in the emittance study reported in Fig. 3.2. In the lattice to the left, which is slightly shorter, the laser heater is located at E=122MeV beam energy; in the lattice to the right at E=162MeV.

A more definite answer to the problem of the transverse space-charge effects on the beam will have to wait more complete simulations including the injector once the design of the latter has been finalized.

4. Accelerator design

In this section we describe a complete baseline lattice design for the entire machine, presenting the overall layout and a discussion of individual machine sections. Fig. 4.1 shows the Twiss functions through the linac, together with an indication of the major components: the accelerator begins with the laser heater (LH), followed by the first linac (L1), harmonic linearizer (HL), bunch compressor (BC), second linac (L2), and spreader.

Notice that the layout shown in the picture does not include the module for collimation of the longitudinal charge density, which will be discussed in Sec. 4.4.

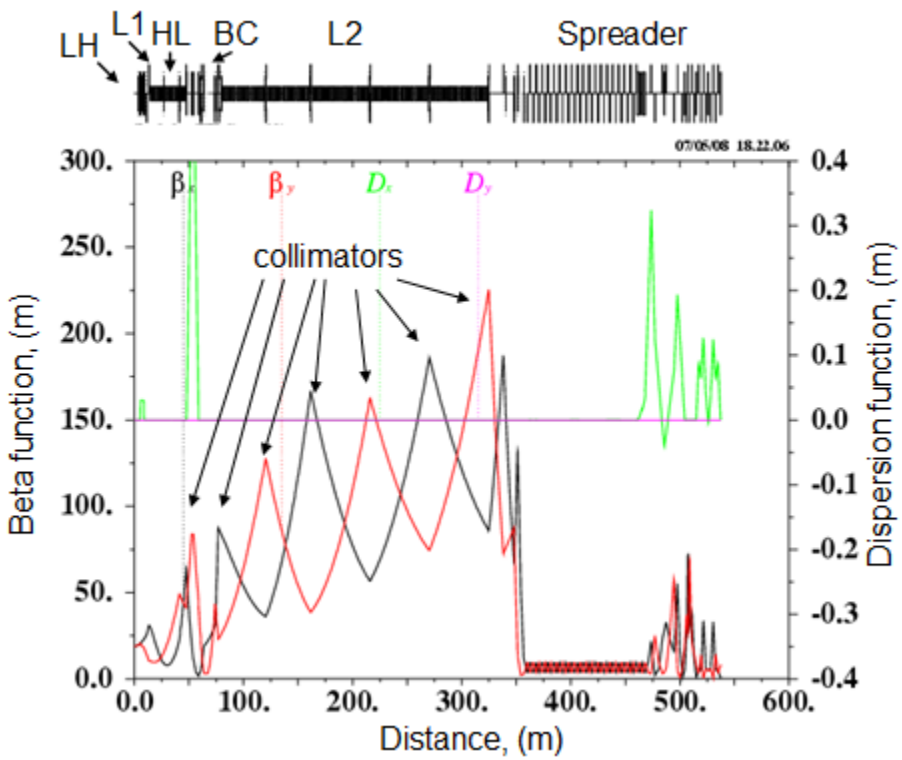

Figure 4.1: Twiss functions along the accelerator.

4.1 Laser heater

The gain of the microbunching instability is very sensitive to the uncorrelated energy spread in the electron beam. A modest increase in the uncorrelated energy spread can be sufficient to weaken the instability because of the "Landau damping" effect. Thus, the concept of a "laser heater" was proposed [Saldin *et al.* 2003] and adopted [Huang *et al.*

2004, Spampinati *et al.* 2007] in order to have an efficient control over the uncorrelated energy spread and the capability to increase it manyfold above the typically small value at the exit of the injector. A detailed description of the laser heater is given in Ref. [Emma *et al.* 2009]. For the purpose of this Report it will suffice to assume that the action of the laser heater is equivalent to contributing a certain amount of energy spread to be added in quadrature to the existing beam uncorrelated energy spread at the entrance of the accelerator.

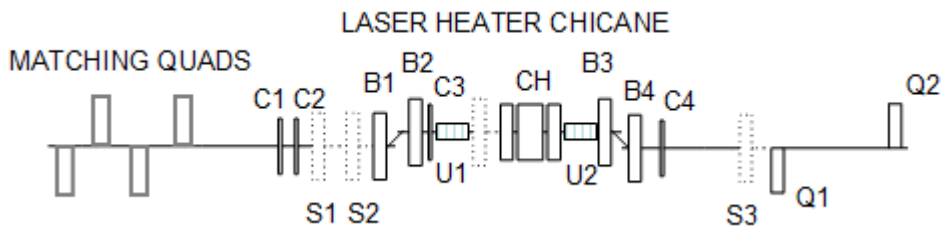

Figure 4.2: Schematic of the laser heater .

Fig. 4.2 shows the schematic of the laser heater section. It includes the laser heater chicane, two short undulators inside the chicane, a small diagnostics chicane (CH), four upstream and two downstream quadrupoles, four x-y correctors (C1-C4), optical transition radiation monitors (S1-S3), four BPMs (not shown), bunch current and bunch arrival-time monitors (not shown). Normally, four upstream quads will be used to match the Twiss functions from the injector into the LH. They can also be reconfigured to provide beam crossover upstream the LH chicane for emittance measurements in the *x* and *y* planes. The laser light will interact with electrons in the first undulator U1. The second undulator and the small chicane CH are devised for diagnostics employing the "optical replica" [Saldin *et al.* 2005] technique.

The laser heater lattice is also used to complete the matching of the Twiss functions from the injector into the accelerator.

For a calculation of the energy spread we use Eq.(9) of Ref. [Zholents *et al*. 2006] yielding the following estimate of the energy gain/loss experienced by an electron co-propagating along the undulator with the laser wave (focused in the center of the undulator):

$$\Delta\gamma(q,\nu,\hat{\sigma}_\tau) = 2\sqrt{\frac{A_L \alpha \hbar \omega_{0s}}{\left(mc^2\right)^2}\frac{K^2}{2+K^2}}\{JJ\} f(q,\nu,\hat{\sigma}_\tau)\,, \tag{4.1}$$

where

$$f(q,\nu,\hat{\sigma}_\tau) = \sqrt{\frac{2q}{(2\pi)^{1/2}\hat{\sigma}_\tau}}\int_{-0.5}^{0.5}\frac{\cos\left(2\pi\nu\hat{z} - \tan^{-1}(q\hat{z})\right)}{\sqrt{1+(q\hat{z})^2}}e^{-\hat{z}^2/4\hat{\sigma}_\tau^2}d\hat{z}\,. \tag{4.2}$$

The various quantities are defined as follows: γ is the relativistic factor, $A_L = P_L 2.35\sigma_\tau$ is the laser pulse energy and σ_τ is the rms width in intensity of the laser pulse with peak power P_L (a Gaussian shape is assumed), $q = L_w / z_0$, where L_w is the length of the

undulator with N periods, $z_0 = \pi w_0^2 / \lambda$ is the Rayleigh length, λ is the laser wavelength, w_0 is the waist size which is assumed to be in the center of the undulator, $\hat{\sigma}_\tau = \sigma_\tau / \tau_0$ where $\tau_0 = N\lambda / c$, c is the speed of light and $\omega_{0s} \approx 2\pi c / \lambda$ is the fundamental frequency of the electron spontaneous emission in the undulator, $\alpha = 1/137$ is the fine structure constant, $\hbar$ is the Plank constant, and $\nu = 2N\delta\gamma / \gamma_r$ where $\gamma_r^2 = \frac{\lambda_u}{2\lambda}\left(1 + K^2/2\right)$ is the so called FEL resonance energy, λ_u is the undulator period, $K = eB_0\lambda_u / 2\pi mc$, B_0 is the undulator peak magnetic field, e, m are the electron charge and mass, and $\hat{z} = z / L_w$, z is the coordinate along the undulator with the beginning in the middle of the undulator, $\{JJ\} = J_0(\xi/2) - J_1(\xi/2)$ and $\xi = K^2/(2+K^2)$. Eq. (4.1) defines the maximum amplitude of the energy modulation and according to Ref. [Spampinati *et al.* 2007] the rms energy spread induced due to the laser electron beam interaction is equal to half of that amplitude.

On the basis of these formulas we can now give a sense of the numerical value of the basic quantities characterizing the laser heater performance. For this purpose we assume that the laser heater is located after the first accelerating module where the electron beam energy is of the order of 140 MeV. (We alert the reader that in other parts of this Report we make the different assumption that the laser heater is located at 40MeV *i.e.* before the first accelerating module). We propose the use of a 800 nm laser wavelength (corresponding to a $\hbar\omega_{0s}$=1.5 eV photon energy) and a 3 cm undulator period. Based on these numbers we determine the undulator parameter to be *K*=2.45 (corresponding to a 0.9T peak magnetic field). Assuming β=19 m for the beta functions and ε=1 mm-mrad for the normalized emittance we calculate $\sigma_x = \sqrt{\beta\varepsilon/\gamma}$ = 263 μm. Matching of the laser beam and the electron beam size in the undulator center would require: $w_0 = 2\sigma_x$ and z_0 = 1.1 m. As in Ref. [Huang *et al.* 2004] we assume an undulator with 9 full periods, *i.e.* L_w = 27 cm.

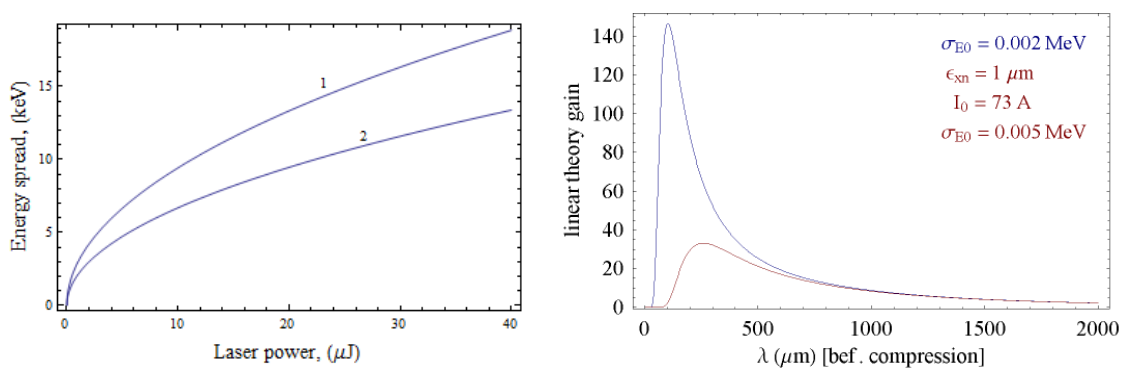

Figure 4.3: Picture to the left: the rms energy spread induced in the laser heater as a function of the laser pulse energy. Curve 1 is for a beta function β =19 m and curve 2 is for β =38 m. Picture to the right: the linear gain function for the microbunching instability for a beam with a small rms uncorrelated energy spread (2 keV, blue curve) can be greatly reduced by increasing the energy spread using the laser heater (red curve, corresponding to a 5 keV energy spread).

The rms energy spread induced by the laser heater as a function of the laser pulse energy for a Gaussian laser pulse with 40 ps FWHM is plotted in Fig. 4.3 (left picture, curve 1). For comparison we also report the corresponding quantity for an electron beam with larger transverse size, specifically, with beta function β =38 m (curve 2).

A demonstration of the effect of the laser heater is shown in the right picture of Fig. 4.3 where we report the gain function of the microbunching instability through Linac L1 and the bunch compressor (here we used a lattice with the laser heater located at 40 MeV, before L1; for the purpose of this calculation the exact location is irrelevantl as long as the relative energy spread remains unchanged). Observe that the larger the energy spread at the exit of the laser heater the weaker the gain at the high-frequency end of the spectrum. A further discussion of the implications of controlling the energy spread by the laser heater is contained in Sec. 6.

4.2 Bunch compressor

A schematic of the bunch compressor is shown in Fig. 4.4. It consists of a chicane built from four rectangular bending magnets. Due to symmetry, this bunch compressor is a perfect achromat. To compensate for the possibility of leakage of dispersion after the last bend due to errors trim quadrupoles (shown in Fig. 4.3 between the first and second bends and between the third and fourth bends) are added for a fine tuning of the lattice functions. Dispersion is at its maximum in the middle of the chicane and, therefore, this is a convenient place for a collimator and energy monitor. Here we plan to use two kind of diagnostic devices, *i.e.* BPMs and screens. Since the electron beam typically presents a significant energy chirp while propagating through the chicane, the collimator can be used to trim electrons from the head and tail of the bunch, thus providing a way to shape the bunch profile and reduce the undesired current spikes that often appear at the bunch edges. Alternatively, the same collimation function could be implemented in a dedicated non-dispersive module using rf deflecting cavities (see Sec. 4.4). This latter solution may be preferable as it offers more flexibility for a collimator design if it is designed to intercept electrons at much lower energy.

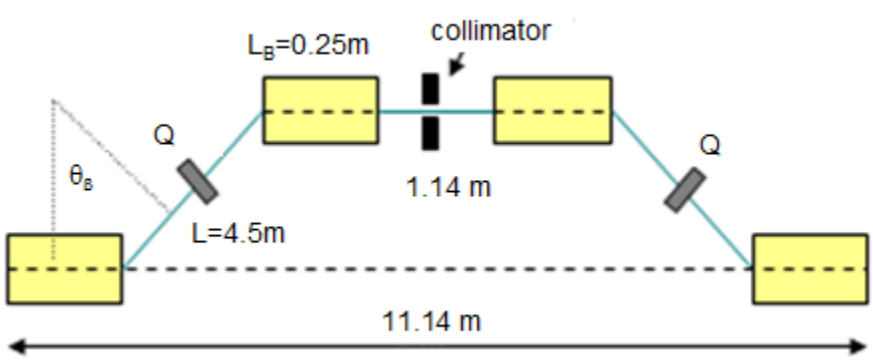

Figure 4.4: A schematic of the bunch compressor (not to scale).

An important consideration for a design of the bunch compressor is CSR. CSR plays a role in the microbunching instability discussed in Section 2.2.5 and may also be

responsible for emittance degradation. Both these processes can be moderated with the appropriate design of the compressor lattice.

Although transverse microbunching radiative effects [Derbenev *et al*. 1996] can affect emittance directly, this is usually a small effect and emittance degradation via longitudinal-to-transverse coupling is typically dominant. This coupling is characterized by the dispersion invariant:

$$\mathcal{H} = \left(\frac{1+\alpha_x^2}{\beta_x}\right) D_x^2 + 2\alpha_x D_x D_x' + \beta_x D_x'^2, \tag{4.3}$$

where α_x, β_x are horizontal Twiss functions and D_x, D_x' are horizontal dispersion function and its derivative. Here we assume a chicane lying in the horizontal plane. Using H, we write for the emittance change due to a CSR-induced energy variation:

$$\delta\varepsilon_x \approx \mathcal{H}(\delta E / E)^2 . \tag{4.4}$$

Here, $\delta E / E$ is the spread of the energy losses caused by CSR, which is proportional to the quantity defined in (2.24). It is obvious from Eq. (4.4) that a lattice with small $\mathcal{H}$ will generate a smaller emittance change. Since the strongest CSR effect is expected in the 4th bending magnet of the chicane where the electron bunch is the shortest, an optimization strategy that we can pursue is to reduce $\mathcal{H}$ in this magnet. A lattice implementing this strategy with a minimal Twiss function β_x in the last bend is shown in Fig. 4.5.

Next, we would like to present an argument showing why we may not want to get the smallest possible $\mathcal{H}$. While traveling through the chicane bend magnets, electrons with different betatron oscillation amplitudes follow different paths with path lengths described by the following equation:

$$\delta\ell(z) = \int_0^z \frac{x(z')}{R} dz' = x_0 \int_0^z \frac{C(z')}{R} dz' + x_0' \int_0^z \frac{S(z')}{R} dz' . \tag{4.5}$$

Here x_0, x_0' are the electron coordinate and angle at the beginning of the chicane and $C(z)$, $S(z)$ are cos-like and sin-like trajectory functions. It can be shown [Venturini *et al.* 2007a] that the rms value of $\delta\ell$ taken over the electrons in the any given slice of the electron bunch is related to the electron beam emittance through the function $\mathcal{H}$, *i.e.*:

$$\delta\ell_{rms} \approx \sqrt{\mathcal{H}\varepsilon_x} , \tag{4.6}$$

where ε_x is the rms value of the electron beam horizontal geometrical emittance. Thus, a lattice with large $\mathcal{H}$ "washes out" the microbunching more effectively than the lattice with the small $\mathcal{H}$ because it spreads apart slice electrons more than the lattice with the small $\mathcal{H}$, similarly to the Landau damping induced by uncorrelated energy spread. The smearing of the microbunching by a finite transverse emittance may be important and further analysis shows that without accounting for this effect the instability could be significantly overestimated.

On the basis of these considerations we design the BC lattice in such a way that the magnitude of $\mathcal{H}$ in the last bend of the chicane can be tuned by up to a factor of four.

This will give us some flexibility to maneuver between the tasks of containing the emittance excitation due to CSR, which benefits from a smaller $\mathcal{H}$, and that of containing the energy spread growth due to the microbunching instability, which benefits from a larger $\mathcal{H}$.

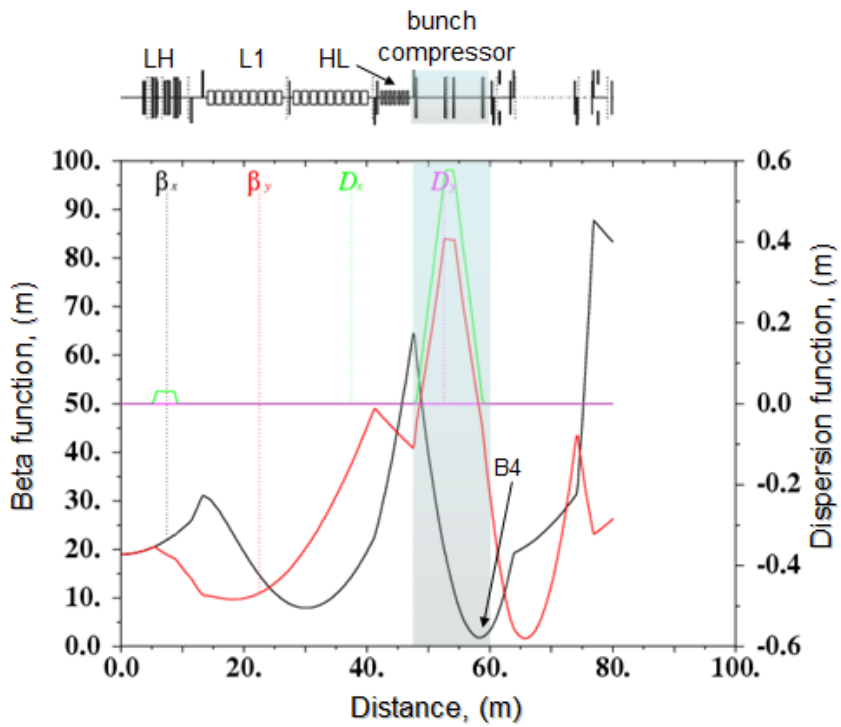

Figure 4.5: Twiss functions in the bunch compressor (highlighted) and in the adjacent linacs. The location of the 4th bending magnet is indicated by the arrow.

Four quadrupole magnets after the chicane are used for matching the Twiss functions into the downstream Linac 2. Between these magnets we reserved some space for a deflecting cavity to be used for emittance measurements and for the option of bending the beam into a side diagnostic beamline (yet to be designed).

Many accelerator designs for FEL facilities proposed so far employ two bunch compressors (*e.g.* [Arthur *et al.*]). While optimizing our design we also investigated this option and concluded that a second bunch compressor would greatly increase the gain of the microbunching instability. This would result into a considerably larger final energy spread after compression (see Fig. 4.6), even for an optimally tuned LH. On the other hand if the strong beam compression needed in a single-chicane BC lattice is carried out at relatively low electron beam energy an excessively large projected emittance growth can ensue because of CSR. Hence our choice of locating the BC at approximately 250 MeV beam energy. In the design of the BC we also optimized the Twiss functions to minimize the impact of CSR on the emittance as mentioned above. Results from macroparticle simulations that we will discuss in Sec. 6 show some growth in the projected emittance. While this will not compromise lasing it may interfere with some of the diagnostics. A more accurate assessment of the maximum tolerable projected

emittance growth is left for future work. If needed, higher quality emittance could be achieved by moving the BC further to higher beam energy.

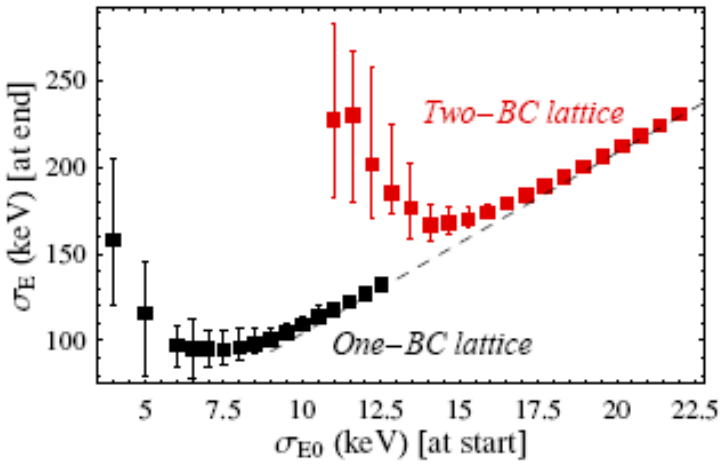

Figure 4.6: The rms electron beam energy spread at the end of the linac as a function of the electron beam energy spread immediately after the laser heater. This example is derived form the comparative studies of two accelerator configurations for FERMI@elettra FEL project [Bocchetta et al., Di Mitri]. The calculations were carried out using a Vlasov solver (see Appendix B).

4.3 Electron beam switch yard (spreader)

The electron beam switch yard also referred here as a "spreader" distributes the electron beam into ten independent FEL undulator lines, each operating at a repetition rate of 100 kHz. In the current design we follow a modular approach and build all spreader beam lines as uniformly as possible. We also adopted a design concept discussed in Ref. [Venturini *et al.* 2008] to minimize the impact of the spreader on the electron beam dynamics.

4.3.1 Design description

Fig. 4.7 shows the lattice functions from the beginning of the spreader to the end of the longest of the ten spreader beam lines. The remaining nine spreader beam lines branch off from the long FODO section seen in Fig. 4.7 starting from s=0. A schematic of the beam take-off sections, identical for all the ten beam lines, are shown in Fig. 4.8. The take-off sections are repeated after every second focusing quadrupole (two such sections are seen in the picture).

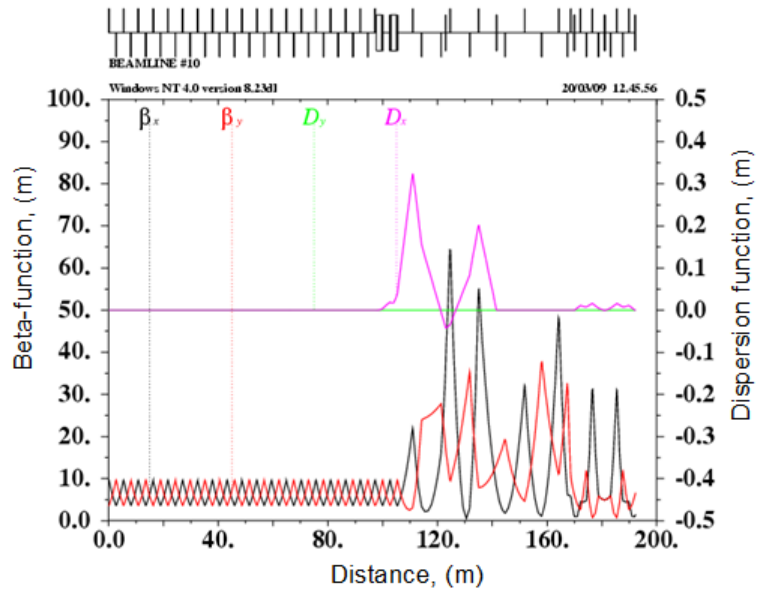

Figure 4.7: The lattice functions in the spreader.

A two meter long stripline kicker is located between focusing (F) and defocusing (D) quadrupoles. It supplies a 3 mrad kick to the electron bunch. The stripline has a small gap of 8 mm to maximize the field with assumed ±10 kV voltage on the electrodes. A pulsed power-supply with repetition rate up to 100 kHz, pulse amplitude up to 15 kV, and pulse length up to 10 ns is available from FID GmbH [Efanov]. The advertised timing jitter is less than 200 ps and the amplitude stability is 0.1%. The company stated that they can not measure stability better than 0.1% and expressed interest to work together to improve amplitude stability using beam-based measurement techniques.

The downstream defocusing quadrupole adds an additional 0.7 mrad to the primary kick. Then the orbit passes through the focusing quadrupole with a 15.8 mm off-set from the quadrupole center. This quadrupole forces the beam to go almost parallel to the FODO beam line. Next to this quadrupole is a septum magnet. The betatron phase advance between the kicker and the septum is 0.3π. This provision helps to maximize the orbit off-set at the beginning of the septum. The blown-up area in Fig. 4.8 shows a 15.6 mm distance between the axis of the FODO beamline and the beam orbit at the beginning of the septum and a 5.3 mm distance from the axis of the FODO beamline to the current wall of the septum magnet. The defocusing quadrupole of the FODO beamline downstream of the septum is a large bore quadrupole that is centered on the FODO line and the branch line has a 50 mm off-set there. This quadrupole supplies additional 17 mrad kick to the beam orbit. Beyond this quadrupole, the two beam lines continue in separated vacuum chambers. The next downstream focusing quadrupole along the FODO beamline is a small bore septum quadrupole: the line branching off passes by this quadrupole at a 150 mm distance from the axis of the FODO beam line.

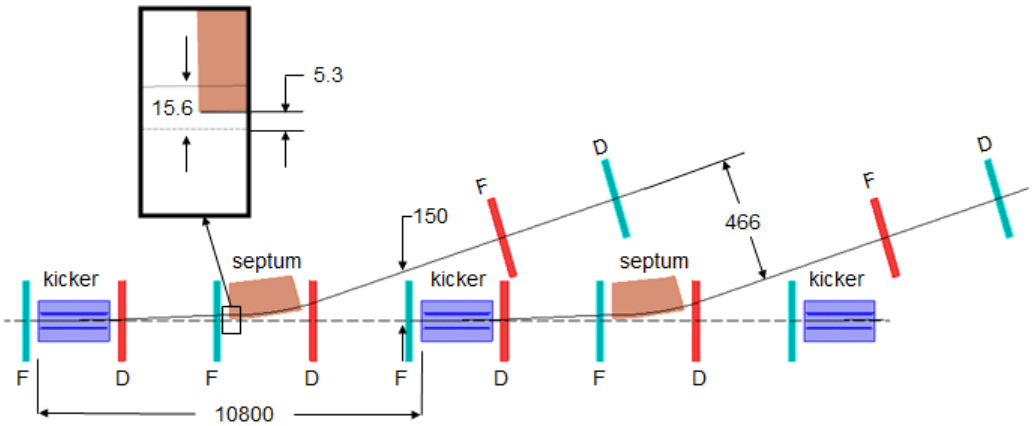

Figure 4.8: The schematic of the electron beam take-off section. All dimensions are given in mm. Scales are different in the vertical and horizontal direction.

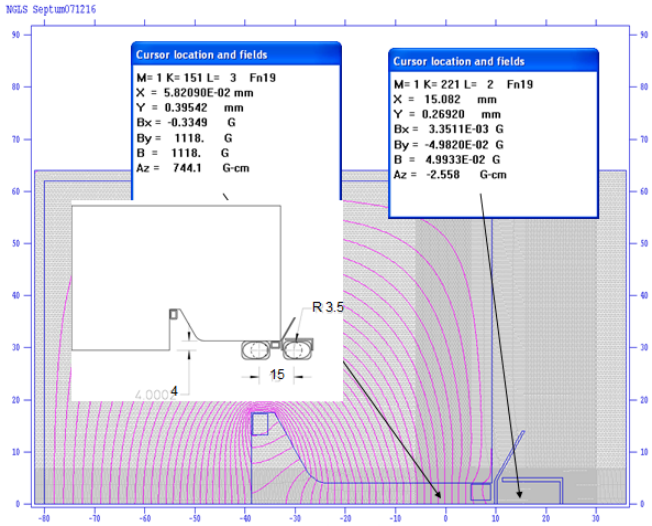

Figure 4.9: The cross section of the septum magnet. All dimensions are given in mm. See text for further detail.

Fig. 4.9 shows the cross section of the septum magnet and magnetic flux lines. The septum magnet is a C-type magnet with a 8 mm gap and current wall on the right side. The conductor is a hollow 4 mm × 3 mm rectangular tube with rounded corners and 3 mm × 2 mm rectangular bore. The current density is 55 A/mm^2. The insert shows important dimensions and also the magnitude of the magnetic field in the two locations indicated by the arrows, *i.e.* one on the electron beam orbit inside the magnet and the other on the FODO beamline behind the current wall. One can see that it is practically zero there. It is also assumed that a thin magnetic shield will be wrapped around the vacuum chamber in this location.

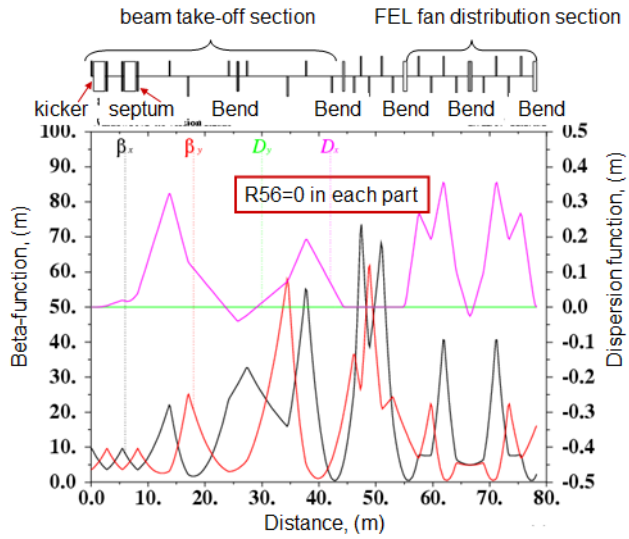

Figure 4.10: Lattice function for one of the spreader branch-off lines.

Fig. 4.10 shows the lattice functions of a typical branch beam line. The lattice has two distinct parts, *i.e.* the beam take-off section and the FEL fan distribution section. Each part is built as a triple-bend achromat. In the beam take-off section the kicker, septum and off-set quadrupoles are functionally equivalent to one bending magnet. An additional pair of bending magnets completes the achromat supplying 60 mrad orbit angle. Importantly, these achromats are designed to be isochronous with the design sufficiently flexible to allow for adjustment of the transfer matrix element R_{56} controlling the particle time-off-flight. The achromats are connected by a short matching section. As mentioned above, the beam take-off section is identical for all the FEL lines, while the FEL fan distribution section is different for each undulator beamline with gradually increasing orbit bending angle from 10 mrad to 140 mrad.

An electromagnet can be placed atop the stripline kicker and this will allow for a single FEL operation with maximum bunch repetition rate of 1 MHz.

4.3.2 Spreader beam dynamic studies

In order to verify the design concept we performed beam dynamics studies through the spreader. We are mainly concerned about the possible impact of the spreader bending magnets on the electron beam emittance and microbunching. For this study we selected the branch line that has the strongest bending magnets, thus focusing on the most demanding case. The proper location to begin our analysis is immediately downstream the bunch compressor. This is because some of the effects that we are interested are in fact seeded before the beam passes through the bending magnets of the spreader. In particular, of some concern is the energy modulation generated by the longitudinal space charge in the long linac section between bunch compressor and spreader. An energy modulation can be turned into an unacceptably large charge density modulation (microbunching) in the spreader region where R_{56} is non vanishing. Enforcing isochronicity as much as possible is a way to reduce the effect. The plot in Fig. 4.11 shows the gain of the microbunching instability calculated using the linear theory of Ref.

[Heifets *et al*.]. The amplitude of a sinusoidal density perturbation of wavelength λ present in the beam at the exit of the bunch compressor is amplified by a factor equal to the gain by the time the beam exits the spreader. The left plot shows that the gain is small when each achromat is isochronous. The gain is much larger on the right plot, *i.e.* in the case where we intentionally destroyed the isochronicity of the individual achromats while at the same time still preserving the overall isochronicity for the entire spreader beamline (this was achieved by having the two achromats mutually compensating for the time of flight.). We also found that the gain is substantially larger when the entire beamline is not isochronous.

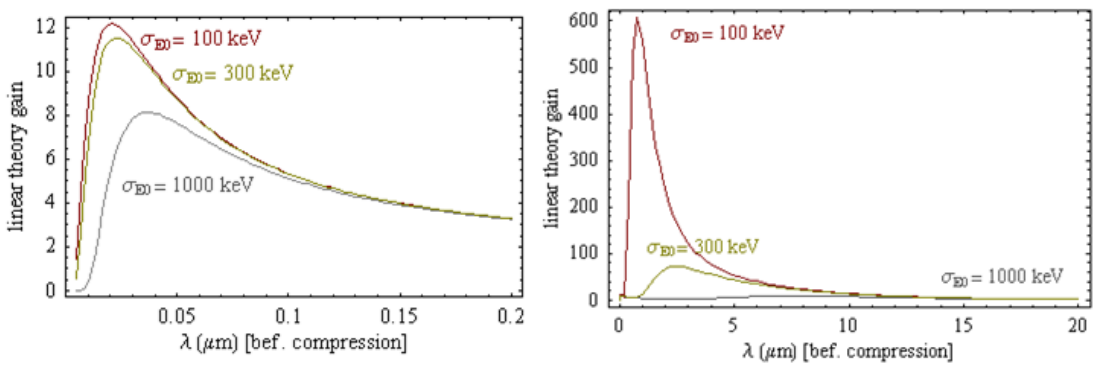

Figure 4.11: The linear gain of microbunching instability beginning from the exit of the bunch compressor through one of the spreader lines. The assumed uncorrelated beam energy spread is indicated on the graphs. The left plot is for a case when both achromats are insochronous and the right plot is for the case where the entire spreader is isochronous but the individual achromats are not.

Following these studies we performed particle tracking of the same part of the machine for a nominal case using the code IMPACT with one billion macroparticles and obtained the electron beam distribution in the longitudinal phase space shown in Fig. 4.12. In good agreement with linear theory this plot demonstrates a weak microbunching. We should emphasize that we have not yet studied the non-isochronous spreaders with high-statistics macroparticle simulations. While we believe that a non-isochronous spreader should be avoided, the magnitude of the adverse effects may have to be revised from estimations based on the linear theory and a simplified 1D model of longitudinal space charge impedance, which has known limitations.

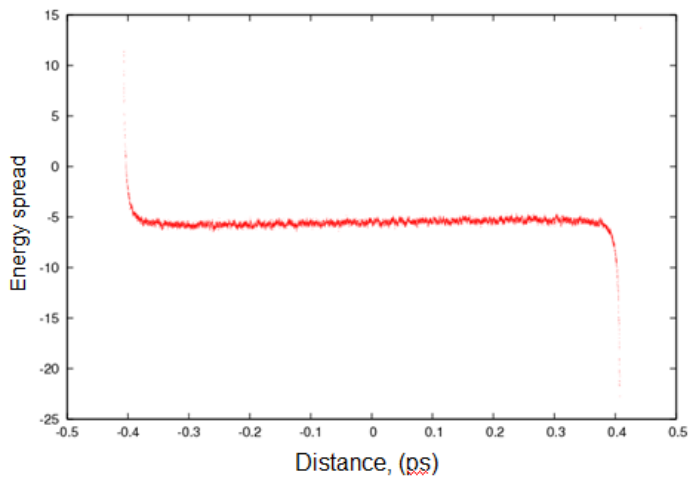

Figure 4.12: The electron bunch distribution in the longitudinal phase space. The energy deviation is in units of the electron rest mass.

Fig. 4.13 shows the plot of the slice emittance along the bunch obtained from IMPACT simulations through the spreader. The emittance at the exit of the linac (green curve) is contrasted to the the slice emittance of the beam at the exit of the BC (start of simulation). Clearly no emittance growth is observed aside from the bunch tails.

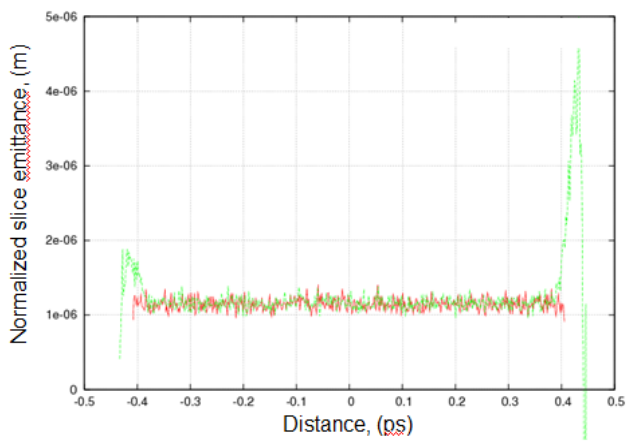

Figure 4.13. Slice emittance along the electron bunch at exit of the BC (red curve, start of simulations) and exit of the spreader (green curve).

4.4 An active "management" system for bunch tails

Macroparticle simulations show that intense beams traveling through the injector and the linac have a propensity to filament in the longitudinal phase space. Filamentation results from a combination of collective effects and rf nonlinearities causing particles populating forward and backward beam tails to gain (or lose) energy compared to the beam core. As the beam traverses dispersive regions these particles will shift longitudinally relative to the beam compounding the overall degradation of phase-space quality.

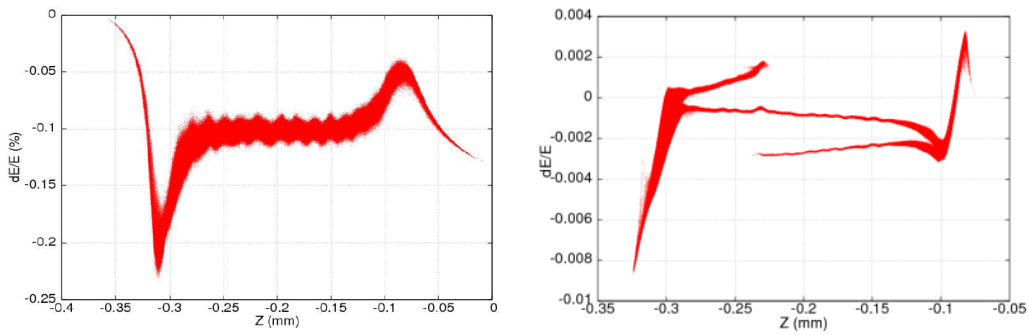

Figure 4.14:. Examples of longitudinal phase space at the exit of one of the linacs considered in our studies for x-ray FELs. A 0.8nC bunch with an initial Gaussian charge density in the longitudinal direction (picture to the right) is shown to develop branch-like structures that are markedly absent when a beam with a more compact profile (parabolic) is used (picture to the left). Notice the difference in the vertical scales.

Generally, the details of this evolution and the final phase-space footprint will depend on the initial profile of the longitudinal beam density. A beam presenting an initial longitudinal density with long tails will be more prone to filament than a beam with a more compact profile. This is exemplified in Fig. 4.14 where the phase space at the exit of a linac starting from a beam with a parabolic longitudinal density (picture to the left) is compared to that resulting from a beam with initial Gaussian density (picture to the right).

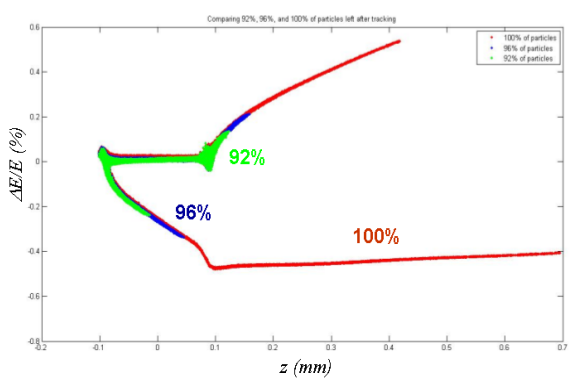

Figure 4.15: Another example of beam longitudinal phase space at the exit of a linac. The initial beam distribution in this example was obtained from a numerical simulation of the injector. The bifurcations observed in the right picture of Fig. 4.14 are absent but very long tails can still be noticed. Fortunately, as indicated in the figure, these tails tend to be thinly populated.

Although relatively few electrons will in general populate the filamented regions of phase space (Fig. 4.15) their presence may be a nuisance. Firstly, there is a concern that particles in these regions may not be intercepted by ordinary collimators placed along the machine and thus get lost in an uncontrolled manner possibly causing damage to sensitive devices (in particular the FEL undulators). Secondly, portions of the beams with the same

longitudinal coordinate but slightly different energy may degrade lasing in the FEL. Thirdly, a filamented beam phase space could make the reading of certain diagnostic signals difficult to interpret.

As suggested by Fig. 4.14 containment of the phase-space at the exit of the linac could be achieved, at least in principle, by suitable control of the beam tails through the injector. This is a strategy worth investigating but it remains to be demonstrated that one can design and injector system allowing for this functionality while at the same time meeting other requirements on bunch population, transverse emittance, and length. Instead, to prevent the potential harm deriving from the uncontrolled evolution of the beam tails once can conceive of ways to intervene along the machine to shape the longitudinal beam density directly.

A possible system implementing this capability consists of a pair of rf deflecting cavities and a collimator. The first cavity will induce a longitudinal-transverse correlation (say in the vertical direction) by applying a z-dependent linear kick along the bunch. The correlation will develop as the electrons undergo betatron motion. At a suitable point downstream the cavity where the *y/z* correlation in the beam density is fully developed a collimator will remove particles with large transverse offset and thus deplete the particle population in the longitudinal tails. A second deflecting rf cavity downstream would then remove the transverse/longitudinal correlation before the beam resumes its trajectory down the linac. A schematic for the device is shown in Fig. 4.16.

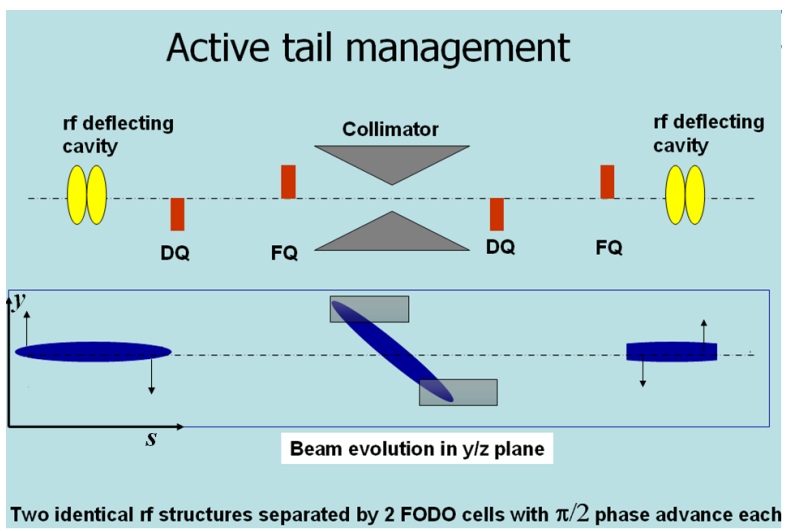

Figure 4.16: Concept for an rf deflecting -cavity based collimator for removing tails from the beam longitudinal profile. The beam travels from left to right.

The required kick can be realized using an rf structure operating in the TM_{110} mode [Zholents *et al.* 1999, Emma 2000]. A particle with longitudinal coordinate *z* (*z* measure the longitudinal position with respect to the reference particle in the bunch) will receive a transverse kick of magnitude

$$\Delta y' = \frac{eV_0}{E}\sin(-k_{rf}z + \phi) \approx \kappa_z z\,,$$

where the second equality follows from a linear expansion and the assumption $\phi=0$. Here $\kappa_z = -2\pi e V_0/(E\lambda_{rf})$, V_0 is the cavity transverse voltage, λ_{rf} the rf cavity wavelength and E the beam energy. Notice that in this section $z>0$ denotes a particle in the bunch head. In the reduced phase-space with particle coordinate $\vec{x} = (y, y', z)$ we write the transfer matrices for propagation of the beam between the two rf cavities and for the action by each cavity as

$$M = \begin{pmatrix} m_{yy} & m_{yy'} & 0 \\ m_{y'y} & m_{y'y'} & 0 \\ 0 & 0 & 1 \end{pmatrix} \quad \text{and} \quad M_{rf}(\kappa_{rf}) = \begin{pmatrix} 1 & 0 & 0 \\ 0 & 1 & \kappa_z \\ 0 & 0 & 1 \end{pmatrix},$$

having assumed that the electrons are ultrarelativistic so that motion in z is effectively negligible. The condition for the y/z correlation to be removed from the beam by the exit of the second cavity requires that the entries (1,3) and (2,3) of the matrix product $M_{rf}(\kappa_z^{(2)}) M\, M_{rf}(\kappa_z^{(1)})$ vanish *i.e.* $m_{yy'}\kappa_z^{(1)} = 0$, and $m_{y'y'}\kappa_z^{(1)} + \kappa_z^{(2)} = 0$, where $\kappa_z^{(1)}$ and $\kappa_z^{(2)}$ are relative to the leading and trailing cavity respectively. These two conditions are satisfied, in particular, by choosing the transverse part of the transfer matrix M to satisfy $M_\perp = -1$, (*i.e.* $m_{yy'} = m_{y'y} = 0$, $m_{yy} = m_{y'y'} = -1$), and $\kappa_z^{(1)} = \kappa_z^{(2)}$.

In the considerations to follow we assume negligible vertical beam size, which is a good approximation as long as the anticipated transverse particle offset in the collimator is large compared to the transverse beam size (typically sub-mm). Consider an electron located in the head of the beam $z = l_b$. Denoting with N the transfer matrix for the vertical betatron motion from the first rf structure up to the collimator, the vertical offset displayed by the electron is given by $y = N_{12}\kappa_z^{(1)} l_b$. Using the standard parameterization [Lee] for the entry N_{12} in terms of beta functions $\beta_y^{(1)}$ and $\beta_y^{(c)}$ (at the rf structure and collimator respectively), and phase advance $\Delta\psi$, we have $N_{12} = \sqrt{\beta_y^{(1)}\beta_y^{(c)}}\sin(\Delta\psi)$ and therefore

$$y = \beta_y^{(c)} \frac{2\pi e V_0}{E\lambda_{rf}} l_b \,, \tag{4.7}$$

on the further assumption that $\beta_y^{(1)} = \beta_y^{(c)}$ and $\Delta\psi = \pi/2$. This choice for the phase advance maximizes the vertical offset obtainable for a given transverse while at the same time insuring that the transverse part of the transfer matrix satisfies the condition $M_\perp = -1$ for removal of longitudinal/transverse correlations. We base the numerical examples to follow on the lattice shown in Fig. 4.17 consisting of two 5.5 m FODO cells. The beta functions at the location of the collimator and rf structures are $\beta_y = 4.2$ m

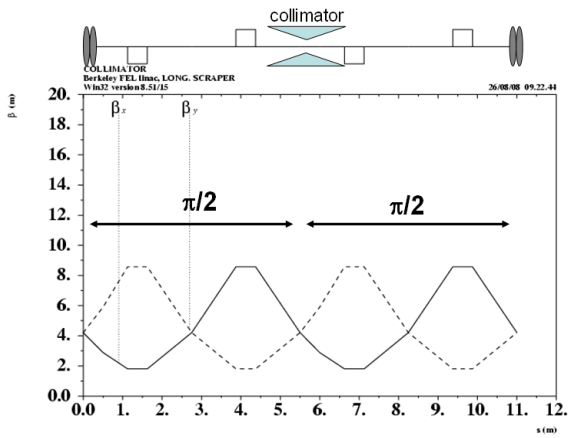

Figure 4.17. Lattice functions for an 11m long two FODO-cell beamline with collimator. (The dimensions of the collimator and the rf deflecting cavities are not to scale.)

The rf deflecting cavities are located at the two ends of the beam line. In the present calculation for the purpose of determining the Twiss functions they are treated as drifts. Because of the requirements posed by the machine high repetition rate (1 MHz) superconducting technology is the obvious choice. As suitable models for our discussion we consider the superconducting 3.9 GHz structures discussed in [Li D.]. Assuming a 50 MeV beam energy, to scrape particles from the beam tails $z>|l_b|$ with l_b=1.5 mm using a collimator with $2y_c$=2 cm aperture will require about V_0 ~ 1 MV. With a modest deflecting gradient of about 5 MV/m the required voltage magnitude can be obtained using the ~0.5 m long structure investigated in [Li D.].

Power density deposition on the collimator is an important quantity to investigate in order to determine the practical feasibility of a longitudinal scraper design. Here we present a simple model aimed at finding an order-of-magnitude estimate and basic scaling with respect to some relevant parameters. We model the collimator cross section as consisting of two triangular shapes in the *y/s* plane as shown in Fig. 4.16. The two basic parameters determining this geometry is the angle α between the slanted sides of the collimators and the *z* axis and the minimum vertical aperture $2y_c$ (the collimator is assumed to be translational invariant in *x*). Denote with *dN(s)* the number of particles deposited on the collimator wall along a segment of length *ds*. We are interested in finding the power deposited per unit length along the collimator wall surface

$$P = E\nu \cos^{-1}(\alpha)\frac{dN}{ds}, \tag{4.8}$$

where ν is the bunch repetition rate. Suppose that the electron bunches have a longitudinal particle density $N_b f(z)$ where N_b is the bunch population and $f(z)$ is normalized to unity. To find $\frac{dN}{ds_z} = N_b f(z(s_z))\frac{dz}{ds_z}$ we shall need to determine the relationship $z = z(s_z)$ between s_z and the longitudinal phase-space coordinate *z* of an electron scraping the collimator surface. Notice that we distinguish between the position along the beamline of an electron with *z*-coordinate $s_z = s + z$ and *s*, the location along the beamline of the reference particle in the bunch (defined as having phase-space coordinate *z=0*).

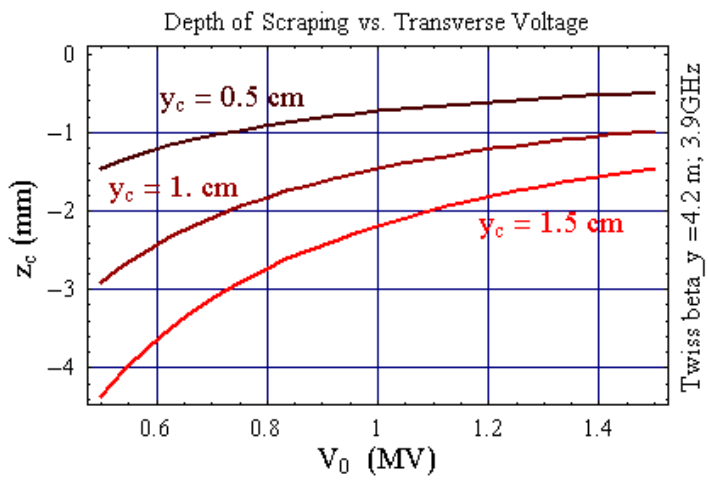

Figure 4.18: Scraping depth z_c for the tail of the longitudinal beam density (z<0) as a function of the rf deflecting cavity transverse voltage V_0 for various choices of the scraper vertical aperture. Particles with coordinate $z<z_c$ are scraped off. A similar picture holds for particles in the beam head (z>0).

Denote with $Y(z;s)$ the transfer function yielding the vertical coordinate at s of an electron that has vanishing transverse offset and coordinate z at the beginning of the beamline and denote with $Y_{scrap}(s)$ the function yielding the profile of the scraper cross-section in the *y/s* plane (more precisely we have 2 such piece-wise linear functions for the top and bottom parts of the collimator). For sake of concreteness let $Y_{scrap}(s)$ describe the top part of the collimator. Also, assume that the beam is tilted as shown in Fig. 4.16 with the tail (head) pointing upward (downward). The desired relationship $z(s_z)$ is defined as an implicit function by the equations $Y_{scrap}(s+z) = Y(z;s)$ and $s_z = s+z$. If we define R to be the transfer matrix for the vertical betatron motion from the beginning of the beamline through the focusing quadrupole (FQ) immediately before the collimator an approximate solution to the above equation reads:

$$z \approx -\frac{y_c + (s_c - s_z)\tan\alpha}{|\kappa_z|[R_{12} + (s_z - s_{FQ})R_{22}]}, \tag{4.9}$$

where s_c is the location of the collimator center along the beamline. The above expression is accurate provided that zR_{22}/R_{11} be small (for bunch lengths of the order of a few mm or less and a FODO cell a few meters long this is always the case). The above expression also yields an expression for the depth of scraping, upon setting $s_z=s_c$ $z_c = -\frac{y_c}{|\kappa_z|[R_{12} + (s_c - s_{FQ})R_{22}]}$; (the particles in the beam tail scraped off by the collimator are those with longitudinal coordinate $z < z_c$). Numerical examples of scraping depth as function of the transverse voltage for various choices of the collimator vertical aperture are shown in Fig. 4.18.

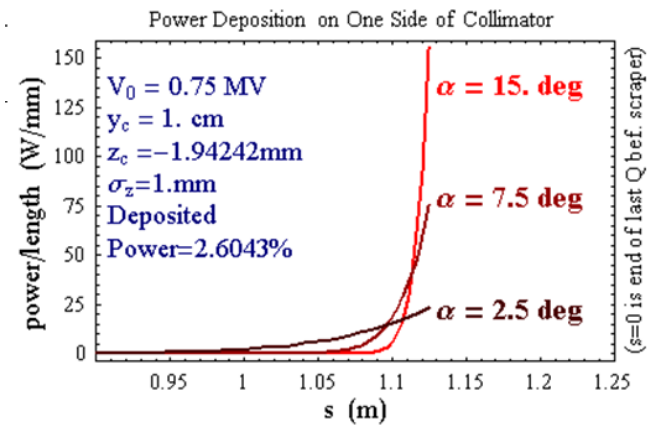

Figure 4.19: Power deposition along the top or bottom side of the collimator; the longitudinal position s is measured starting from the exit of the last quadrupole before the collimator. The center of the collimator is at s= s_c=1.125 m.

For a given longitudinal density profile, for example of Gaussian form, we can then use Eq. (4.9) into Eq. (4.8) to determine the power per unit length along the collimator deposited by the scraped electrons. Assuming 1 nC bunches at E=50 MeV, and 1 MHz repetition rate (corresponding to 50 kW total beam power), Fig. 4.19 shows that the peak power deposition per unit length (along either the top or bottom part of the collimator) is about 75 W/mm for an angle α=7.5° , corresponding to a particle loss of about 2.6%. Assuming a 1μm rms emittance beam implying a ~200 μm rms horizontal size the resulting peak power deposition per unit area is in the neighborhood of 300 W/mm^2. Removing the heat load from the collimator resulting from this power deposition may be challenging.

Another important consideration concerning the feasibility of a collimator system concerns the possible detrimental impact on the beam through wake fields. A first (rough) assessment of the magnitude of the effect can be carried out using simple analytical formulas applicable to shallow tapered collimators in the inductive-regime [Yokoya, Stupakov]. Although this regimes requires $\alpha y_c/\sigma_z << 1$ we can hope to still get a meaningful order-of –magnitude estimate in spite of the fact that for the short bunches of interest in our application and reasonable choices for α and y_c the above ratio tends to be close to unity. The transverse kick experienced by particles with coordinate z along a Gaussian beam and transverse offset y is given by $\Delta y' = y\frac{N_b r_e}{\gamma} Z_0 c \frac{\alpha}{y_c}\frac{\exp(-z^2/2\sigma_z^2)}{(2\pi)^{3/2}\sigma_z}$, where r_e is the electron classical radius, γ the relativistic factor, and Z_0 the vacuum impedance. For α=10°, σ_z=1 mm, and y_c=1 cm the peak value of the kick is of the order of 1 μrad if one assumes scraping particles with $|z|>2\sigma_z$ This should be compared to the rms angular spread of a beam with 1μm rms emittance, which is about 50 μrad (having assumed β_x=4 m for the horizontal beta function and a 50 MeV beam energy). Although seemingly benign these numbers warrant a more careful evaluation using either a more advanced analytical model or numerical simulations to completely rule out any adverse effects on the beam.

5. Long range wake fields and beam break-up instability

An ultra-relativistic charged particle bunch moving through a resonator cavity leaves behind a wake field that will affect subsequent bunches (if the bunch is not ultra-relativistic, the wake field will not be exclusively behind it). If the initial bunch enters the cavity off-axis, it will produce a transverse wake field that can then kick later bunches off the axis. Thus, even bunches that were initially traveling on-axis could be displaced and, in turn, produce their own transverse wake fields. The offsets obtained by bunches could increase along the bunch train, leading to the so-called multi-bunch beam break-up instability [Chao *et al.* 1980]. The purpose of our investigation is to see whether such instability will occur in the accelerator under the following conditions listed in Table 5.1.

Table 5.1: *Electron beam and linac parameters used in the beam break-up studies.*

Linac type	1.3 GHz, superconducting rf linac
Charge per bunch	0.8 nC
Bunch repetition rate	1 MHz
Beam energy entry/exit linac	0.240/2.180 GeV

When a charged bunch moves through a resonator cavity, it excites various higher-order modes (HOMs) in the cavity, which contribute to the total long-range wake. A quantity called the loss factor can be defined for each HOM; it is proportional to the amplitude of the oscillations of that HOM. Modes with higher loss factors have a greater wake field and a greater impact on the electron beam. One can usually ignore effects from HOMs with low loss factors (which HOMs can be ignored must be determined via simulation or experiment).

Our current working assumption is that the BFA will have the same accelerator modules as those proposed in the TESLA Design Report [Brinkman, *et al.*]. Because the modules are the same, the properties of the HOMs (amplitude, frequency, damping time, etc.) are also the same, since these depend only upon the properties of the cavity. Table 5.2 taken from [Baboi] shows which modes are expected to dominate the long-range transverse dipole wake field. We will consider only small deviations from the axis, and so the dipole wake is a good approximation for the total wake field.

5.1.1 Wake field of a single bunch

We can calculate the transverse wake field left behind a point-like bunch (the so-called delta wake) using a formula for the wake function from [Baboi]:

$$w_\perp(\hat{z}) = \sum_l 2k_{\perp l}\frac{c}{\omega_l}\sin(\omega_l\frac{\hat{z}}{c})\exp(-\frac{\omega_l}{2Q_l}\frac{\hat{z}}{c}) \quad \text{for } \hat{z} > 0 \qquad (5.1)$$

$$w_\perp(\hat{z}) = 0 \quad \text{for } \hat{z} < 0.$$

where k_l is the loss factor of the lth mode, Q_l is the quality factor of the lth mode, ω_l is the frequency of the lth mode. We sum over the HOMs listed in Table 5.2, since they are

considered to have the largest impact on the wake field. Defined this way, the wake function gives the transverse potential seen by a bunch, traveling over a unit length, while moving through a wake field produced by a bunch of unit charge that had an unit offset. The behavior of the dipole wake function (using dipole loss factors in the formula above) is illustrated in Fig. 5.1.

Table 5.2: *Dipole modes with the highest loss factors. The two independent polarization directions (x and y) have slightly different frequencies for the modes. In order to find the wake field in what we consider the x-direction, one needs to sum over the modes with the 1st polarization. Similarly, summing over the modes with the 2nd polarization will give the wake field in what we consider as the y-direction. Only data on the frequency, loss factor, and measured Q was used in this investigation*

Frequency (simulation) [GHz]	Ave. frequency (measured) [GHz]		Loss factor (simulation) [V/pC/m^2 /9-cell]	R/Q (simulation) [Ω/cm^2 /9-cell]	Q (meas.)	Q (BBU limit [11])
	1st pol.	2nd pol.				
TE_{111}-like						
1.6289	1.6110	1.6114	0.16	0.01	$1.0\cdot10^6$	
1.6369	1.6188	1.6195	2.67	0.10	$5.0\cdot10^5$	
1.6506	1.6321	1.6316	0.02	0.001	$2.0\cdot10^5$	
1.6669	1.6500	1.6506	19.98	0.76	$7.0\cdot10^4$ *	
1.6888	1.6725	1.6727	6.05	0.23	$5.0\cdot10^4$	
1.7137	1.6978	1.6991	301.86	11.21	$5.0\cdot10^4$ *	$8.4\cdot10^3$
1.7383	1.7260	1.7252	423.41	15.51	$2.0\cdot10^4$ *	$7.2\cdot10^3$
1.7652	1.7554	1.7545	59.86	2.16	$2.0\cdot10^4$ *	
1.7909	1.7827	1.7831	49.20	1.75	$7.5\cdot10^3$ *	$7.2\cdot10^3$
TM_{110}-like						
1.7991	1.7949	1.7948	21.70	0.77	$1.0\cdot10^4$ *	
1.8392	1.8342	1.8334	13.28	0.46	$5.0\cdot10^4$ *	$4.7\cdot10^4$
1.8531	1.8509	1.8511	11.26	0.39	$2.5\cdot10^4$ *	$5.2\cdot10^4$
1.8647	1.8643	1.8635	191.56	6.54	$5.0\cdot10^4$ *	$7.6\cdot10^4$
1.8727	1.8731	1.8732	255.71	8.69	$7.0\cdot10^4$ *	$1.2\cdot10^5$
1.8783	1.8795	1.8798	50.80	1.72	$1.0\cdot10^5$ *	$1.9\cdot10^5$
1.8820	1.8837	1.8841	3.17	0.11	$5.0\cdot10^5$	$3.3\cdot10^5$
1.8842	1.8864	1.8868	4.72	0.16	$7.0\cdot10^5$	$6.7\cdot10^5$
1.8852	1.8877	1.8881	2.31	0.01	$1.2\cdot10^6$	
TE-like						
2.5630	no statistics		42.41	1.05	$1.0\cdot10^5$ *	arbitr. chosen
2.5704			20.05	0.50	$1.0\cdot10^5$ *	
2.5751			961.28	23.80	$5.0\cdot10^4$ *	

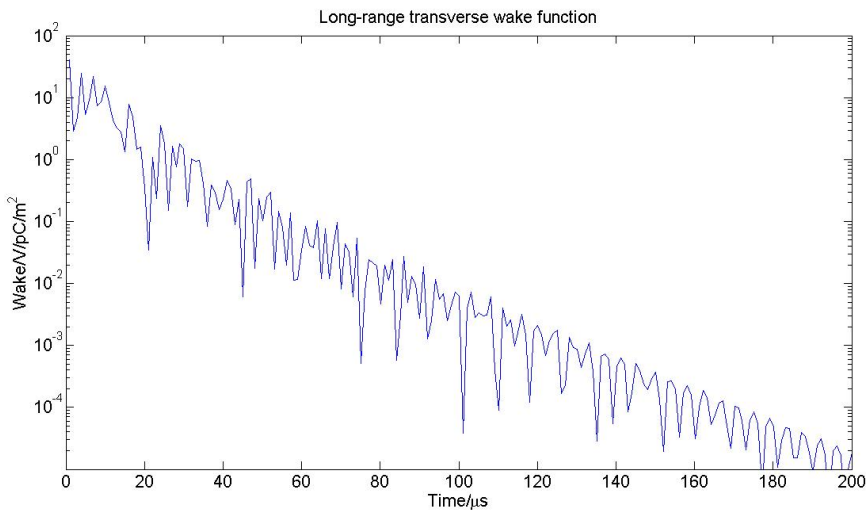

Figure 5.1: *Long-range transverse dipole wake function for a point-like bunch moving through a resonant cavity. The wake field for a point-like bunch (represented above) is known as a delta wake.*

5.2 Results of beam break-up studies

In the following analysis we are mostly concerned about stability of the machine operation at 1 MHz bunch repetition rate. However we should assume that a start up and initial commissioning of the machine will be performed at a lower repetition rate and beam-based alignment will be used to establish stable beam trajectory through the linac. Following terminology borrowed from storage rings we can refer to this as the "golden orbit". We assume that the values for dipole wake fields as reported in Table 5.2 can be applied also to small deviations from the golden orbit (in general different from the geometric axis of the accelerator)

In this section we investigate the consequences of one or several bunches deviating from the golden orbit due to some abnormal fluctuations. We are interested in establishing whether these fluctuations will propagate and grow over the trailing bunches causing a multi-bunch beam break-up or instead will die out in a short period with no consequences on beam stability [Kur].

5.2.1 Two-linac section model

We now start with a simplified model, which we use to demonstrate the general behavior of the beam when bunches move off-axis. We assume two adjacent linacs (with the HOMs listed in Table 5.2), each of length 30 m. We do not consider acceleration in this model, but rather assume that the beam has a constant energy of 0.7 GeV. A bunch (we will call the first bunch) enters the first linac with x-offset σ_x (the rms transverse beam size) and no angle, as shown in Fig. 5.2. The rest bunches will enter the first linac on-axis, also with no angle (Fig. 5.3). For the long-range transverse dipole wake field, a

bunch offset in the x-direction will leave behind a wake field that deflects only in the x-direction. We thus limit our observations to the x-direction, since we assume no deviations in the y-direction.

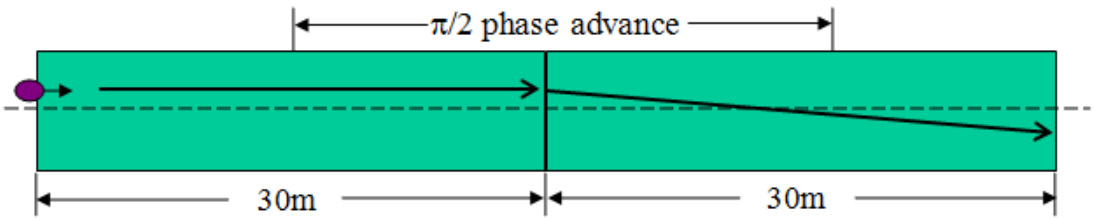

Figure 5.2. *Schematic of the two linac model showing the first bunch entering with an offset. The green rectangles represent the linacs and the purple oval is the bunch. This bunch proceeds with its normal betatron oscillation, and so has an angle but no offset in the middle of the second linac.*

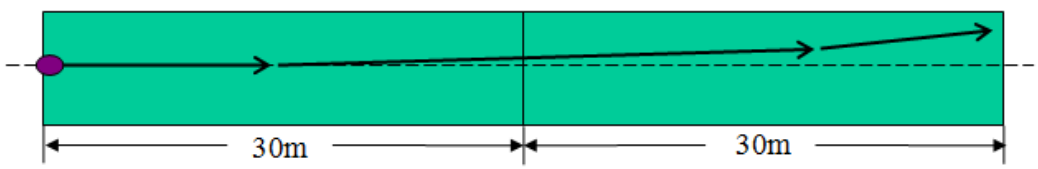

Figure 5.3. *Schematic of the two linac model showing a bunch entering the first linac (after the first bunch and any other previous bunches have already left a wake field). This bunch receives a transverse momentum kick in the middle of the first linac due to the transverse wake field, and then continues to the second linac where it experiences a transverse momentum kick from the existing wake field, and also makes its own contribution to the wake field in the second linac.*

After leaving behind a wake field, the first bunch will move to the second linac. In order to simplify the calculations, we assume a constant β_x=30 m in the two linacs, and a betatron phase advance of $\Delta\mu_x=\pi/2$ between their centers. This gives a simple transfer matrix between the first and second linac: $M=\begin{bmatrix} 0 & \beta_x \\ 1/\beta_x & 0 \end{bmatrix}$. Since the first bunch went through the first resonator with offset σ_x, it will go through the second linac with angle σ_x/β_x and no offset. Meanwhile, subsequent bunches will experience a transverse momentum kick in the first linac, knocking them off-axis. This causes them to obtain an angle in the first linac: $dx/ds=\Delta p_\perp/p_0$, where p_0 is the longitudinal momentum of the beam. $\Delta p_\perp$ can be defined with the help of the single-bunch wake as:

$$\Delta p_\perp(t)=\tfrac{1}{c}\int_{s_0}^{s_0+L}\int_0^\infty w_\perp(c(t-t'))q(t')x(t')dt'ds\,, \qquad (5.2)$$

where q is magnitude of the charge in the electron bunch at time t', $x(t')$ is the transverse displacement of a bunch at time t', s_0 is some distance along the linac, and L is the length of a structure (usually a resonant cavity). In general, the wake field could depend upon the distance along the linac (in case the properties of the cavities changes), but in our models, the integrand is independent of s, and so the double integral reduces to a single integral over t', multiplied by L.

The transverse momentum kick makes all bunches after the off-axis bunch have angles but not offsets in the first linac. Applying the transfer matrix, the offsets of the bunches in the second linac will be these angles multiplied by β_x. Since the bunches are no longer moving on-axis in the second linac, they will all leave behind wake fields that subsequent bunches will encounter. Thus all bunches after the first will have both an angle and an offset in the second linac.

From the definition of normalized emittance in the case where $\alpha_x=0$, $\varepsilon_x = x^2/\beta_x + \beta_x x'^2$ we can define an effective beam size (really the amplitude of betatron oscillations): $\sigma_{eff} = \sqrt{\varepsilon_x \beta_x} = \sqrt{x^2 + (\beta_x x')^2}$. We then define gain as σ_{eff}/σ_x, *i.e.* the amplitude of betatron oscillations gained by each individual bunch at the end of the linac normalized by the amplitude of betatron oscillations at the end of the linac obtained by the first bunch. The gains for bunches two onward are shown in Fig. 5.4. One can see that the effects of the wake fields are very small. The second bunch ends up with only about 4% of the deviation of the first bunch. Additionally, the amplitudes of oscillations decrease along the bunch train. This shows that the beam is stable when one bunch deviates from the established orbit.

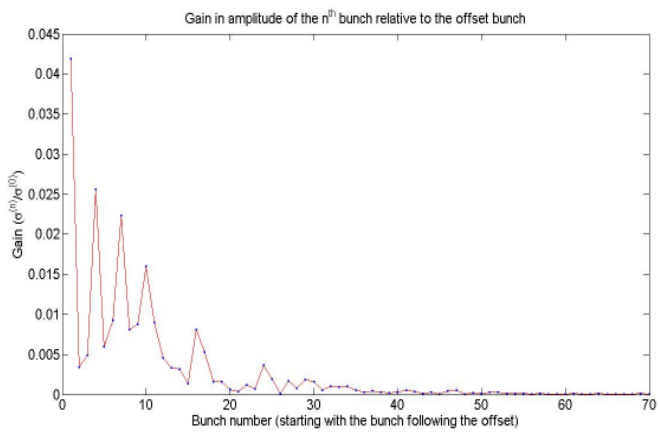

Figure 5.4 *Plotted is the amplitude of betatron oscillations of bunches at the end of the second linac (in the two linac model) normalized by the amplitude of betatron oscillations of the first bunch (σ_x). This plot shows how small the wake field effects are, since the second bunch is displaced from its path by only 4% of the displacement of the first bunch. The amplitudes of oscillations decrease along the bunch train, meaning that there is no beam break-up.*

We continued our investigation using the two linac model by simulating a situation in which the initial offset would be given by a sinusoidal function: $x = \sigma_x \sin(\omega_{jit} t)$. This could happen if some element before the first linac has a jitter which kicks the bunches

with some frequency ω_{jit}. We assume that such an element has a period that is long compared to the bunch spacing. The results for a modulation frequency of 10 kHz are shown in Fig. 5.5. Here one can see the bunches almost exactly following the pattern of the element causing the offset. This gives further evidence that the effect of the wake fields is small (the bunches which enter the first linac with an offset of σ_x end with an amplitude that is only slightly greater).

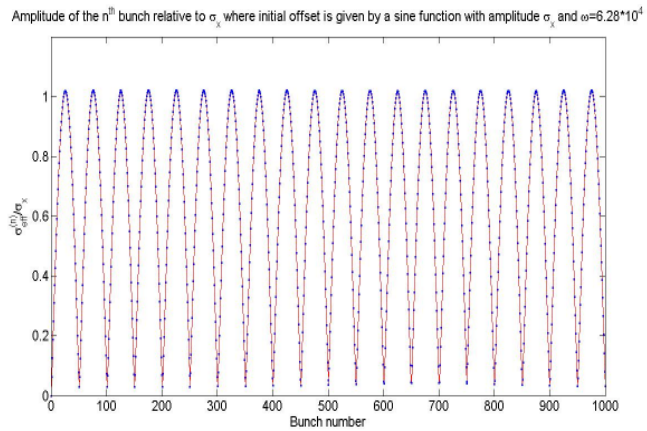

Figure 5.5. *A plot of how the bunch train responds to an element that causes bunches to have a sinusoidal variation in initial offsets. Due to the small wake field effects, the bunches end with an amplitude of oscillation only slightly greater than their initial offset. Thus having an element in the beamline which kicks the bunches off of their ideal path (with a period that is long compared to the bunch spacing) does not cause the beam to break up.*

5.2.2 Five-linac sections model

We now look at a more realistic model of the acceleration system in the BFA. We break up the linac into five units (resonators) accounting for energy gain along the linac and for variations in Twiss functions from unit to unit but considering constant Twiss functions along the unit. We look at the bunches starting at a point with a betatron phase $\pi/2$ less than the phase at the center of the first resonator. We assume that all of the bunches move on-axis through that point, but that one of them (the "first") has an angle of σ_x' (we also looked at the y-direction where the angle was assumed to be σ_y'). This setup is shown in Fig. 5.6.

We used the general transfer matrix [Lee]:

$$M = \begin{bmatrix} \sqrt{\frac{\beta_2}{\beta_1}}(\cos\Delta\psi + \alpha_1 \sin\Delta\psi) & \sqrt{\beta_1\beta_2}\sin\Delta\psi \\ -\frac{(1+\alpha_1\alpha_2)\sin\Delta\psi + (\alpha_2-\alpha_1)\cos\Delta\psi}{\sqrt{\beta_1\beta_2}} & \sqrt{\frac{\beta_1}{\beta_2}}(\cos\Delta\psi - \alpha_2\sin\Delta\psi) \end{bmatrix},$$

to find the offset and angle in the first resonator (assuming that β_x, β_y = 30m and α_x ,α_y=0 at the starting point). In the matrix, β_1 is the beta-function at the initial point, β_2 is the beta-function at the final point, α_1 is the alpha-function at the initial point, α_2 is the alpha-function at the final point, and $\Delta\psi$ is the betatron phase difference between the initial and final points.

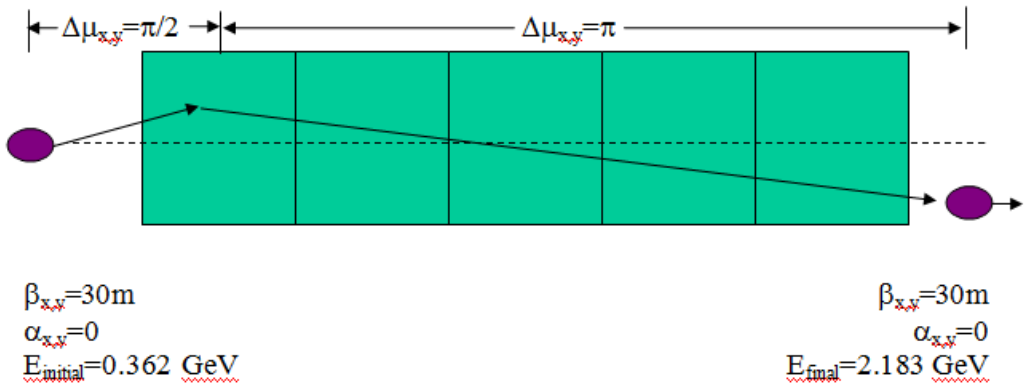

Figure 5.6. *Schematic of the five resonator model showing the first bunch having an angular deviation prior to entering the first resonator. The two purple ovals represent the same bunch as it goes through a betatron phase advance of 3π/2, entering with an angular deviation and leaving with an offset. The Twiss parameters at the starting and ending points are arbitrarily chosen, whereas the Twiss parameters inside the resonators correspond to actual Twiss parameters at the center of each resonator.*

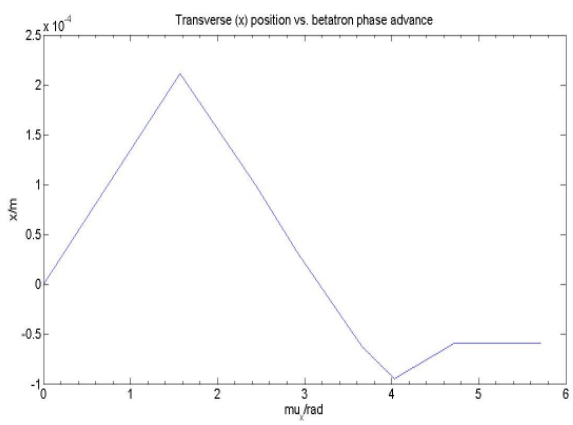

Figure 5.7: *Transverse position of a bunch moving through the five resonators without encountering any wake fields. This shows that the transfer matrix program works since the bunch goes from no offset (with an angle) to no angle (but with an offset) during a phase advance of 3π/2.*

Prior to starting the wake field calculations, we decided to test the program which applies the transfer matrix to find final offsets and angles from initial offsets and angles.

We chose an end point that has a $3\pi/2$ phase advance from the starting point. This way the transfer matrix program should take an initial angular deviation and turn it into an offset with no angle at the end. A plot of offset (in the x-direction) versus betatron phase advance along the linac is shown in Fig. 5.7.

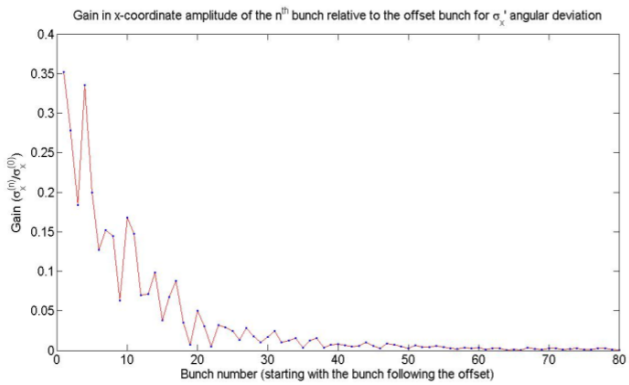

Figure 5.8. *Plot of the amplitude of betatron oscillations at the end of the linac normalized by the amplitude of betatron oscillations of the first bunch (σ_x at the end) when the first bunch starts with an angular deviation of σ_x'.*

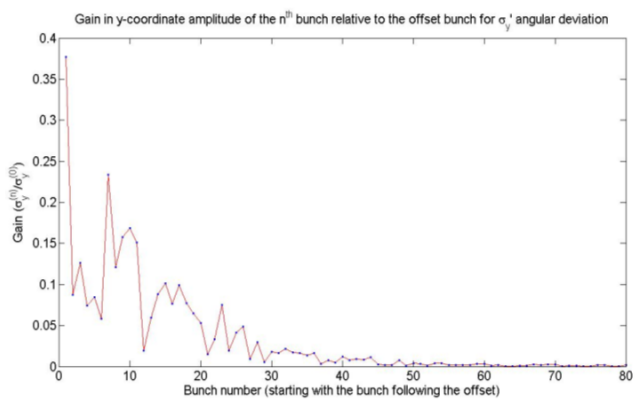

Figure 5.9. *Plot of the amplitude of betatron oscillations at the end of the linac normalized by the amplitude of betatron oscillations of the first bunch (σ_y at the end) when the first bunch starts with an angular deviation of σ_y'.*

From there on we calculate the wake left behind by the first bunch, apply it to subsequent bunches to find the angles they obtain and apply the transfer matrix (using actual Twiss parameter values and energies for the center of each resonator) to find offsets and angles in the next resonator. We continue in this manner through the five resonators. In order to make our results easier to see and understand, we pick our end point so that the total betatron phase advance from start to end is $3\pi/2$. We assume that the end point has the same Twiss parameter values as the starting point. We can then use the same definition of σ_{eff} (amplitude of betatron oscillations) that we had in the two-

resonator model, and again give our results in terms of the gain: $\sigma_{eff}/\sigma_{end}$, where σ_{end} is the amplitude of oscillation of the first bunch. Below are the results for the five resonator model for the cases of only one bunch starting with an angle (Figures 5.8 and 5.9), one bunch starting with an angle and all subsequent bunches also starting with the same angle (Figures 5.10 and 5.11), and the starting angle being given by a sinusoidal function with modulation frequency 10 kHz (Figures 5.12 and 5.13):

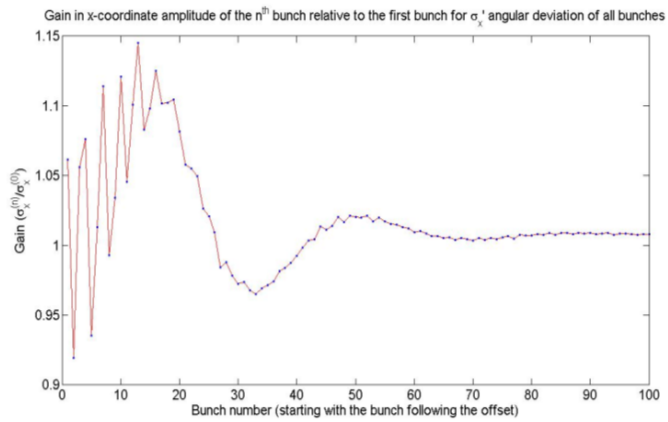

Figure 5.10. *Plot of the amplitude of betatron oscillations at the end of the linac normalized by the amplitude of betatron oscillations of the first bunch (σ_x at the end) when the all bunches start with an angular deviation of σ_x'.*

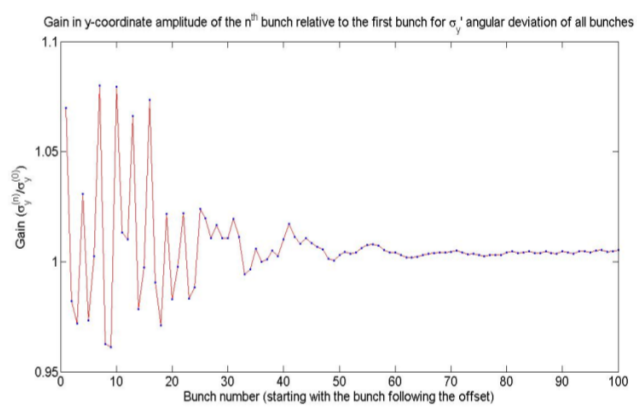

Figure 5.11. *Plot of the amplitude of betatron oscillations at the end of the linac normalized by the amplitude of betatron oscillations of the first bunch (σ_y at the end) when the first bunch starts with an angular deviation of σ_y'.*

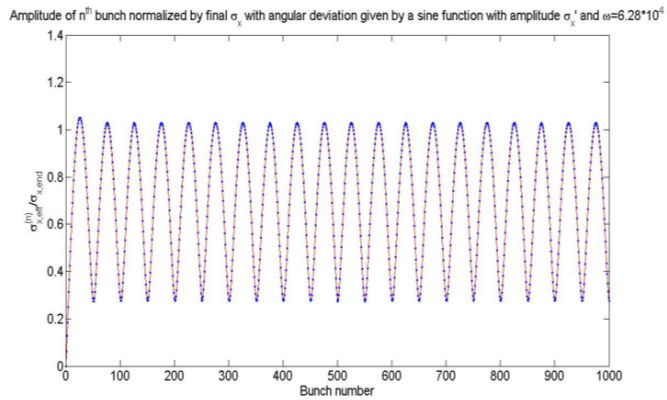

Figure 5.12. *Plot of the amplitude of betatron oscillations at the end of the linac normalized by the rms beam size (σ_x) at the end, when the first bunch starts with an angular deviation of σ_x'.*

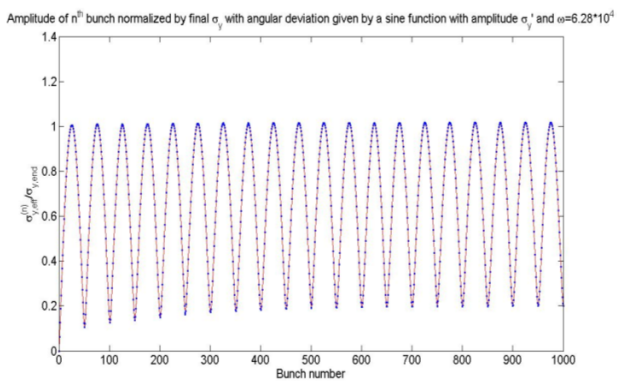

Figure 5.13. *Plot of the amplitude of betatron oscillations at the end of the linac normalized by the rms beam size (σ_y) at the end, when the first bunch starts with an angular deviation of σ_y'.*

From the above graphs (of the five resonator model) we can conclude that, although wake field effects are about ten times greater than in the two linac model, there is no evidence for multi-bunch beam break-up. Deviations of the first bunch by σ or σ′ (rms beam size or rms angular spread) lead to a maximum deviation of 0.4σ (or 0.4 σ′) in subsequent bunches. In addition, amplitudes of oscillations decrease along the bunch train, falling to zero after less than 100 bunches have passed (0.1ms). Even if all bunches (after some initial bunch) obtain angular deviations of σ′, a steady state is reached over the course of 100 bunches. In the steady state, bunches have an amplitude which is nearly σ, meaning that the initial deviation is not amplified by wake field effects. As in the two linac model, the beam is stable with respect to an element that causes bunches to enter the first resonator with a sinusoidal variation in angular deviation.

The results of the models we used suggest that long-range transverse wake fields will not lead to multi-bunch beam break-up in the BFA linac.

6. Start-to-end macroparticle tracking studies

Start-to-end macroparticle single-bunch simulations for the entire linac were carried out using the IMPACT code [Qiang *et al.* 2000, 2009] (see also Appendix A). Because at the time we conducted these studies the design of the electron gun was still evolving we did not try to make use of realistic macroparticle distributions generated by tracking through the injector. Instead, as the initial macroparticle distribution at the entrance of the linac (~40 MeV) we used an idealized distribution with Gaussian densities in all the phase-space coordinates except for the longitudinal space coordinate. For the beam longitudinal density we explored various profiles as shown in Fig. 6.1 with the intent to provide some guidance to the design of the injector. These profiles differ slightly in shape but all have approximately the same peak current (of the order of 70 A). In all cases we used the total charge of 0.8 nC and the normalized transverse emittance of 0.75 mm-mrad. As for the energy spread we considered a range of values as part of our effort to assess the microbunching instability. The simulations included the linac section with the laser heater chicane but did not include a realistic model of the beam-laser interaction. Instead, the effect of the laser heater is captured by an appropriate setting of the beam rms energy spread. The implied assumption is that the beam energy density resulting from the interaction with the laser is close to Gaussian.

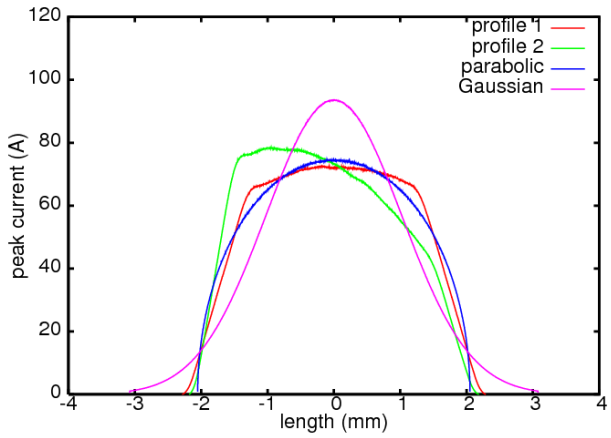

Figure 6.1: *Sample of longitudinal current profiles used in the simulations. They include a Gaussian (magenta), parabolic (blue), smooth flat-top (red), and ramped profile (green).*

A critical parameter for the simulations is the choice of the number of macroparticles N_{mp} Because of the microbunching instability (Sec. 2.2.5) the quality of the beam phase space at the exit of the linac is generally very sensitive to small current fluctuations present in the initial beam density. Using a number of macroparticles smaller than the bunch population $N_{mp} < N$ causes a random unphysical enhancement of the level of these initial fluctuations affecting the outcome of the simulation significantly. A substantial part of our effort has been to enable the IMPACT code with the capability of

carrying out high-resolution simulations employing a number of macroparticles comparable to a typical bunch population.

While we can easily estimate the scaling of the spurious effects introduced by a limited number N_{mp} of macroparticles used in the simulations (see Sec. 2.2.5) a more accurate and useful determination of the minimum requirement can be done by studying empirically the dependence on N_{mp} of sensitive quantities like the beam uncorrelated energy spread or the energy fluctuations at the exit of the linac. The result of this study is summarized in Fig. 6.2. The quantity plotted in the ordinate axis is the rms energy fluctuation averaged over all the slices along the bunch core. More precisely, this quantity is defined as $\sigma_{flct}^2 = \left\langle \left(\langle E \rangle_i - \overline{E} \right)^2 \right\rangle$, where $\overline{E}$ is the average beam energy after subtraction of long-scale smooth energy variations along the beam (caused *e.g.* by the nonlinearities of the rf waveform or the rf structures wake fields) and $\langle E \rangle_i$ is the energy centroid for the *i*-slice. The outer average is over the slices in the beam core. The picture shows two curves obtained from simulations with 2 and 5 keV initial beam uncorrelated energy spread. All other parameters in the simulations were kept the same. As expected, the energy fluctuations resulting from the smaller initial energy spread are notably larger and decrease with the number of macroparticles employed. While the current capabilities of IMPACT allow for up to 5B macroparticle simulations (equal to the population of a 0.8 nC electron bunch) it is apparent from the picture that there is little variation in the outcome between simulations with 1B and 5B. As a consequence in most of the remaining simulations discussed in this section we opted to use 1B macroparticles.

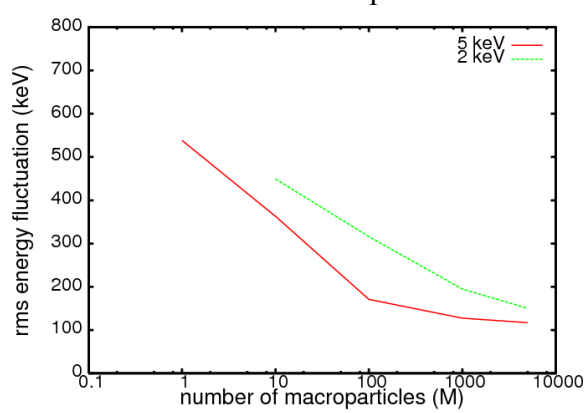

Figure 6.2: *Rms energy fluctuation at the end of the spreader as a function of the number of macroparticles. Two cases with 2 keV (red) and 5 keV (green) initial rms uncorrelated energy spread are shown.*

Fig. 6.3 illustrates the impact of the initial current profile on the slice energy spread at the end of the spreader obtained with 5 keV initial energy spread. The shape of these profiles has a noticeable impact on the phase space of the beam at extraction. Initial current profile with longer tails tend to cause filamentation and the appearance of 'bifurcations' as shown in Fig. 6.4 for the case of a beam with an initial Gaussian profile. By contrast, a parabolic initial current density, thanks to its more compact support, evolves into a distribution that occupies a relatively smaller area of phase space (See Fig. 6.5 and Fig. 4.14) thus resulting in a significantly smaller slice energy spread along the

bunch. The other intermediate profiles (*i.e.* the `ramp' and `smooth flat-top' shown in Fig. 6.1) yield results somewhat in between.

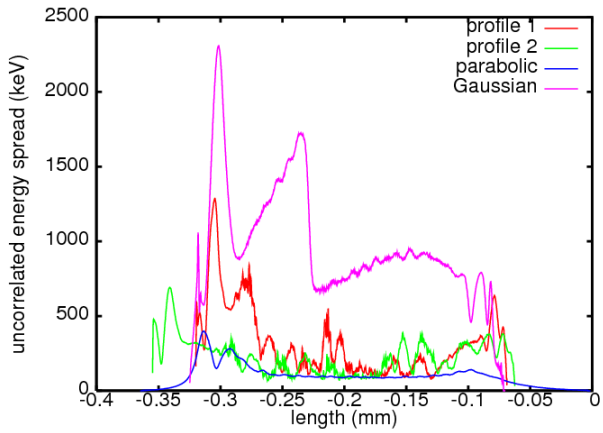

Figure 6.3: *The rms uncorrelated energy spread at the end of the spreader corresponding to the four initial longitudinal distribution profiles of Fig. 6.1: Gaussian longitudinal distribution (magenta), parabolic distribution (blue), distribution with ramped current (green) and distribution with a smooth flat-top (red).*

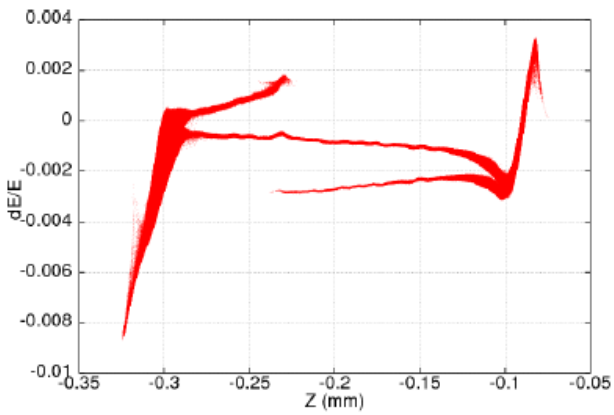

Figure 6.4: *The longitudinal phase space at the end of the spreader for initial Gaussian distribution.*

The profile of the bunch current impacts the beam evolution in the longitudinal phase space mostly through the response to the rf structure longitudinal wake fields excited by the bunch passage, the nonlinearity of the rf waveform and to some extent CSR. As already mentioned in Sec. 4.4 a beam phase space like the one shown in Fig. 6.4 is not very attractive as it is likely to induce uncontrolled beam losses, compromise the quality of the x-ray pulse in the FEL and interfere with diagnostics. This study suggests that an effort should be made in the design of the injector to control the beam current profile. If this effort does not succeed it may be necessary to develop an active system to remove the offending beam tails, like the one described in Sec. 4.4, to be located in the lower energy section of the linac.

The longitudinal phase space picture shown in Fig. 6.5 taken at the exit of the spreader is an example of a good-quality beam meeting the design requirement for the

FEL. The initial parabolic profile for the longitudinal density causes the particle in the bunch ends to remain relatively close to the core of the beam in phase space whereas the effect of the microbunching instability is evident in the slight modulation seen in the core of the beam but remains very modest. The apparently effective control of the microbunching instability is largely due to an adequate choice of the uncorrelated energy spread of the beam at injection with 5 keV, the value used for this example, close to the optimum. Decreasing the initial value of the energy spread to 2 keV, as indicated in Fig. 6.6 (red line), will increase the energy spread of the beam at extraction and enhance the random fluctuations characteristic of the instability. The same pictures also shows how increasing further the initial energy spread will keep the instability suppressed but will not help reduce the final energy spread, as a lower bound to the latter is given by the product between compression factor (about 17 in these examples) and the initial energy spread. Control of the slice energy spread in the beam injected into the linac is provided by a suitable tuning of the laser heater (Sec. 4.1).

The right picture in Fig. 6.6 demonstrates the insensitivity of the calculation to the choice of resolution for the grid used for charge deposition in the PIC algorithm in IMPACT, provided that the resolution is high enough to capture the small length scale of the fluctuations induced by the microbunching instability. Evidence of the spectral characteristics of the microbunching instability is seen in the ~15 μm energy modulation apparent in the beam core in Fig. 6.5. The period of this modulation is consistent with expectations from the linear analysis [Heifets *et al.*, Huang *et al.* 2002, Venturini 2007b] of the microbunching instability. The spectral properties of the instability are determined by the gain function through the bunch compressor shown in Fig. 6.7. The peak of the gain corresponds fairly well to the 15 μm modulation after accounting for compression (factor 17). We remind the reader that the gain function is defined by placing a (small) sinusoidal density modulation on the beam at the beginning of the beamline under consideration and taking the ratio between the relative amplitudes of the modulation at exit and entrance of the beamline.

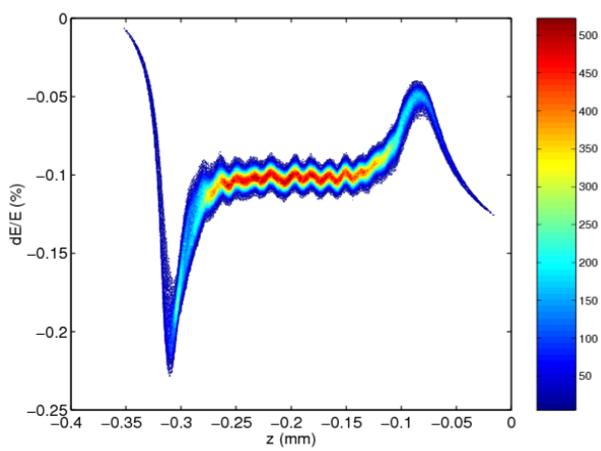

Figure 6.5: *The longitudinal phase space at the end of the spreader for initial longitudinal density profile and Gaussian energy density with 5 keV uncorrelated rms energy spread.*

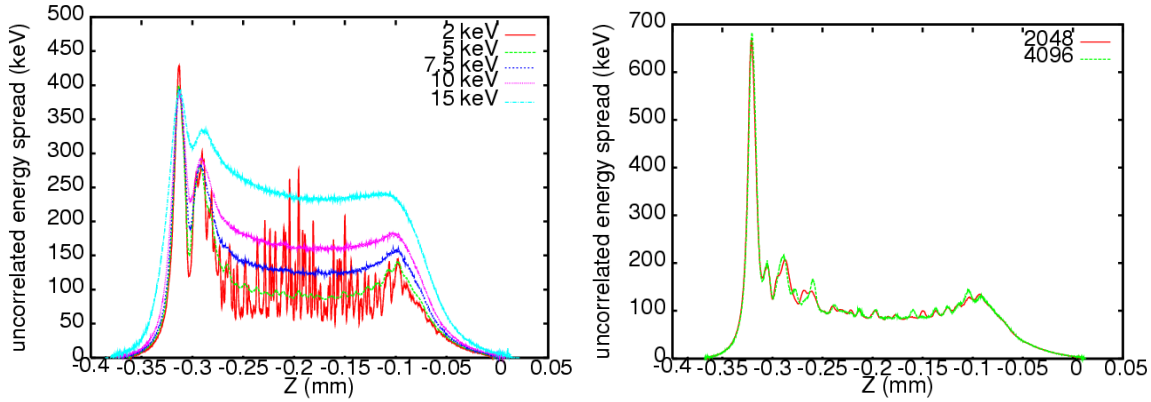

Figure 6.6: *Picture to the left: rms slice energy spread at the end of the spreader starting from an initial parabolic distribution with 2 keV (red), 5 keV (green), 7.5 keV (blue), 10 keV (magenta), and 15 keV (light blue) rms energy spread at the beginning of the linac. The two curves in the picture are results obtained from two IMPACT runs employing a grid with 2048 (red) and 4096 (green) cells (5 keV initial energy spread in both cases).*

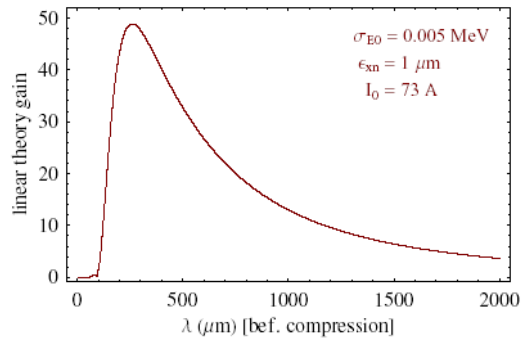

Figure 6.7: *The spectral gain of the microbunching instability calculated using linear theory for 5 keV initial uncorrelated energy spread from the entrance of the linac through the bunch compressor.*

Fig. 6.8 shows the current profile (picture to the left) at the end of the spreader corresponding to the beam of Fig. 6.5 as well the slice emittances along the bunch (picture to the right). The current profile is satisfyingly smooth. The small fluctuations seen in the core of the beam, which we believe are the result of the microbunching instability are clearly very mild. The picture to the right in Fig. 6.8 shows no evidence of slice emittance growth. However we should point out that a potential source of projected emittance growth, rf transverse wakes were omitted in these studies. While we believe their impact should be modest and controllable [Craievich *et al*. 2009] they will require a careful evaluation. Also, in these simulations transverse space-charge forces were purposely turned off in order to preserve the beam matching against the linear (unperturbed) lattice. We believe that transverse space-charge effects, which are essentially limited to the low-end energy span of the linac, can be successfully handled. A

validation of this assumption, will have to wait for more complete simulation studies integrating the injector section into the linac. Finally, Fig. 6.9 shows the evolution of the projected transverse emittance along the machine. The growth (about a factor 2.5) in the horizontal plane is essentially due to CSR in the bends of the bunch compressor. This projected emittance growth is mostly concentrated in the tail regions of the beam as indicated by Fig. 6.10 and is produced by relatively large beam centroid offsets in x and p_x. The projected transverse emittance for the core of the beam comprising 64% of the electrons is only 0.94 μm (but still larger than the ~0.7 μm slice emittance because of residual x/z and p_x/z CSR-induced correlations). While the projected emittance observed at the exit of the linac would not compromise lasing in the FEL [Xiang *et al.*], further studies will be needed to determine whether this value would be consistent with the diagnostics requirements.

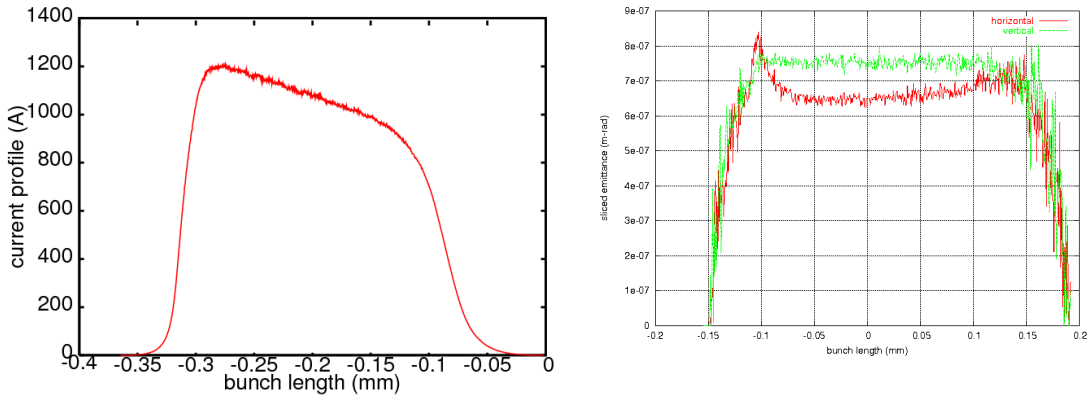

Figure 6.8: *Current profile along the bunch (picture to the left) and horizontal (red), vertical (green) slice emittance at the exit of the spreader (picture to the right) starting from a 0.8nC bunch with parabolic longitudinal density, 5 keV rms uncorrelated energy spread and 0.75 μm(horizontal and vertical) normalized rms emittance.*

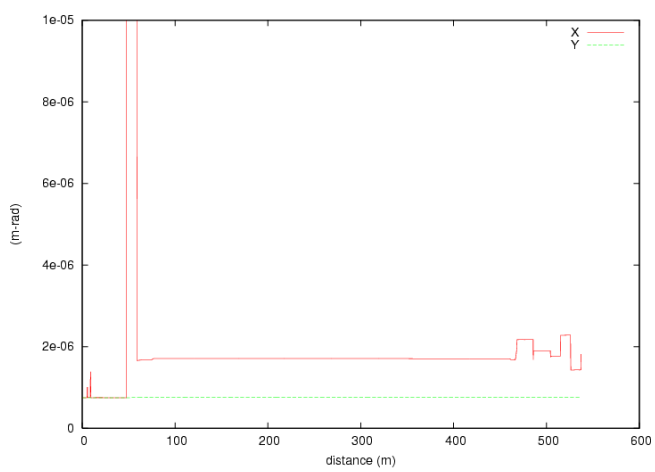

Figure 6.9: *Evolution of the horizontal (red) and vertical (green) rms projected emittance along the linac and through the spreader.*

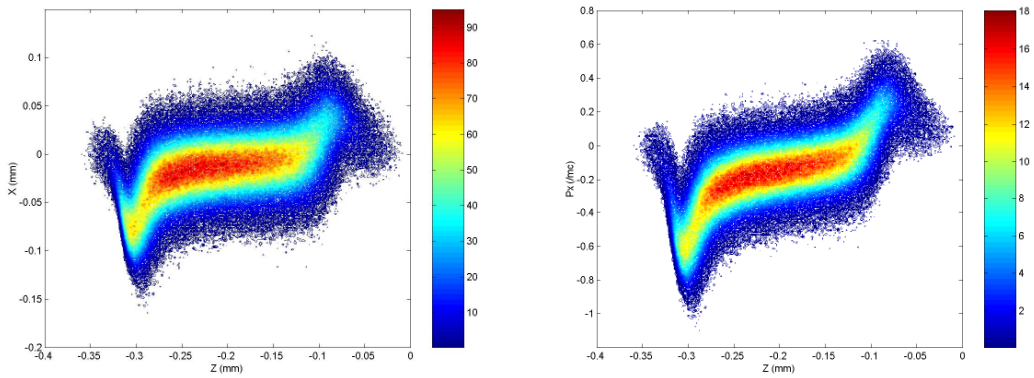

Figure 6.10: *The projections of the beam phase-space density in the x/z (left picture) and p_x/z (right picture) at the exit of the spreader.*

7. Jitter studies

The electron beam delivered by the linac is subject to jitter in key properties due to errors and fluctuations in its component parts. Parameters of particular interest are the electron beam energy and energy chirp, bunch length, current, arrival timing at the FEL. The importance of stable beam energy is to maintain the resonance condition in the FEL, otherwise the gain length and x-ray power output could suffer large fluctuations with electron energy. X-ray power output also depends on the bunch current. The timing and bunch length jitter should be controlled to maximize the interval of time over which the electron beam can be reliably seeded by a laser to produce good output in the FEL. Energy chirp in the beam can lead to shifts in the wavelength of the output radiation, although this is more of a concern when narrow bandwidth pulses are desired.

7.1 Simulation technique

To analyze the sensitivity of the electron beam to errors, the entire beamline must be considered. The beamline is modeled in LiTrack [Bane *et al.* 2005] from the photocathode through the spreader, based on a preliminary injector design provided in Ref. [Lidia] and on the reference linac design. LiTrack tracks particle energy and longitudinal position, models basic accelerator components, and allows for prescribed longitudinal wake fields. An additional feature of modeling jitter in chicanes was used as implemented in [Craievich *et al.* 2006]. The physics model is most appropriate for highly relativistic beams. There is no modeling of space charge or CSR, so some physics is left out that might contribute to sensitivities to linac parameters. Slight perturbations to a few linac parameters were made in order to reproduce the desired beam profile at the end of the accelerator. In addition, the initial electron beam leaving the cathode is replaced by a

mock distribution used by running LiTrack backwards starting from a reasonable distribution at 40.8 MeV. This was necessary to simulate the entire injector and linac within the physics model used by LiTrack. We note that the current injector design targets obtaining the distribution at 40.8 MeV that we use here.

Many sources of jitter are examined in the LiTrack simulations. Two fluctuating parameters of the initial beam are the charge per bunch and the time of impact of the photocathode laser on the photocathode. The error in this time of impact, as well as the final timing of the electron bunch, is measured with respect to a fixed, ideal reference time that governs the entire system, including RF. The phase-space distribution of the electrons leaving the cathode is fixed. Shifts in these parameters are particularly important because they continue to affect beam propagation throughout the injector and linac, altering wake fields and the RF phases experienced by the beam. All RF cavities are allowed to fluctuate in both peak accelerating gradient and phase. In addition, the strength of the chicanes in the bunch compressor and the spreader fluctuate. While low-energy drift sections are modeled as generalized dispersive sections, their parameters are fixed by the drift length and do not have jitter.

The elements of the injector are the photocathode, which is inside the cathode RF cavity at 100 MHz, a drift section, a buncher RF at 650 MHz for velocity compression, a second drift, and the injector acceleration stage which consists of 6 RF cavities at 1300 MHz and accelerates the beam up to 40.8 MeV. After the injector, the beam passes through linac 1 which has 18 RF cavities at 1300 MHz and accelerates the beam up to 240 MeV, then the third harmonic RF at 3900 MHz which has 7 cavities, the chicane for bunch compression, linac 2 which has 162 RF cavities and accelerates the beam to the final energy of 2.4 GeV, and the spreader which has nonlinear dispersion but $R_{56} = 0$ (see schematics in Fig. 1.1).

Listed beam parameters, such as energy or current, are either given at a nominal external reference time, which is fixed to be the arrival time for the center of the nominal beam, or as an average over a 0.5 ps interval centered about this reference time. Additional parameters are the bunch length (total duration head to tail) and the shift in the final arrival time for the center of the bunch relative to the external reference time. Fluctuations in these parameters, as well as for beamline errors, are given in terms of their rms values.

We first consider errors that are completely uncorrelated, both from shot-to-shot and among different beamline elements. We then model the time evolution of errors using a characteristic power spectral density (PSD) function. The error function for each element is built up out of randomly phased frequency bins spaced 1 Hz apart, ranging from 1 to 300 Hz. Based on experimental observations of acoustic noise [Portmann *et al.*], the power spectral density is assumed to be flat over the range 1 to 20 Hz, and then to decreas at higher frequencies as $1/f^4$, where f is the frequency. Excluding frequencies above 300 Hz has a negligible effect. All sources of jitter are taken to have a similar PSD function except for the charge per bunch, which is assumed to fluctuate on a shot-to-shot basis because these errors are not expected to have a mechanical or electrical basis which would evolve over longer time scales. The effect of variation in the charge thus tends to stand out over short time scales. A spatial correlation is also considered, where RF cavities in linac 2 are assumed to be grouped into cryomodules of 9 cavities each, and all the RF cavities in a single cryomodule are taken to have identical power and phase errors,

although neighboring cryomodules are still uncorrelated. Similarly, all third harmonic RF cavities are taken to have identical errors. This increases fluctuations in the final beam by reducing the number of statistically independent errors.

Finally, a simple model for the effectiveness of a feedback system is used. Measurements of beam jitter could be taken for the final beam or earlier in the acceleration stage, such as at the end of the bunch compressor, and could then be corrected by feedback, for example with dedicated RF cavities. However, rather than modeling the feedback directly, we consider a generic feedback system and apply the general rule that a well-designed feedback system should yield similar results as if the noise inputs were all reduced. We model the system with feedback by taking the PSD at each frequency f and reducing it by a factor $1+(\sqrt{N}/10Tf)$, where T is the time resolution of the feedback system and N is the number of measured quantities that the feedback system reacts upon. Here $N = 3$, for example bunch energy, arrival time and bunch length could be measured. The time resolution T of the feedback system is taken to be either 1 ms or 0.1 ms. The feedback does not act on the errors in the bunch charge, which vary shot-to-shot.

The nominal charge per bunch is 0.8 nC, and the current in the core of the beam is approximately 9 A. The local compression factor in the core of the bunch is 7.5 going from the initial distribution to the end of the injector, and the bunching chicane compresses the bunch by an additional factor of 12. With no beamline errors, the rms standard deviation in energy in these simulations is 20 keV. The current at the nominal center is 0.847 kA, and the rms standard deviation in current is 34 A. To suppress the effects of short-scale statistical noise in the beam profile, the energy and current profiles are generated by smoothing the values per bin over the 0.5 ps region through an 8th-order polynomial fit. The smoothing is particularly important for the current profile, taking the rms standard deviation down to 25 A, and for derivatives. A low energy spread is used in these simulations in order to highlight short-wavelength wakefield effects, which tend to be suppressed by large energy spreads. The rms slice energy spread in the core of the final beam is about 23 keV. For the ideal configuration, there is approximately 650 fs over which the beam current, energy, and energy spread are all close to nominal parameters.

7.2 Global Jitter Studies

Simultaneous, uncorrelated errors in all parameters were simulated in LiTrack. Results are summarized in Table 7.1, where a linear analysis is used to obtain the contribution of key beamline sections to electron beam fluctuations for given moderate errors. The ``null'' row serves as a measure of nonlinear effects. The calculation of jitter caused by sections with multiple RF cavities includes partial cancellations caused by uncorrelated errors, and so the total contribution is approximately the square root of the number of cavities times the jitter caused by a single cavity error. Global errors can be estimated by scaling fluctuations from individual elements for the expected error, and adding the results in quadrature.

Table 7.1: The contributions of various sources of jitter to fluctuations in output average beam energy, average current, bunch length, and the shift in arrival time. Energy and current are averaged over a fixed 0.5 ps interval. The sign represents the sign of the perturbation when the input error is positive.

Quantity	Amount	Contribution to Jitter in:			
		Energy [keV]	Current [A]	Bunch length [fs]	Arrival time [fs]
charge	1%	-25.5	-1.9	11.3	6.0
timing	100 fs	8.5	-0.68	1.9	-0.83
cathode voltage	0.01%	-33.3	8.1	-8.7	1.1
cathode phase	0.1 degree	-2.1	2.2	-0.73	-0.43
buncher voltage	0.01%	4.2	-1.5	1.3	-0.15
buncher phase	0.1 degree	-220	50.7	-56.3	5.7
injector accel voltage	0.01%	0.83	1.3	0.14	-3.0
injector accel phase	0.1 degree	1.8	-5.2	5.3	-0.93
linac 1 voltage	0.01%	0.76	-1.1	0.43	-10.0
linac 1 phase	0.1 degree	11.5	26.7	21.0	-51.7
third harmonic voltage	0.01%	-1.3	1.1	-0.14	1.7
third harmonic phase	0.1 degree	-3.4	7.1	-8.7	0.53
chicane	0.01%	9.7	3.8	-1.1	22.3
linac 2 voltage	0.01%	16.8	0.092	0.0033	-0.037
linac 2 phase	0.1 degree	10.1	1.5	-0.063	0.13
spreader	0.01%	-0.43	1.4	-0.016	0.13
null	–	0.13	0.13	0.024	0.033

7.3 Time-Dependent Model

Having looked at completely uncorrelated noise errors, we now consider the time-dependent model. Nominal rms beamline errors used are 2% for the charge per bunch, 300 fs for the time of impact of the photocathode laser pulse, 10^{-4} for the RF peak gradient, 0.1 degree for the RF phase, except for the cathode RF which is allowed to jitter by 2×10^{-4} in peak gradient and 0.2 degree in phase, and 10^{-4} for the strength of the chicane and spreader. In each plot below, the curves represent single shots separated by 1 ms in time. A total of 250 shots, corresponding to 250 ms of beam variation, is shown. The charge per bunch errors are assumed to be uncorrelated in time. For all other error terms from a single element, the PSD is normalized so that the the rms of the combined error from all frequency bins yields the nominal error level. Results are shown in Fig. 7.1.

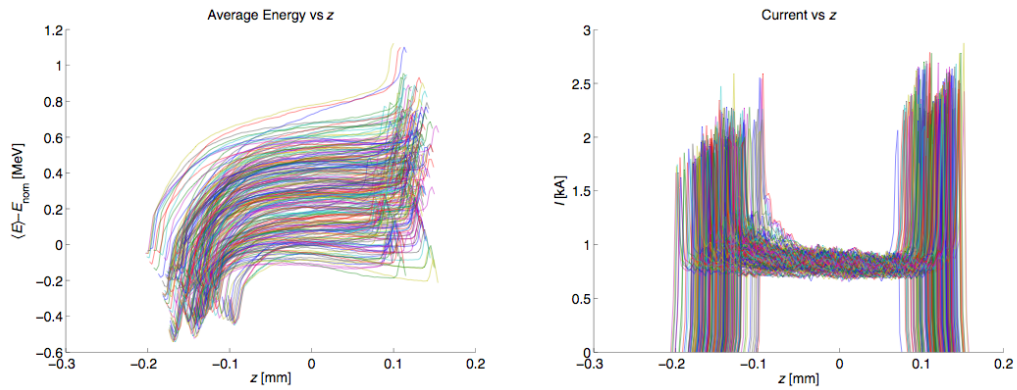

Figure 7.1: Energy (left) and current (right) profiles for simulations of sample electron bunches over a 250 ms time period, adopting the assumed noise spectrum.

The same simulations are repeated for the feedback model with either 1 ms or 0.1 ms time resolution. The feedback model dramatically improves performance, as shown in Figs. 7.2 and 7.3. With feedback, the charge per bunch variation becomes much more significant as a driver of jitter in electron beam parameters. Charge per bunch fluctuations have a distinctive signature, as they affect longitudinal wake fields (recall that space-charge effects are not modelled by LiTrack). Therefore, the head of the bunch is not affected but the tail of the bunch is very sensitive to charge per bunch. With the faster feedback system, although the head of the bunch is extremely stable, variations in the tail of the bunch are not much improved.

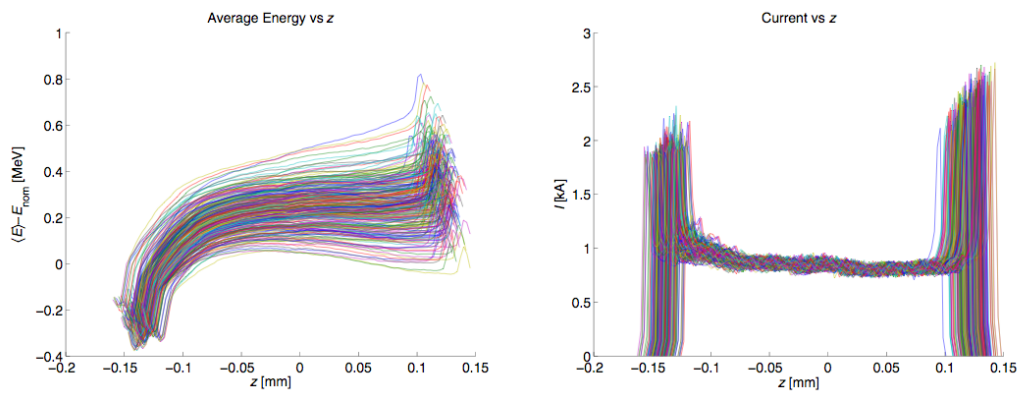

Figure 7.2: Energy (left) and current (right) profiles for simulations of sample electron bunches over a 250 ms time period, using the prescribed noise spectrum and including a generic feedback model with 1 ms time scale.

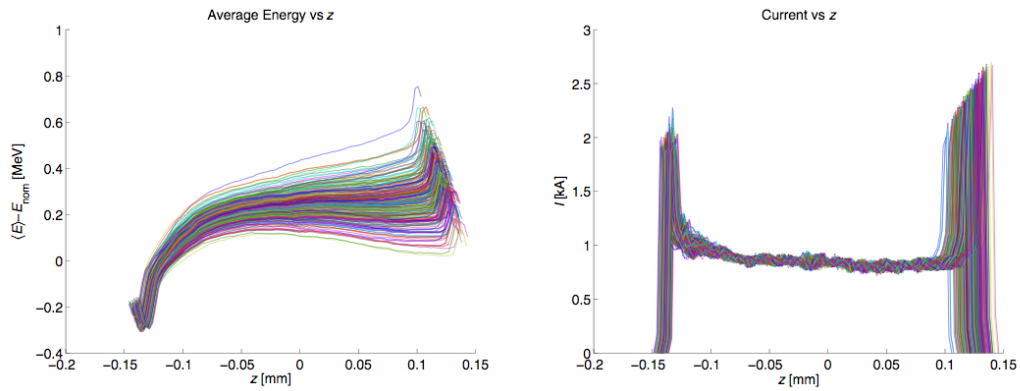

Figure 7.3: Energy (left) and current (right) profiles for simulations of sample electron bunches over a 250 ms time period, using the prescribed noise spectrum and including a generic feedback model with 0.1 ms time scale.

Qualitatively, the charge per bunch jitter is the main driver of fluctuations in the energy chirp. For the case without feedback, the timing fluctuations of the head of the bunch are equal to that of the tail, unlike what would be expected from charge per bunch contributions. The jitter with no feedback is sufficiently large that linear perturbation models do not yield accurate results, but with feedback the overall errors are reduced and the linear model is in fair agreement. For the T = 1 ms feedback model, the bunch length errors are larger than the arrival time errors, in agreement with the first row of Table 7.1. For the T = 0.1 ms feedback model, the charge fluctuations are the dominant effect. The timing variations of the head of the bunch are reduced to 7 fs, and the tail and bunch length jitter are 25 fs; the arrival time error lies in between these values at 15 fs. The fluctuations in beam energy, current, bunch length, and arrival time are given in Table 7.2, along with estimates of the contribution of charge fluctuations. Repeating the simulations without any charge per bunch jitter, fluctuations in the energy could be reduced to as low as 21 keV, in the current to 6 A, in the bunch length to 6 fs, and in arrival time to 5 fs.

Table 7.2: Jitter in beam energy and current at the fixed reference time, and in the bunch length and arrival time. Results are given for the nominal rms errors and PSD function, for the cases with no feedback, feedback with a 1 ms resolution, and with a 0.1 ms resolution. Includes estimates for the contribution of charge fluctuations, where possible.

Parameter	no feedback	T = 1 ms feedback	T = 0.1 ms feedback
Energy [keV]	200	75	45
contrib from N_e	58	44	40
Current [A]	47	19	11
contrib from N_e	–	9	9
Bunch length [fs]	61	30	25
contrib from N_e	5	23	25
Arrival time [fs]	54	21	15
contrib from N_e	17	15	15

When considering advanced feedback systems, the issue of whether bunch charge or other errors have significant shot-to-shot variations becomes more critical to performance. Reliable estimates of the magnitude and temporal structure of errors will have to be obtained from hardware studies. Taking the above nominal jitter values for beamline errors, the rms energy fluctuations range from 200 keV to 45 keV depending on whether and what type of feedback systems are used. Timing jitter can likewise be reduced by feedback from 54 fs to 15 fs, and jitter in the central current from 47 A to 11 A. Fluctuations in the energy chirp are dominated by the error in the charge per bunch and feedback systems may not be able to stabilize this quantity. It remains to determine the effect of these fluctuations on FEL performance. A more information can be found in [Penn 2009].

8. Conclusion

In this Report we have analyzed the most critical aspects of the accelerator and beam dynamics for a proposed soft x-ray free electron laser at the Lawrence Berkeley National Laboratory. Our study includes the design, optimization, and characterization of the machine using advanced analytical tools and state-of-the-art high resolution macroparticle simulations. We demonstrate the feasibility of feeding ten FELs with high brightness beams of electrons at a 100 kHz bunch repetition rate with up to 0.8 nC charge per bunch and 1 kA peak current, a normalized transverse slice emittance smaller than 1 μm, an uncorrelated energy spread smaller than 100 keV, and a final energy of 2.4 GeV. Our conclusions are based on an ideal lattice. A study of the sensitivity of the electron beam parameters to misalignment errors and lattice errors is deffered to a future detailed design. However, we found that the remarkable stability in the electron bunch peak current, length, energy, and arrival time at the FEL can be achieved by correcting jitter errors in the linac using dedicated feedback systems that take advantage of the high bunch repetition rate. Future design work will also include development of diagnostics systems taylored to this machine. A closer look at effects that have not been sufficiently investigated (*e.g.* transverse space-charge at the low-energy end of the accelerator) is in our plans as well.

9. Acknowledgements

Work supported by the US Department of Energy under contract No. DE-AC02-05CH11231. We gladly acknowledge fruitful discussions and comments from J. Byrd, J. Corlett, M. Cornacchia, P. Craievich, S. Di Mitri, L. Doolittle, P. Emma, W. Fawley, Z. Huang, S. Lidia, G. Penco, A. Ratti, R. Ryne, F. Sannibale, J. Staples, and J. Wurtele.

Appendix A: The parallel tracking-code IMPACT

IMPACT [Qiang *et al.* 2000] is a suite of parallel particle-in-cell codes, designed for modeling high intensity, high brightness beams in rf proton linacs, electron linacs and photoinjectors. It consists of two parallel particle-in-cell tracking codes (one is longitudinal position-dependent and one is time-dependent), an rf linac lattice design code, an envelope matching and analysis code, and a number of pre- and post-processing codes. The present version of IMPACT can treat intense beams propagating through drifts, magnetic quadrupoles, magnetic solenoids, magnetic dipoles, and rf cavities, using map integrators and nonlinear Lorentz integrators.

The codes implements a novel treatment of rf cavities [Abell], in which the gap transfer maps are computed during the simulations by reading in rf fields on axis calculated using for example the SUPERFISH code [SUPERFISH]. This feature permits avoiding time-consuming (and unnecessary) fine-scale integration of the orbit of the individual particles through the highly z-dependent cavity fields. Instead, fine-scale integration is used to compute the maps (which involve a small number of terms), and the maps are then applied to advance the particle orbits (this is analogous to techniques used to simulate beam transport through magnets with fringe fields. Recent additions include new capabilities for modeling short-range longitudinal and transverse wake fields as well as 1D CSR wakes (the latter for now do not allow for transient effects through the dipole magnets ends).

Both parallel particle tracking codes of the IMPACT suite assume a quasi-static model of the beam and calculate space-charge effects self-consistently at each time step together with the external acceleration and focusing fields. The 3D Poisson equation is solved by depositing the charge onto an adaptive 3D Cartesian grid and solving for the potential on the grid in the beam frame. The resulting electrostatic fields are Lorentz transformed back into the laboratory frame to obtain the space-charge forces of the beam. The user can chose among six Poisson solvers, corresponding to transverse open or closed boundary conditions with round or rectangular shape, and longitudinal open or periodic boundary conditions. These solvers are based on either a spectral method for closed transverse boundary conditions, or a convolution-based Green function method for open transverse boundary conditions. The convolution for the most widely used open boundary condition Poisson solver is calculated by means of an FFT with doubled computational domain. The computing time of this solver scales as $N \log N$, where N is number of grid points. The parallel implementation is based on a two-dimensional domain decomposition approach for the three-dimensional computational domain.

The IMPACT simulations used for this Report were carried out on the National Energy Research Scientific Computing Center (NERSC) facilities [NERSC]. The end-to-end runs employing 1B macroparticles reported in Sec. 6 were typically distributed on 512 processors taking about two hours to complete.

A typical example of a set of benchmarks that we carried out to validate the code is shown in Fig. A.1. Here we compare the linear gain of the microbunching instability from the laser heater through the bunch compressor of the BFA linac as detemined by IMPACT and linear theory [Heifets, Venturini 2007b]. The calculation was done for a slightly modified version of the lattice considered in this study. The good agreement

shown by the picture is a validation for both the macroparticle simulations as well the simplified model of dynamics embodied by linear theory.

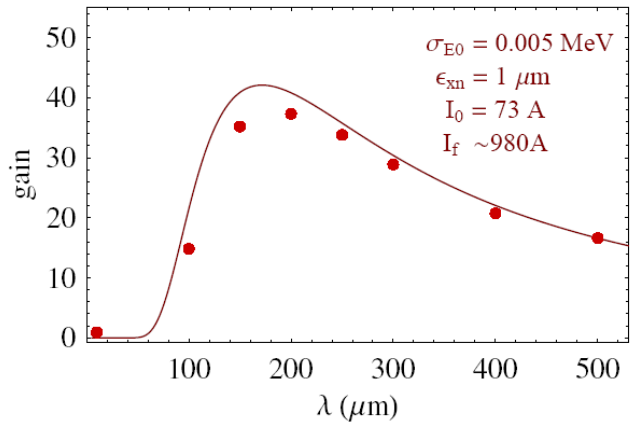

Figure A.1: *Linear gain for the the microbunching instability through the bunch compressor. The results from IMPACT calculations (dots) are in good agreement with analysis based on linear theory (solid line). Electron beam parameters before compression and electron peak current after compression are shown in the top right corner.*

Appendix B: Vlasov solver

Direct numerical solution of the Vlasov equation represents a complementary approach to the more prevalent method of simulating beam dynamics by macroparticle traking. In particular a Vlasov solver offers the advantage of being immune from the statistical fluctuations stemming from using a limited number of macroparticles, which may interfere with a correct interpretation of the results when studying the microbunching instability (see Sec. 2.2.5). Small scale structures are more easily resolved and instabilities more accurately characterized. Moreover, in contrast to semi-analytical studies based on the linearized Vlasov equation, numerical solutions of the full equation can be used to investigate saturation effects, which may be important.

It should be pointed out, however, that the Vlasov solver cannot be expected to substitute macroparticle simulations as the burden both in terms of developing suitable numerical algorithms and required computational resources limits the dimensionality of phase space that can be explored (the computational cost scales quite unfavorably with the phase-space dimension). At this time only a 2D phase-space solver is fully available and functional and the physics that can be investigated for now is limited to the short-scale effects of collective forces causing microbunching. Studies based on numerical solutions of the Vlasov equation should be seen as occupying a middle ground between the semi-analytical analysis based on the linearized Vlasov equation and macroparticle simulations.

Here we briefly discuss 2D longitudinal phase-space Vlasov solver developed in [Venturini *et al.* 2007] that we used in studying the lattice design for the BFA machine and to generate the data reported in Fig. 4.6. The solver implemented as a Fortran code finds numerical solutions of the equation:

$$\frac{\partial f}{\partial s} - \delta \frac{D}{R}\frac{\partial f}{\partial z} + F(z)\frac{\partial f}{\partial \delta} = 0\,, \tag{B.1}$$

where

$$F(z) = -\frac{e^2 Nc}{E_0}\int dk Z(k)\hat{\rho}(k)e^{ikz} \tag{B.2}$$

is the collective force expressed in terms of an impedance per unit length *Z(k)* and the Fourier transform $\hat{\rho}(k)$ of the longitudinal bunch density. The existing code allows for inclusion of models of impedance describing space charge, coherent synchrotron radiation (CSR), and possibly rf structure wake fields (although the latter have no consequence on the microbunching instability). In particular CSR is evaluated in free space on the assumption that the bunch follows a trajectory with uniform radius of curvature, thus excluding transition effects through the entrance and exit of bending magnets. Incidentally this is the same model presently implemented in IMPACT [Qiang *et al.* 2009]. The numerical solution of (B.1) is found using a variation of the time-splitting method that was already used to study the longitudinal beam dynamics in storage rings [Venturini *et al.* 2005]. A technical complication arising when treating single pass systems and in particular bunch compressors is the presence of a large correlation in the beam density in the z-δ plane. The method implemented in the code tackles this complication by solving Eq. (B.1) in a new coordinate system where the correlation is removed. In the new coordinates the density function for the beam is represented on a rectangular grid with adapting cell sizes to follow the bunch compression in the longitudinal coordinate (and the corresponding stretching in canonical momentum). For a detailed description of the method we refer to [Venturini *et al.* 2007a].

A possible concern regarding the study of a purely longitudinal phase space is the seeming neglect of the smearing effect to microbunching caused by a finite transverse emittance. While it is true that a complete accurate assessment of the effect of transverse emittance should entail the inclusion of the dynamics in the horizontal plane as well, we argue that it is possible in 2D to account for this smearing in an approximate but meaningful way by introducing an effective low-pass filter in the evaluation of the collective force. In particular we contend that (B.2) should be replaced with

$$F(z) = -\frac{e^2 Nc}{E_0}\int dk Z(k)\hat{\rho}(k)e^{ikz}\exp(-k^2\sigma_\perp/2)\,, \tag{B.3}$$

where

$$\sigma_\perp = \sqrt{2\varepsilon_x \mathcal{H}}; \quad \mathcal{H} = \gamma_x D^2 + 2\alpha_x DD' + \beta_x D'^2. \tag{B.4}$$

Confidence in the validity of the above model of emittance-induced smearing can be obtained from comparison with predictions from linear theory [Heifets *et al.*] in the regime where linear theory applies [Venturini *et al.* 2007a].

In the reminder of this section we illustrate the application of the solver to the study of FERMI@elettra lattice [Bocchetta *et al.*] which presents many of the problems

posed by the machine discussed in this paper. Fig. B1 shows the gain curves for a beam through approximately 36 m of transport line including a section of accelerating linac (from E=96 to 233 MeV) followed by a chicane for bunch compressor. The beam is a flattop with gaussian energy density and 10 keV rms energy spread, ε_x=1 μm normalized transverse emittance, and I=191 A peak current The two pictures contrast the case where the smearing effect of the horizontal emittance is taken into account (left picture) to the case where it is not (picture to the right; in which case a finite value of the emittance $\varepsilon_x=\varepsilon_y=1$ μm is still assumed for the purpose of determining the bunch sizes along the lattice). Notice how the transverse emittance smearing effect substantially reduces the gain at small wavelengths. Good agreement is found with linear theory (solid lines).

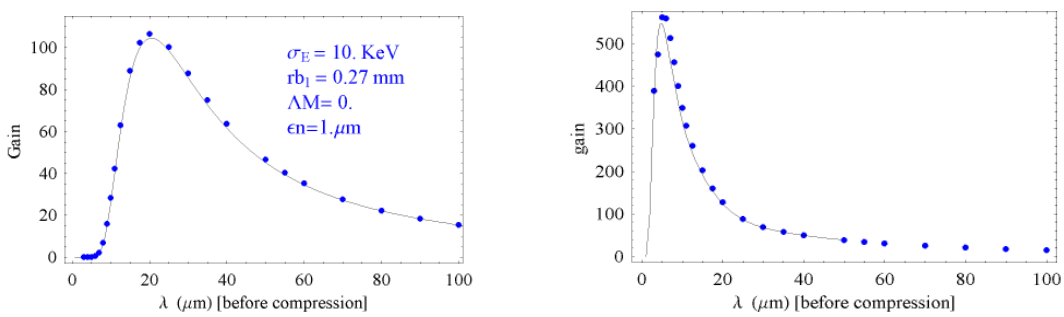

Figure B.1: Gain curves through for L1+BC1 in the presence of CSR and space charge (with space charge excluded in BC1) as determined by linear theory (solid line) and from the numerical solutions of the Vlasov equation (blue dots). σ_E=10 κeV; smearing effect of transverse emittance is included in the left but not in the right picture.

The results from simulations through a longer portion of the linac including both the bunch compressors present in the FERMI lattice design are reported in Fig. B.2. The pictures show snapshots of the longitudinal phase space detailing the evolution of the microbunching instability seeded by shot noise for a choice of beam parameters causing the instability to be particularly strong. The snapshots are taken right after the first bunch compressor BC1 (top left picture) at the entrance of the second bunch compressor (top right picture), after the 3rd dipole in BC2 (bottom left picture) and at the exit of BC2 (bottom right picture).

The initial beam density is a flattop in charge density and Gaussian in the (uncorrelated) energy spread. The shot noise was modeled by perturbing the initial, smooth density function in phase space with random noise specified as follow. Having denoted with (q,p) the pair of canonical coordinates (q is a normalized longitudinal coordinate, p the energy) the density function $f = f(q_i,p_j)$ is represented on a Cartesian grid with cells of size Δq and Δp. Indicate with $f_{ij}^{(0)} = f^{(0)}(q_i,p_j)$ he smooth density; we set the initial density with random noise to $f_{ij}= f_{ij}^{(0)}(1 + \xi_{ij})$ where ξ_{ij} is a stochastic variable with normal law distribution, vanishing average and variance $\sigma_\xi = N_{ij}^{-1/2}$, where $N_{ij} = N f_{ij}^{(0)}\Delta q\Delta p$ is the number of electrons contained in the $\Delta q\Delta p$ cell of phase space.

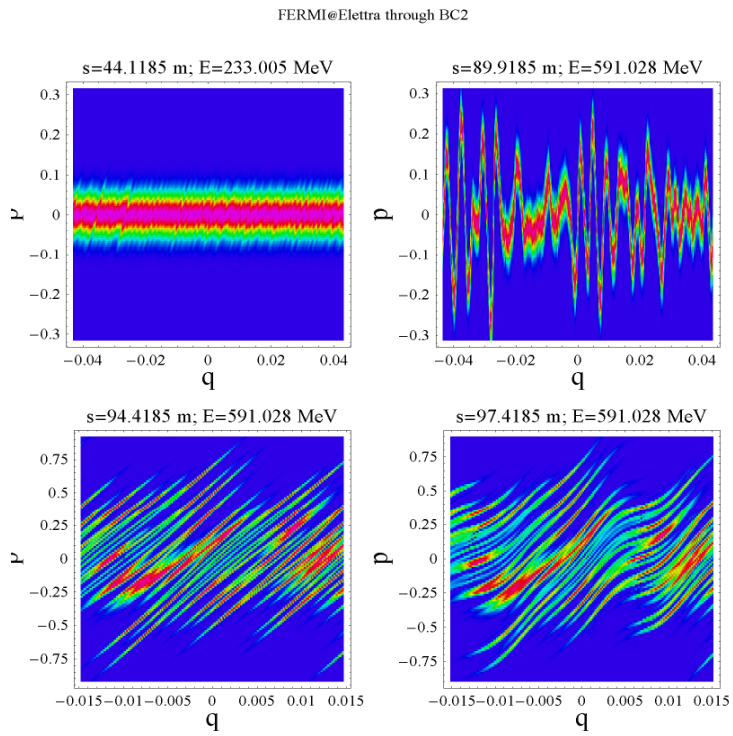

Figure B.2: Longitudinal phase space at selected locations along the linac starting from a noisy flat top bunch with Gaussian rms energy spread; s=0 corresponds to the start of the laser-heater section. The top left pictures is taken at the exit of BC1; top right picture is taken at the entrance of BC2 and the remaining two after the BC2 third and fourth dipole. Here q is the longitudinal coordinate in mm and p is the remaining energy offset in MeV after removing the correlated energy variation.

The calculation reported in Fig B.2 indicates that most of the energy modulation induced by space charge (the dominant collective effect) takes place between BC1 and BC2. By the time the beam reaches the second bunch compressor these fluctuations are sufficiently large to cause the instability to reach saturation, as indicated by the two bottom figures.

Projection of the 2D phase-space density can then be made to determine the linear charge density profile and energy distribution. Repeating the calculation by varying the rms energy spread for the initial density and then plotting the beam energy spread at the exit of the linac *vs.* the value at entrance yields a useful curve that gives guidance toward optimization of the tuning of the laser heater. Such curve was reported in Fig. 4.6 of Sec. 2, where a comparison is shown between the lattices with two and one bunch compressor. In these simulations the effect of the laser heater was represented as generating a beam energy density with Gaussian profile and adjustable rms spread. It should pointed out that this is only an approximation as the laser-beam interaction in the laser heater generates a more complicated energy density profiles – possibly yielding different Landau damping for equal rms energy spreads.

References

Abell D., 2006, Phys. Rev. ST Accel. Beams **9**, 052001.

Alexander J. *et al.* 2006, *4GLS Conceptual Design Report*, http://www.4gls.ac.uk/ documents.htm .

Arthur J. *et al.*, 2002, Linac *Coherent Light Source (LCLS) Conceptual Design Report*, SLAC Report No. SLAC-R-593.

Baboi N., 2001, Thesis, *Studies on Higher Order Modes in Accelerating Structures for Linear Colliders,* Hamburg.

Bane K. *et al.*, 1998a, *Calculation of the short-range longitudinal wake fields in the NLC Linac*, SLACPUB-7862.

Bane K., Mosnier A., Novokhatski A., and Yokoya K., 1998b, in *Proc. of the Inter. Comp. Acc. Phys. Conf.,* Monterey, USA, SLAC-R-580, p. 137.

Bane K., 2003, *Short-range dipole wake fields in accelerating structures for the NLC*, SLAC-PUB-9663.

Bane K. and Emma P., 2005, *LiTrack: A fast longitudinal phase space tracking code with graphical interface*, PAC2005, Knoxville, Tennessee, 4266.

Bane K., 2006, *Wake fields of sub-picosecond electron bunches*, SLAC-PUB-11829.

Bocchetta C.J. *et al*., 2007, *FERMI@elettra FEL: Conceptual Design Report*, http://www.elettra.trieste.it/FERMI/index.php?n=Main.CDRdocument.

Borland M., 2000, *"ELEGANT"- A flexible SDDS-compliant code for accelerator simulations*, APS Tech. Note LS-207.

Borland M., Chae Y., Emma P., Lewellen J., Bharadwaj V., Fawley W., Krejcik P., Limborg C., Milton S., Nuhn H.-D., Soliday R., and Woodley M., 2002, Nucl. Instrum. Methods Phys. Res. A **483**, 268.

Borland M., 2008, Phys. Rev. ST Acc. and Beams, **11**, 030701.

Brinkman R. *et al*., 2001, *TESLA Technical Design Report, Part II*, DESY-01-011, http://tesla.desy.de/new_pages/TDR_CD/PartII/accel.html

Chao A.W., Richter B., and Yao C.Y., 1980, Nucl. Instrum. Methods Phys. Res. **178**, 1.

Chao A.W., and Tigner M., 1999, *Handbook of Accelerator Physics and Engineering*, World Scientific, Singapore.

Corlett J.N. *et al.*, 2004, *A Recirculating Linac-based Facility for Ultrafast X-ray Science***,** Proc. of 2004 European Part. Acc. Conf., Luzerne.

Cornacchia M., Di Mitri S., Penco G., and Zholents A., 2006, Phys. Rev. ST Accel. Beams, **6,** 084402.

Craievich P., Di Mitri S., and Zholents A., 2006, Jitter Studies for the FERMI@elettra Linac, Proc. of 2006 European Part. Acc. Conf., Edinburgh,

Craievich P., Di Mitri S., and Zholents A., 2009, Nucl. Instrum. Methods Phys. Res. A **604**, 457.

Derbenev Ya.S., Rossbach J., Saldin E.L., and Shiltsev V.D., 1995, DESY-TESLA-FEL-95-05.

Derbenev Ya.S., Shiltsev V.D., 1996, FERMILAB-TM-1974 and SLAC-PUB-7181.

Di Mitri S. *et al.*, 2005, *Optimization and Modeling of the Accelerator for the FERMI@ elettra FEL*, Proc. of the FEL 2005 Conf., SLAC, USA.

Dohlus M., Limberg T., and Emma P., 2005, *Bunch compression for linac-based* FELs, Beam Dynamics Newsletter, N38, Ed. I.S. Ko.

Dowell D. H., Hayward T. D., and Vetter A. M., 1995, in Proc. of the 1995 Part. Acc. Conf. New York.

Emma P. and Brinkman R., 1998, Proc. 1997 Particle Accelerator Conference.

Emma P., Frisch J., and Krejcik P., 2000, *A Transverse rf Deflecting Structure for Bunch Length and Phase Diagnostics*, SLAC Report LCLS-TN-00-12.

Emma P. *et al.* 2009, *First Results of the LCLS Laser-Heater System,* PAC 2009, Proceedings.

England R. J. *et al.*, 2005, Phys. Rev. ST Accel. Beams **8**, 012801.

Efanov V, 2008, *private communication*. See also http://www.fidtechnology.com.

Heifets S., Stupakov G., and Krinsky S., 2002, Phys. Rev. ST Accel. Beams **5**, 064401.

Huang Z. and Kim K.-J., 2002, Phys. Rev. ST Accel. Beams **5**, 074401.

Huang Z., Borland M., Emma P., Wu J., Limborg C., Stupakov G., and Welch J., 2004, Phys. Rev. ST Accel. Beams **7**, 074401.

Kramer D. *et al.,* 2004, *The BESSY Soft X-ray Free Electron Laser*, Technical Design Report, BESSY, Berlin http://www.bessy.de.

Kur E. and Zholents A., 2008, *Investigation of Beam Instability Under the Effects of Long-range Transverse Wake Fields in the Berkeley Future Light Source*, LBNL-1061E.

Lee S.Y., Accelerator Physics, World Scientific, Singapore (1999).

Li D. and Corlett J.N., 2002, *Rf Deflecting Cavity Design for Berkeley Ultrafast x-Ray Source*, EPAC 2002, Proceedings.

Li R., Bohn C.L., and Bisognano J.J., 1997, Particle Accelerator Conference PAC97, 1644.

Lidia S., *private communication*, 2008.

Moncton D. and Graves W., 2003, *The MIT X-ray Laser Project*, Proc.of 2003 SRI Conference, p. 113, San Francisco, USA.

Murphy J.B., Krinsky S., and Gluckstern R.L., 1997, *PAC95*, 2980 (1995); *Part. Accel.* **57**, 9.

NERSC, National Energy Research Scientific Computing Center, http://www.nersc.gov.

Novokhatski A. and Mosnier A., 1996, DAPNIA/SEA-96-08.

Novokhatski A., Timm M., and Weiland T., 1998, TESLA Report. No. TESLA 99-16.

Penn G., *Jitter studies for Berkeley soft x-ray free electron laser*, to be published.

Portmann G.J. and Zholents A., 1996, *Ground Motion Measurements at the Advanced Light Source*, LBNL ALS Report LSAP-226.

Qiang J. *et al.,* 2000, J. Comp. Phys **163** 434.

Qiang J., Ryne R.D., Venturini M., Zholents A., and Pogorelov I., 2009, *High Resolution Simulation of Beam Dynamics in Electron Linacs for X-Ray Free Electron Lasers*, submitted to Phys Rev. ST Accel. Beams.

Ratner D. *et al.,2008, 3D Analysis of Longitudinal Space-Charge Microbunching Starting from Shot-Noise, Free* Electron Laser Conference FEL08 Conference, Proceedings.

Rosenzweig J. *et al.,* 1997, Nucl. Inst. and Methods A, **393**, 376-379.

Sacherer F., 1971, IEEE Trans. Nuc. Sci. NS-18 No. 3 1105.

Saldin E.L., Schneidmiller E.A., and Yurkov M.V., 1997, Nucl. Instrum. Methods Phys. Res. A **398**, 373.

Saldin E.L., Schneidmiller E.A., and Yurkov M.V., 2002, Nucl. Instrum. Methods Phys. Res. A **490**, 1.

Saldin E.L., Schneidmiller E.A., and Yurkov M.V., 2003, DESY Report No. TESLA FEL- 2003-02, 2003.

Saldin E.L., Schneidmiller E.A., and Yurkov M.V., 2005, Nucl. Instrum. Methods Phys Res.A **539,** 499.

Spampinati S., Di Mitri S., and Diviacco B., 2007, *A Laser Heater for FERMI@elettra*, Free Electron Laser Conference FEL07 Conference, Proceedings.

Stupakov G., 1995, *Geometrical Wake of a Smooth Taper*, SLAC-PUB-95-7086 TESLA TDR, 2001, DESY Report No. DESY-2001-011.

SUPERFISH, 1987 *Superfish Codes User Manual*: Report no. **LA-UR-87-126**, Los Alamos National Laboratory, Los Alamos.

Venturini M, Warnock R., Ruth R., and Ellison J., 2005, Phys. Rev. ST Accel. Beams **8** 014202.

Venturini M, Warnock R., and Zholents A., 2007a, Phys. Rev. ST Accel. Beam, **10** 054403.

Venturini M., 2007b, Phys. Rev. ST Accel. Beam **10** 104401.

Venturini M., 2008, Phys. Rev. ST Accel. Beam **11** 034401.

Venturini M., and Zholents A., 2008, Nucl. Instrum. Methods Phys. Res. A **593**, 53.

Xiang D. and Stupakov G., 2009, *Coherent soft x-ray generation in the water window with EEHG scheme*, SLAC-PUB-13645.

Yokoya K., Impedance of Slowly Tapered Structures, 1990, CERN Report, SL/90-88 (AP).

Zholents A., Heimann P., Zolotorev M., and Byrd J., 1999 Nuclear Instrum. Methods Phys. Res. A **425** , 385.

Zholents A. and Holdack K., 2006, *Energy Modulation of the Electrons by the Laser Field in the Wiggler Magnet: Analysis and Experiment*", Free Electron Laser Conference, FEL06, Berlin, Germany.